Ph.D. Dissertation of Engineering

Direct Estimation of the Specific Rate of Breakage using DEM and Development of a Grinding-Liberation Coupled Model

DEM을 이용한 직접적인 분쇄율 추정 및 분쇄와 단체분리 결합 모델 개발

February 2022

Graduate School of Engineering
Seoul National University
Energy Systems Engineering

Donwoo Lee

Direct Estimation of the Specific Rate of Breakage using DEM and Development of a Grinding-Liberation Coupled Model

Adviser: Heechan Cho

Submitting a Ph.D. Dissertation of Public Administration

October 2021

Graduate School of Engineering
Seoul National University
Energy Systems Engineering

Donwoo Lee

Confirming the Ph.D. Dissertation written by
Donwoo Lee
December 2021

Chair	민 동 주	(Seal)
Vice Chair	조 희 찬	(Seal)
Examiner	정 은 혜	(Seal)
Examiner	김 정 윤	(Seal)
Examiner	권 지 회	(Seal)

Abstract

Grinding is an energy-intensive process and the first step in mineral processing. However, it is difficult to accurately describe the grinding phenomenon owing to the complexities caused by the heterogeneity of natural mineral ore. This thesis introduces numerical and experimental approaches to effectively model the grinding process.

First, discrete element method (DEM) was used to demonstrate a ball mill grinding process and estimate the breakage characteristics of the sample by separating the machine- and material-dependent factors. Although the grinding kinetics model exhibited a high performance in terms of predicting the size distribution of the breakage products depending on breakage characteristics, there is a lack of understanding of the breakage phenomena occurring inside the mill. Therefore, by using DEM, all collisions occurring on each particle inside the mill can be effectively analyzed. However, when combined with the population balance equation for modeling the ball mill grinding process, the prediction accuracy of the particle size distribution of the breakage product becomes relatively low. In this thesis, the collision energy distribution for each particle was determined using DEM, and accurate energy data was obtained by realizing both ball media and rock particles in the ball mill simulation. In addition, a particle breakage probability model was introduced to independently apply the material dependent factors. Finally, the ability of the model to determine the breakage characteristics was improved by interpreting the simulation results of the grinding kinetics model. During the single-fraction

grinding test, the first-order kinetics was confirmed by changing the particle size distribution inside the mill over time. Additionally, the phenomenon wherein the particle breakage occurred more easily owing to repeated collisions was determined based on the energy distribution for each particle. Furthermore, the relationship between the breakage probability and breakage rate parameters was investigated to analyze the change in the breakage rate according to the scale-up of the mill and the change of the lifter.

Second, a model that could predict the particle size and grade distribution of the breakage product based on the grinding kinetics was developed. Owing to the development of liberation measurement equipment, various information can be obtained easily. However, there is lack of research on how to effectively utilize the information for modeling. In this study, the particle size and grade distribution of the breakage product were obtained by performing a ball mill grinding test or conducting a mineral liberation analyzer (MLA) measurement for various grade distributions and particle sizes. Furthermore, the breakage and liberation characteristics were identified depending on the grade and the MLA data. In particular, the liberation size, which is one of the liberation parameters, was determined by effectively utilizing the grain size distribution obtained from the MLA measurement. By using this model, it was possible to determine the target particle size and the required grinding time based on the degree of liberation.

This thesis presents a more practical method for modeling the ball mill grinding process based on numerical and experimental methods. In the case of numerical methods, it is expected that a deeper understanding of the breakage

characteristics of the particles could be achieved by analyzing the particle size distribution after breakage.

Nomenclature

Alphabetical Characters

A	Breakage rate of the reference size
a	Acceleration
$a_{i,j}$	Matrix used for the analytic solution of population balance equation of grinding
$B_{i,j}$	Cumulative breakage distribution: cumulative weight fraction of particles of size class i generated from a breakage of particle of size class j
BF	Breakage function
$b_{i,j}$	Breakage distribution for particle size: weight fraction of particles of size class i generated from a breakage of particle of size class j
$b_{ij,kl}$	Breakage distribution for particle size and grade: weight fraction of particles of grade class i and size class j generated from a breakage of particle of grade class k and size class l
b'	Breakage probability parameter that characterizes the mechanical strength
C_n	Damping coefficient for the normal component
C_s	Damping coefficient for the tangential component

c	Coefficient of scale-up empirical formula for the breakage rate according to formal powder filling
D	Mill diameter
D_n	Damage for the nth collision
D_{lib}	Liberation size
d	Ball diameter
d_p	Progeny particle size
d_p'	Parent particle size
E	Young's modulus
E_0	Threshold energy
$E_{0,n}$	Threshold energy for the nth collision
E_{50}	Mass-specific median fracture energy
E_b	Energy representing particle strength that normalizes the applied energy
$E_{b,n}$	Energy representing particle strength that normalizes the applied energy for the nth collision
E_b'	Energy representing particle strength that normalizes the applied energy for the weakened particle
E_d	Dissipation energy
$E_{f,0}$	Initial particle fracture energy
$E_{f,n}$	Mass-specific fracture energy after the nth collision
E_i	Weight fraction remaining in the top size class of the ith particle
E_k	Collision energy for the kth collision

E_s	Expected remaining weight fraction in the top size class
E_T	Young's modulus of the target
E_{total}	Sum of the effective energy
E'_{total}	Recalculated sum of the effective energy
E_∞	Fracture energy at coarse size
$\overline{(E - E_0)}_i$	Average effective energy for the ith particle
F_d	Damping force
F^c	Contact force
F_n^c	Contact force for the normal component
F_s^c	Contact force for the tangential component
F^{nc}	Non-contact force
f	Collision frequency
f_{Mat}	Particle resistance to fracture
g'	Parent particle grade
g_{ac}	Gravitational acceleration
g_l	Lower bound for Andrew-Mika diagram
g_u	Upper bound for Andrew-Mika diagram
I	Moment of inertia
J	Formal ball filling
l_i	Initial flaw length
K_l^*	Lower grade boundaries for the parent particle in size class l
K_l^{**}	Upper grade boundaries for the parent particle in size class l
k	Number of impacts
k_n	Spring coefficient for the normal component

k_s	Spring coefficient for the tangential component
M	Maximum t_{10} when the material is broken
M^r	Torque of rolling friction
m	Mass
N_t	Number of effective collisions for time t
n	Number of size class
$\hat{n}$	Unit vector for the normal component
P_B	Particle breakage probability
P_i	Cumulative weight fraction of the breakage products smaller than size class i
P_S	Particle survival probability
p	Parameter for beta distribution
p_E	Parameter for E_b
p_f	Parameter for f_{Mat}
q	Parameter for beta distribution
q_E	Parameter for E_b related to the particle size
q_f	Parameter for f_{Mat} related to the particle size
R	Particle radius
r	Parameter for beta distribution related to the parent particle grade and variance of progeny particles
S_i	Specific rate of breakage for size class i
S_{ij}	Specific rate of breakage for grade class i and size class j
S_V	Volume-specific surface area
$\hat{s}$	Unit vector for the tangential component

T	Contact duration
T_c	Contact time
t	Time
t_n	Weight fraction of particles whose size is less than $1/n$
U	Formal powder filling
v	Velocity
v_d	Velocity of the crack propagation
v_{el}	Velocity of the propagation of elastic waves
v_{fract}	Velocity of the crack propagation
$v_{rel,n}$	Relative velocity for the normal component
$v_{rel,s}$	Relative velocity for the tangential component
v_s	Equivalent velocities to strength
$W_{m,kin}$	Mass-specific kinetic energy
$W_{m,min}$	Mass-specific threshold energy for kinetic energy
W_v	Volume-specific elastic strain energy
$W_{v,i}$	Kinetic energy which can be stored in the vicinity of a characteristic crack of length l_i
w_i	Weight fraction of particle size class i
$w_{i,all}$	Weight fraction of grade class i considering all size classes
w_{ij}	Weight fraction of particle grade class i and size class j
x	Particle size
x_0	Reference size
$x_{0,f}$	Size where the fracture energy becomes twice the convergence value

x_i Particle size for size class i

z Number of chain links

Greek Characters

α	Slope of the exponential function for the breakage rate
α_{ac}	Angular acceleration
β	Cumulative breakage distribution parameter representing cleavage fracture property
β_{max}	Crack extension energy per unit of the created surface area
γ	Cumulative breakage distribution parameter representing breakage characteristics by shatter
γ_D	Damage coefficient
δ	Parameter reflecting the geometrical property of ore texture
δ_0	Material parameter for δ
δ_n	Overlap displacement for the normal component
δ_s	Overlap displacement for the tangential component
ε	Coefficient of restitution
η	Parameter affecting the rate of liberation before and after the liberation size
λ	Index indicating how rapidly the breakage rate decreases
μ	Particle size at which reduction ratio of the breakage rate is 0.5.
μ_f	Friction coefficient
μ_r	Rolling friction coefficient
ν	Poisson's ratio
ν_T	Poisson's ratio of the target

ρ	Density
σ	Standard deviation
σ_k	Applied stress
σ_s	Strength of the link
$\Sigma\tau$	Net torque
Φ	Cumulative breakage distribution parameter representing intercept with when the relative size is $1/\sqrt{2}$
φ_c	Critical mill rotational speed
φ_r	Fraction of the rotational speed to the critical mill rotational speed
χ	Slope of the size-fracture energy plot
$\chi(g)$	Normalized grade for the upper and lower grade bounds
ω	Angular velocity
ω_{rel}	Rolling friction coefficient

Table of Contents

List of Figures

List of Tables

Chapter 1. Introduction

1.1. Research Background

An estimated 2% of the total energy in the world is used for mineral comminution (Napier-Mun, 2015). Grinding, the first stage in mineral processing, is a highly energy-intensive process. During grinding, about 10%–20% of the input energy is used for actual size reduction (Napier-Mun, 2015), whereas the remaining is dissipated and lost. One of the purposes of grinding is to liberate valuable minerals from gangue minerals. Generally, a higher degree of liberation can be achieved by decreasing the particle size. However, the energy required for grinding increases significantly as the particle size decreases. Furthermore, when the particles generated during the breakage process is added to the subsequent process, excessively small particles are not preferred owing to the characteristics of the subsequent process. Therefore, it is necessary to develop a suitable model to predict the characteristics of the product after grinding to increase energy efficiency and produce a breakage product with an appropriate particle size.

The process of grinding can be modeled mathematically using two approaches: grinding kinetics model and energy-based model. Grinding kinetics model is based on chemical reaction kinetics, wherein intermediates are produced from the reactants in a consecutive chemical reaction, and simultaneously disappear when converted into products. Similarly, in grinding, particles of a specific size are produced owing to the breakage of larger particles, and concurrently disappear due to breakage. Therefore, the rate equation based on the population balance can be

established for all particle sizes (Gardner and Austin, 1962), similar to the rate law for chemical reactions.

The energy-based model uses an energy-size reduction relationship to characterize the grinding property. As the size decreases due to the applied energy, the energy-size reduction relationship is claimed to be more rational, and hence, can decouple the machine- and material-dependent effects. Considering this, the size-energy relationship can be derived by conducting single-particle breakage tests using the twin pendulum or the drop weight (Narayanan and Whiten, 1983). In this test, particles are broken under the impact at various energy levels. Considering the size distributions of the breakage products based on the relative size remains similar in shape for a wide range of energy inputs, particle sizes, and ore types, it can be described by a single point on the distribution.

The aim of both models is to predict the particle size distribution of the breakage products. Both models are extensively used in mineral processing and can effectively determine the breakage properties of a material. Considering the grinding kinetic model determines the parameters based on the breakage product, it can predict results more accurately using the equipment provided. However, because grinding is a complex mechanism, continuous research is being conducted to understand its principles. This study aims to improve the grinding model and ensure it is more practical and comprehensive.

1.2. Recent Studies

1.2.1. Overview of the Size-Grade Grinding Kinetics Model

The kinetics model of the grinding process was developed similar to the chemical reaction kinetics. In grinding mills, particles of a specific size are produced owing to the breakage of larger particles, and transformed into smaller particles during the breakage process. Therefore, the rate equations for particles of all sizes can be established, which comprises two breakage functions: the specific rate of breakage, which is the rate constant for the disappearance of particles due to breakage, and the primary breakage distribution, which is the weight distribution function of the fragments produced from breakage. Several studies have demonstrated that this model can accurately simulate the ball mill grinding process while treating various ores. Furthermore, researchers have studied a model that can predict size reduction and liberation simultaneously.

The first attempt to model mineral liberation based on ore texture was made by Gaudin (1939). By using an ideal binary mineral system model comprising cubic grains of equal sizes. Using this cubic grain lattice, a cubic fracture lattice was applied to investigate the mineral liberation owing to breakage. According to Gaudin's model, the degree of liberation is related to the ratio of the grain and particle sizes and the relative abundance of the two minerals.

Although several mineral liberation models have been proposed after the Gaudin's model, owing to the complexity of the subject, no standard model has been generally accepted. One method of modeling mineral liberation is by describing the texture of the ore and analyzing how liberation occurs when random breakage is

applied (Gaudin, 1939; Wiegel and Li, 1967; Ferrara et al., 1989; Evans et al., 2013). The Julius Kruttschnitt Gaudin Random Liberation Model (JK-GRLM), studied by Evans (2013), determines the size and grade of breakage products by random breakage for a given ore texture. First, the grain size distribution is measured using X-ray tomography, and is randomly arranged in a cubic virtual block. Then, random breakage in a cubic lattice is applied to generate breakage products, and the liberation characteristics are identified by recording the properties of each particle. Recently, Mariano (2016) conducted a study on cases where non-random breakage occurred. However, investigating real ore to describe its texture to an actual one is time consuming. Moreover, additional experiments should be performed to analyze non-random breakage.

Another way to quantitatively describe liberation is by calculating it using a mathematical model. Andrews and Mika (1976) used a heterogeneous material comprising two distinct mineral species. Peterson and Herbst (1985) classified particles into three categories according to their mineral composition; free particles of mineral A, free particles of mineral B, and mixed particles containing minerals A and B. A balance equation was established for the weight change rate by applying different breakage rate and breakage distribution functions for each group, based on the assumption that the fraction of particles of mixed material that breaks into smaller free particles is proportional to the fraction of free particles breaking into the same smaller-sized free particles. Furthermore, considering the breakage product of free particles is the same free particles, the three balance equation can be solved easily.

Furthermore, King and Schneider (1998) proposed a general solution for batch grinding that considers all grade classes. Herein, the breakage rate and

breakage distribution varied depending on the particle size and grade. Schneider (1995) determined the quadrivariate breakage function using the Andrew-Mika diagram and beta distribution.

1.2.2. Overview of the Energy-based Model

The simplest approach for modeling grinding to predict the particle size of the breakage products is to relate the fineness of the breakage products to the specific energy of grinding. Classical approaches based on Rittinger's, Kick's, and Bond's laws were in turn based on the empirical energy–size relationships. Although these models often explain the grinding results for various mill and particle sizes, their application is limited to the only estimating the effect of changing the feed or product on the specific energy during grinding. Moreover, this model does not provide information on the particle size distribution of the breakage products.

In recent years, energy-size reduction relationships have gained wide attention. Studies have debated that the size-balance model is based on a black-box approach, which in turn is based on the outcome of milling, regardless of the milling geometry and operational conditions (Shi and Xie, 2015). Therefore, the energy-size reduction relationship is considered to be more rational than the size-balance approach and decoupling of the machine- and material-dependent effects. The energy used in the model is a specific energy applied to the particle per mass. Accordingly, the size-energy relationship can be derived by conducting a single-particle breakage test using either the twin pendulum or drop weight approaches (Narayanan and Whiten, 1983).

The tests were conducted by applying an adequate amount of energy to a relatively large particle to induce breakage on a single impact. Particles break under the impact at various energy levels. It has been observed that the size distribution of the breakage products based on a relative size is similar in shape for a wide range of energy inputs, particle sizes, and ore types, and hence, can be described by a single point on the distribution.

However, on analyzing the energy-size reduction relationship for various particle sizes, it was found that the model was inadequate for describing the fracture phenomenon of relatively fine particles, wherein breakage mainly occurs due to repetitive impacts. Alternatively, a new tester was designed to experiment with smaller particles whereas particle-particle collisions were almost completely blocked (Schönert and Marktscheffel, 1986). Accordingly, a model with new added elements was proposed, such as breakage due to repeated damage, particle size effects, and the particle strength (Vogel and Peukert, 2003).

The Vogel and Peukert model calculates the probability of a particle's breakage depending on the applied energy. In this model, the breakage probability is a function of two parameters, the threshold energy required by the minimum energy to break a particle, and the standardization energy that causes different breakage probability by the particle strength even if the same energy is applied. Shi and Kojovic (2007) proposed the energy-size reduction relationship wherein the breakage probability model is modified and comprises the same two parameters. The relationship reflects the effect of particle size, and the overall product size distribution can be calculated from the single point in the size distribution.

Recently, Shi and Xie (2015) used the procedure to simulate the batch grinding process in a ball mill. The mean specific energy was calculated by multiplying the mill power draw and the grinding time. Although this machine-dependent factor is distinct from the material-dependent factor obtained from particle breakage tests, it was assumed that the mean specific energy was not applied evenly to all particles in the ball mill, and was proportional to particles of different sizes at arbitrary ratios obtained by fitting the data to the model predictions. The breakage product size distribution was predicted by combining size-specific energy, breakage parameters, and feed size distribution, and was found to be in good agreement with the experimental results. As such, the energy-based model successfully predicted the particle size of the breakage product in several studies (Vogel and Peukert, 2005; Shi and Kojovid, 2007; Meier et al., 2009; Bonfils et al., 2016; Shi, 2016); however, the machine-dependent factors were not to be independently identified.

1.2.3. Overview of the DEM-PBE Combined Approach

In the late 1980s, a combined model of energy and PBE was studied to replace the two breakage functions (breakage rate and primary breakage distribution) of the traditional population balance equation with a function of energy. The fragment distribution according to energy was determined from the breakage tests of the particle bed, whereas the weight average was set as the breakage distribution function based on the collision energy distribution applied to particles (Cho, 1987). However, the collision energy distribution in the experiment was determined using back-calculation to fit the experimental data.

7

DEM, developed by Cundall and Stack (1979), is a numerical method that tracks discrete particles interacting with each other. In conventional soft-contact DEM, particles overlap when they collide with each other, which exhibits both elastic and nonelastic properties. The force generated by the overlap can be decoupled into normal and tangential components depending on the contact model. After determining the forces acting on the particles, the displacements of the particles are calculated. Generally, the linear spring-dashpot model is used for the normal components, whereas a slider is added in the tangential components.

Considering DEM can calculate the energy applied to all particles, it was used to predict the energy-particle breakage relationship by coupling with DEM in breakage modeling. However, a large number of DEM particles are required to simulate a ball mill grinding process, which is limited by the computation performance and computer memory (Cleary and Morrison, 2011). Although advances in computer technology have made it possible to process more particles, it is still impossible to simulate ball mills used on an industrial scale. The simplest way to solve this problem is to perform DEM simulation for ball mill modeling using only ball media and excluding rock particles (Powell et al., 2008), while assuming that rock particles always exist between balls when they collide. However, information on the number of squeezed rock particles and energy applied to each particle is required.

Datta and Rajamani (2002) proposed a method of modeling batch grinding by combining population balance and DEM. Using this model, a population balance equation was established using the collision frequency according to various energy classes occurring in the ball mill. Furthermore, t calculates the rate of change of the

weight fraction with time by introducing the breakage rate and breakage distribution functions depending on the collision energy. Although the two breakage functions are determined by a drop weight test of 4-layers particle bed, the particle layer between the two colliding balls in the actual ball mill does not always comprise 4 layers. Therefore, the estimated results of the model do not match with the experimental results. Therefore, a correction factor is used to match the experimental data.

Recently, the Universidade Federal do Rio de Janeiro by Tavares (2017) proposed a new model that considers the particle weakening effect caused by repeated collisions and the surface breakage caused by tangential force. Furthermore, this model is based on DEM simulation involving only ball media, and geometrically determines the number of particles between two colliding balls when spherical particles are arranged according to dense hexagonal packing. It is assumed that the energy applied to each particle is evenly distributed. Although this model was developed in consideration of various factors from a microscale perspective, it did not completely agree with the experimental data owing to its complexity.

1.3. Research Objectives and Scope

As mentioned in Sections 1.1 and 1.2, this thesis analyzes the modeling of the ball mill grinding process through numerical and experimental methods. Numerical methods are used to analyze the mechanical phenomena that occurs inside the mill, an area lacking from the grinding kinetics model. Most ball mill grinding process modeling are performed based on the assumption that there are only balls, and no

rock particles. However, in this case, much more information is needed to determine the energy acting on the rock particles. Furthermore, it is difficult to simplify and determine the energy applied to the particles inside the mill owing to its complexity. In addition, to assume that there is always a particle between the two balls, the ball loading amount is forced to be 1 or more. Therefore, this study was carried out by implementing both ball media and rock particles to simulate a laboratory-scale ball mill and realistically determine the energy distribution received by individual particles. Furthermore, the prediction performance of the DEM coupling model was improved by introducing a crushing kinetics model to interpret the results. To this end, it was verified whether the primary grinding kinetics was established according to the various particle size distributions in the mill, and whether it was possible to reasonably calculate the grinding rate when the equipment elements and material elements were individually given. Additionally, the operating conditions of the ball mill are diversified including the size of the lifter.

In the experimental method, a grinding kinetics model with high predictive performance was proposed, and it is related to the particle size reduction as well as liberation. However, there is no representative model among the particle size-liberation coupled models. Additionally, owing to the development of equipment for measuring the degree of liberation, the grade distribution can be measured easily; however, not many studies have used it effectively to predict the particle size and grade distribution of the breakage products. Therefore, in this study, ball mill grinding tests were performed on various grades of samples to understand the breakage characteristics. Furthermore, the liberation characteristics were determined by measuring and analyzing the grade distribution of the samples with various

particle sizes and grades using MLA. Herein, the liberation parameters were effectively selected by using the measured grain size distribution to determine the target particle size using the model.

Chapter 2. Background Theory

2.1. Grinding Models

2.1.1. Grinding Kinetics Model

The grinding kinetic model was developed using a population balance approach that was analogous to the chemical reactor design for first-order reactions. This approach is based on the results of the experimental batch grinding. The model comprises two breakage function: specific rate of breakage and primary breakage distribution.

2.1.1.1. Specific rate of breakage

Consider a simple batch grinding test wherein the size interval is a geometric sequence ($\sqrt{2}$) and the starting feed is within the top size interval. If the rate of disappearance of the top size is proportional to the weight fraction of the top size, the rate of change of weight fraction can be expressed as:

$$\frac{dw_1(t)}{dt} = -S_1 w_1(t), \qquad (2.1)$$

where $w_1(t)$ is the weight fraction of size class 1 at time t and S_1 is a proportionality constant, called the specific rate of breakage. If the specific rate of breakage is independent of time, Eq. (2.1) can be modified as:

$$\log[w_1(t)] = \log[w_1(0)] - \frac{S_1 t}{2.3}, \qquad (2.2)$$

Therefore, the specific rate of breakage can be determined by plotting the fraction of unbroken material against the corresponding grinding time. Then, the slope of the log-linear plot of $\frac{w_1(t)}{w_1(0)}$ and time becomes the breakage rate. Figure 2.1 shows a typical experimental result of the batch grinding test.

The specific rate of breakage is a function of the particle size. By conducting the procedure repeatedly with different starting feed sizes, a set of the breakage rate values can be obtained (Figure 2.2). It was observed that smaller particles were more resistant to breakage, and hence, the breakage rate generally decreases with decreasing size. However, the breakage rate decreases for larger particle sizes when the particle is too big to be nipped properly or too strong to be fractured for the given ball size. Mathematically, a typical relationship between the size and specific rate of breakage is given as:

$$S_i = A \left(\frac{x_i}{x_0}\right)^\alpha \left[\frac{1}{1+\left(\frac{x_i}{\mu}\right)^\lambda}\right], \tag{2.3}$$

where x_0 is a reference size, typically set to 1 mm, A is the specific rate of breakage of the reference size, and α is the slope of the exponential function. μ is a particle size at which the reduction rate is 0.5 and λ is an index indicating how rapidly the specific rate of breakage decreases as the particle size increases.
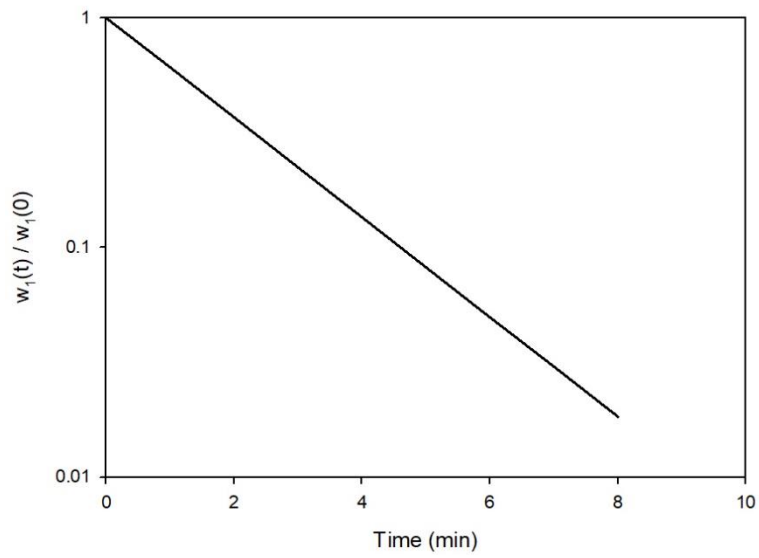
Figure 2.1. Example of the first-order plot.
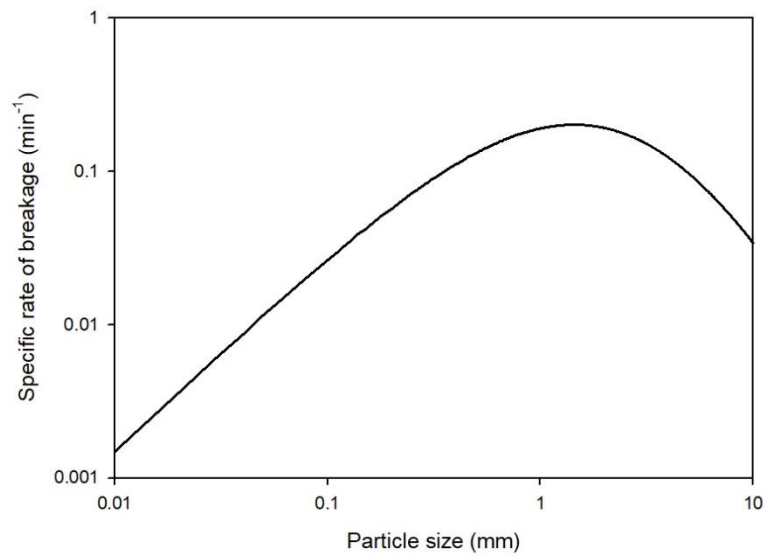
Figure 2.2. Example of the relationship between the particle size and specific rate

of breakage.

2.1.1.2. Primary breakage distribution

Grinding samples in a single size fraction generates products for a whole size fraction, which is smaller than the feed size. To describe the grinding process, it is important to determine the primary breakage distribution, which is the size distribution of fragments measured before the fragments are reselected for further breakage. Primary breakage distribution is denoted as $b_{i,j}$, indicating the weight fraction of fragments in size class i generated by the breakage of particle in size class j. If n is the number of the size classes, i ranges from $j + 1$ to n. In addition, $B_{i,j}$ is a cumulative form of $b_{i,j}$, which indicates the weight fraction of fragments smaller than size class i generated by the breakage of particle in size class j. It was observed that $B_{i,j}$ is independent of the milling condition and is dimensionally normalizable.

$B_{i,j}$ can be determined by conducting the single-size-fraction test with a short grinding time, where 20–30% of the feed is out of the top size fraction. However, considering it is difficult to guarantee that only primary breakage occurs during that grinding time, approximate corrections should be made (Kelly and Spottiswood, 1990). Generally, the BII method proposed by Austin and Luckie (1972), based on the compensational condition where the product of S_j and $B_{i,j}$ is only a function of size class $i,$ is used to correct secondary breakage and calculate the $B_{i,j}$ values. Physically, this means that the weight fraction of the products smaller than size class i generated from the breakage of particles in size class j only depends on the size class i. Under this condition, the weight fraction of the breakage products smaller than size class i at time t, $P_i(t)$ can be calculated as:

$$1 - P_i(t) = [1 - P_i(0)] \exp(-S_j B_{i,j} t), \qquad (2.4)$$

For the top size, Eq. (2.4) can be rewritten as:

$$1 - P_i(t) = [1 - P_i(0)] \exp(-S_1 B_{i,1} t), \qquad (2.5)$$

When the size class i is 2, Eq. (2.5) can be modified as:

$$1 - P_2(t) = [1 - P_2(0)] \exp(-S_1 t), \qquad (2.6)$$

Substituting Eq. (2.6) in Eq. (2.5) provides:

$$B_{i,1} = \frac{\log[(1-P_i(0))/(1-P_i(t))]}{\log[(1-P_2(0))/(1-P_2(t))]}, \qquad (2.7)$$

Therefore, $B_{i,1}$ can be determined by weighing the products of single-size fraction test.

The $B_{i,1}$ values according to the relative particle size can be defined as the sum of the two power function like Eq. (2.8). Figure 2.3 shows an example of the primary breakage distribution on the log-log scale graph.

$$B_{i,1} = \Phi \left(\frac{x_{i-1}}{x_1} \right)^{\gamma} + (1 - \Phi) \left(\frac{x_{i-1}}{x_1} \right)^{\beta}, \qquad (2.8)$$

where Φ is the intercept shown in Figure 2.3, γ is the breakage characteristics by shatter, which occurs with high energy intensities, and β is the cleavage fracture property, which occurs with low energy intensities.
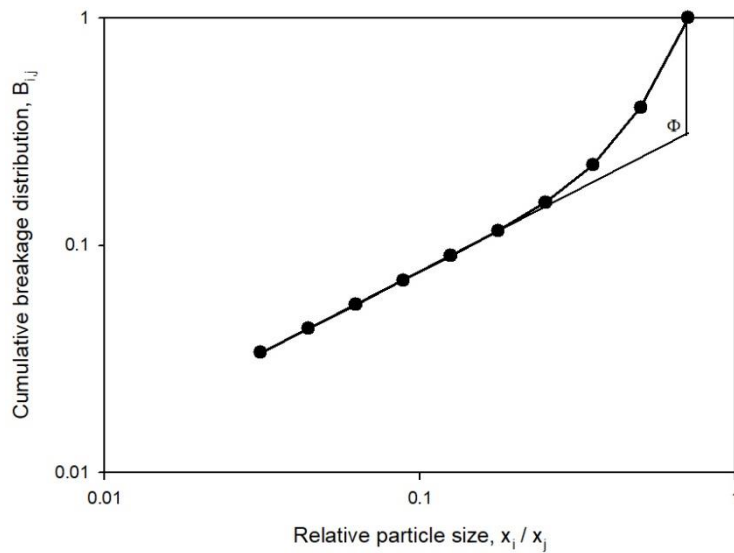
Figure 2.3. Example of the cumulative breakage distribution plot.

2.1.1.3. Population balance equation

The equation for population balance can be established based on breakage functions S and b, as shown in Eq. (2.9). The concept applied to the population balance equation is a rate-mass balance equation on each size interval.

$$\frac{dw_i(t)}{dt} = -S_i w_i(t) + \sum_{j=1,i>1}^{i-1} b_{i,j} S_j w_j(t), \tag{2.9}$$

The total rate of mass change in size class i is the sum of the disappearance rate of size i material caused by breakage and the appearance rate of size i material caused by breakage of larger size class j. If the specific rate of breakage is independent of the grinding time, several analytical solutions can be obtained to calculate the weight fraction of breakage products at a given grinding time. One form of the solution, called Reid solution, is given as:

$$w_i(t) = \sum_{j=1}^{i} a_{ij} \exp(-S_j t), \tag{2.10}$$

where the values of a_{ij} are as defined,

$$a_{ii} = w_i(0) - \sum_{k=1,i>1}^{i-1} a_{ik}, i = j \ ,$$

$$a_{ij} = \frac{1}{S_i - S_j} \sum_{k=j}^{i-1} S_k b_{ik} a_{kj}, i > j \ , \tag{2.11}$$

Herein, a sequential calculation from the top size to the next size is required.

2.1.1.4. Coupled grinding and liberation model

Andrews and Mika (1975) modified the population balance equation to binary ores, expressed as:

$$\frac{dw_{ij}(t)}{dt} = -S_{ij}w_{ij}(t) + \sum_{l=1}^{j-1}\sum_{k=K_l^*}^{K_l^{**}} S_{kl}b_{ij,kl}w_{kl}(t), \qquad (2.12)$$

where $w_{ij}(t)$ is the weight fraction of the particles with grade class i and size class j, S_{ij} is the specific breakage rate of the particles with grade class i and size class j, and $b_{ij,kl}$ is the weight fraction of the progeny particles in grade class i and size class j resulting from the breakage of parent particles in grade class k and size class l. K_l^* and K_l^{**} are the lower and upper grade boundaries for parent particles in size class l, respectively, to generate the progeny particles in grade class i and size class j. The grade boundaries can be determined using the Andrews-Mika diagram, which explains the two regions: feeder region and attainable region, as shown in Figure 2.4. The feeder region contains all particles that can generate the parent particle whereas the attainable region represents the grade boundaries of the progeny particle for each particle size.
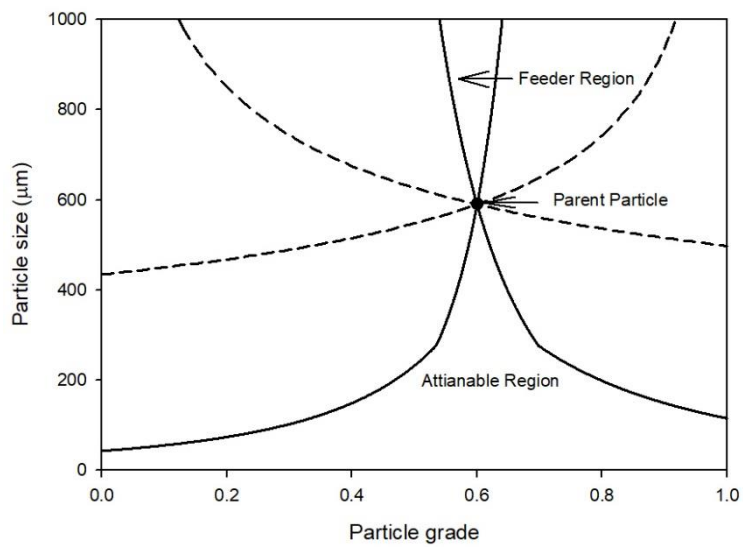
Figure 2.4. Example of the Andrews-Mika diagram.

The dashed and solid lines in Figure 2.4 denote the allowable grade range when the total amount of minerals must be conserved and the confined grade range depending on the ore texture or the mineral grain size, respectively. King (2001) proposed the empirical model for grade boundaries:

$$g_u = max\left[g'\left(\frac{d_{p'}}{d_p}\right)^{0.2}, g'\left(\frac{D_{lib}}{d_p}\right)^{\delta}\right],$$ (2.13)

$$1 - g_l = max\left[(1 - g')\left(\frac{d_{p'}}{d_p}\right)^{0.2}, (1 - g')\left(\frac{D_{lib}}{d_p}\right)^{\delta}\right],$$ (2.14)

$$\delta = min\left[\delta_0\left(\frac{D_{lib}}{d_{p'}}\right)^{0.5}, 3\right],$$ (2.15)

where g_u and g_l are the upper and lower bounds of the progeny particle grade, respectively. g', d_p', and d_p are the parent particle grade, size, and progeny particle size, respectively. The liberation size, D_{lib}, is the particle size at which the mineral starts to liberate so it is closely related to mineral grain size. δ reflects the geometrical property of the ore texture that affects how quickly the grade range expands, and δ_0 is a material parameter. As seen in Eq. (2.15), the value 3 was a result of the constraint that the total amount of minerals should be conserved.

After determining the grade bounds of the progeny particle using the Andrews-Mika diagram, the grade distribution within the upper and lower bounds was described by the beta distribution, a continuous probability distribution defined on the interval [0, 1] and calculated by two positive shape parameters p and q, given as:

21

$$f(g; p, q) = \frac{g^{p-1}(1-g)^{q-1}}{\int_0^1 x^{p-1}(1-x)^{q-1}dx},$$ (2.16)

where p and q are calculated by using the parent particle grade and variance of the grade distribution of the progeny particles, respectively. According to the grade and variance, various types of grade distribution can be described, as shown in Figure 2.5.
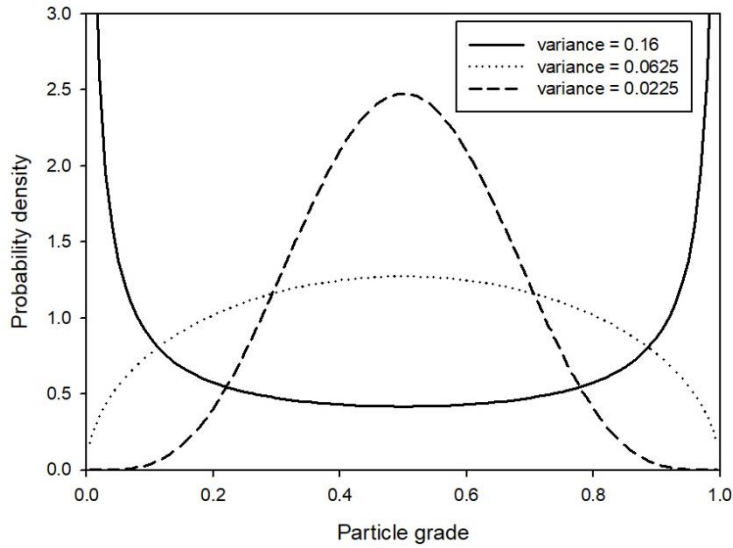
Figure 2.5. Various shapes of beta distribution according to the variance

There are two cases of grade boundary conditions that can be determined from the Andrew-Mika diagram; however, the method of calculating p and q in Eq. (2.16) are different for each case. First, the grade boundary is in [0, 1], and second, one or both of the upper and lower boundaries are out of the range [0, 1]. As mentioned above, beta distribution is defined on interval [0, 1], and hence, the upper and lower grade bounds should be 1 and 0, respectively, in order to use beta distribution. In the first case, the transformed grade is used to normalize the grade between 0 and 1, given as:

$$\chi(g) = \frac{g - g_l}{g_u - g_l}, \qquad (2.17)$$

Subsequently, p and q are calculated using Eqs. (2.18) to (2.22). r is related to the grade of the parent particle and the variance of the progeny particles, as shown in Eq. (2.20). The variance is calculated using Eq. (2.21), the products of the maximum value of the variance and the effect of the progeny particle size represented by $f(d_p)$. η indicates how quickly liberation occurs as the particle size decreases. As η increases, the liberation hardly occurs when the progeny particle is much larger than liberation size. However, if the size of the progeny particle decreases and becomes smaller than the liberation size, liberation occurs rapidly.

$$p = \chi(g')r, \qquad (2.18)$$

$$q = \{1 - \chi(g')\}r, \qquad (2.19)$$

$$r = \frac{g' - (g')^2 - \sigma^2}{\sigma^2} = \frac{1 - f(d_p)}{f(d_p)}, \tag{2.20}$$

$$\sigma^2 = g'(1 - g')f(d_p), \tag{2.21}$$

$$f(d_p) = \frac{1}{1 + \left(\frac{d_p}{D_{lib}}\right)^\eta}, \tag{2.22}$$

Using the calculated values of p and q, the grade distribution in the given grade boundaries can be determined as:

$$P(g) = \begin{cases} 0 & g < g_l \\ \frac{\int_0^g x^{p-1}(1-x)^{q-1}dx}{\int_0^1 x^{p-1}(1-x)^{q-1}dx} & g_l < g < g_u, \\ 1 & g < g_u \end{cases} \tag{2.23}$$

where $P(g)$ is a weight fraction of the particles whose grade is smaller than g.

In the other case, because beta distribution is defined on the interval [0, 1], it cannot reflect the completely liberated particles. Therefore, after plotting the beta distribution using the transformed grade in Eq. (2.14), the completely liberated particles was calculated as:

$$L_0 = \frac{\int_0^{\chi(0)} x^{p-1}(1-x)^{q-1}dx}{\int_0^1 x^{p-1}(1-x)^{q-1}dx}, \tag{2.24}$$

$$L_1 = 1 - \frac{\int_0^{\chi(1)} x^{p-1}(1-x)^{q-1}dx}{\int_0^1 x^{p-1}(1-x)^{q-1}dx}, \tag{2.25}$$

where L_0 and L_1 are the completely liberated gangue and valuable mineral, respectively. However, because the grades lower than 0 and upper than 1 are treated as 0 or 1 in Eqs. (2.24) and (2.25), the mean grade can be changed. In this study, was assumed that the average grade of each progeny particle size class was the same as grade of the parent particle based on random breakage. Therefore, the bisection method was used to determine the proper grade to keep the mean grade constant. The value existed between the parent particle grade g' and $\chi(g')$. After calculating the values for p, q, L_0, and L_1 using the grade values, the grade distribution in the given grade boundaries was determined as:

$$P(g) = L_0 + (1 - L_0 - L_1) \; \frac{\int_0^g x^{p-1}(1-x)^{q-1}dx}{\int_0^1 x^{p-1}(1-x)^{q-1}dx}, \qquad (2.26)$$

2.1.2. Energy–Breakage Probability Model

Vogel and Peukert (2002; 2003; 2004) conducted studies on particle breakage probability models and published several papers. The model considered two different procedures, a generalized dimensional analysis approach (Rumpf, 1973) and a detailed fracture mechanical model (Weichert, 1992).

2.1.2.1. Dimensional analysis

Through dimensional analysis, Rumpf (1973) derived Eq. (2.27) to characterize the breakage similarity for similar particles of different materials.

$$S_V x = f\left(\frac{W_V}{E}, \frac{W_V x}{\beta_{max}}, \frac{v_{fract}}{v_{el}}, \frac{v_d}{v_{el}}, \frac{l_i}{x}, \nu\right), \qquad (2.27)$$

$$v_{el} = \sqrt{\frac{E}{\rho}}, \tag{2.28}$$

where S_V, W_V, β_{max}, l_i, and v are the volume-specific surface area, volume-specific elastic strain energy, crack extension energy per unit of created surface area, initial flow size, and Poisson's ratio, respectively. v_{fract}, v_{el}, and v_d are the velocities of the crack propagation, propagation of elastic waves, and the deformation, respectively. Vogel and Peukert (2003) argued that $\frac{v_{fract}}{v_{el}}$ and $\frac{v_d}{v_{el}}$ can be considered as quasistatic problems, and hence, can be neglected based on the experimental data from Williams (1984).

In addition, Vogel and Peukert (2003) introduced two functions to describe the breakage behavior of particles: breakage probability P_B, which is the proportion of particles broken in the experiment, and breakage function BF, which is the size distribution of the fragments of the broken particles except for the unbroken particles. Substituting the two functions in Eq. (2.29) provides get:

$$P_B, BF = f\left(\frac{W_V}{E}, \frac{W_V x}{\beta_{max}}, \frac{l_i}{x}, v\right), \tag{2.29}$$

The difference in the breakage behavior of the particle is determined by the Young's modulus and Poisson's ratio of the particle, and the toughness of materials β_{max} and l_i.

2.1.2.2. Fracture mechanical model

Weichert (1992) described the probability of particle breakage based on Weibull statistics (Weibull, 1951) to develop the fracture mechanical model. This model is based on the weakest link theory, which states that the survival probability of a chain is a product of the survival probabilities of links within the chain (Eq. (2.30)).

$$P_B = 1 - \exp\left\{-z\left(\frac{\sigma_k}{\sigma_s}\right)^m\right\},$$

(2.30)

where z, σ_k, σ_s, and m are the number of links, applied stress or load, strength of links, and Weibull parameter, respectively. Vogel and Peukert (2003) assumed that the propagation of the crack and particle breakage begin at the circumference of the contact circle considering the highest tensile stress occurs there. Furthermore, considering the statistical distribution of flaws and micro-cracks, the diameter of the contact circle was assumed to be equal to the number of chain links in the Weibull statistics. By substituting the pressure distribution in the collision and the diameter of the contact circle calculated using Hertzian theory (Hertz, 1882), the authors derived the following equation that describes the probability of breakage owing to the impact load.

$$P_B = 1 - \exp\left\{-const.\, x\left[1 + \frac{E}{E_T}\frac{1-v_T^2}{1-v^2}\right]^{\frac{1}{5}}\left[\frac{1-v^2}{E}\rho v^2\right]^{\frac{1}{5}}\left[\frac{v^2}{v_s^2}\right]^{\frac{m}{5}}\right\},$$

(2.31)

where v and v_s are the equivalent velocities to the stress and strength in Eq. (2.30), respectively.

2.1.2.3. Breakage probability equation

As seen in Eq. (2.29), because the initial flaw size is much smaller than the particle size, $\frac{l_i}{x}$ can be neglected. Additionally, Vogel and Peukert (2003) introduced two new parameters, f_{Mat} and $W_{V,i}$, which are related to β_{max}, E and ν considering they are difficult to apply practically owing to the diversity of particles. f_{Mat} denotes the particle resistance to fracture in collision, and $W_{V,i}$ is a volume-specific threshold energy for activating a crack. Setting the Weibull parameter to 4 based on the experiment and inserting these two parameters into in Eq. (2.31) provides:

$$P_B = 1 - \exp\{-f_{Mat}x(W_{m,kin} - W_{m,min})\}, \qquad (2.32)$$

where $W_{m,kin}$ and $W_{m,min}$ are the mass-specific kinetic impact energy and mass-specific threshold energy for particle breakage, respectively. The product $xW_{m,min}$ must be constant considering both $W_{V,i}$ and l_i are size independent. When k successive collisions are applied with an identical energy of $W_{m,kin}$, using Weibull's weakest chain link theory. Eq. (2.32) can be re-written as:

$$P_B = 1 - \exp\{-f_{Mat}xk(W_{m,kin} - W_{m,min})\}, \qquad (2.33)$$

2.1.2.4. Modification of the Vogel and Peukert model

The Vogel and Peukert model is useful for determining the breakage of a particle. However, the equation can only be applied in limited situations with identical amounts of energy. Furthermore, no information is available on the progeny particle size distribution, which is important for analyzing the grinding phenomenon to

predict the breakage products. Morrison et al. (2007) modified Eq. (2.33) to simulate a series of collisions of different specific energies, given as:

$$P_B = 1 - \exp\{-b' \textstyle\sum_k (E_k - E_0)\}, \tag{2.34}$$

where b' is a model parameter that characterizes the mechanical strength, E_k is the mass-specific energy in the kth collision event, and E_0 is the mass-specific threshold energy. If E_k is less than E_0, the contribution to breakage from the kth collision is zero.

Shi and Kojovic (2007) introduced a single parameter t_{10} to Eq. (2.33) to describe the progeny particle distribution (Eq. (2.35)).

$$t_{10} = M[1 - \exp\{-f_{Mat} x k (W_{m,kin} - W_{m,min})\}], \tag{2.35}$$

where M is the maximum t_{10} when the material is broken. t_n is the weight fraction of particles whose size is less than $1/n$ of the original size. Because t_{10} is related to t_n, which indicates the other points comprising the particle size distribution, t_{10} can determine the overall particle size distribution (Narayanan and Whiten, 1988). Figure 2.6 shows the t_n-family curves for various ore types (Narayanan and Whiten, 1988); n is generally 2, 4, 25, 50, and 70, as shown in the plot. When t_{10} is determined using Eq. (2.35), a straight line perpendicular to the x-axis can be drawn, which indicates the particle size distribution of the corresponding t_{10}.
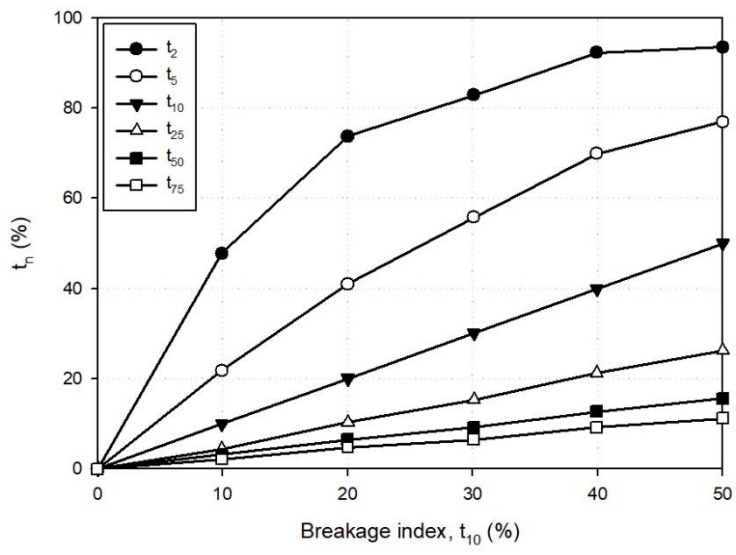
Figure 2.6. t_n-family curves.

2.2. Discrete Element Method

Discrete element method is a numerical method that tracks discrete particles which interact with each other. It was developed by Cundall and Strack (1979) to describe the motion of granular assemblies. To analyze the motion of particles using this method, first the net force acting on each particle is calculated. Then, Newton's second law is applied to calculate the next motion of the particles, given as:

$$a = \frac{\Sigma F}{m}, \qquad (2.36)$$

$$\Sigma F = F^c + F^{nc}, \qquad (2.37)$$

where m, ΣF, a, F^c and F^{nc} are the particle mass, net force, acceleration, contact force, and non-contact force (gravity, drag, and electromagnetic forces), respectively.

Contact forces occur when several individual particles come into contact with each other. In the discrete element method schemes, a soft contact model is commonly used to evaluate the contact force, as it allows overlapping particles, which occurs when particles collide with each other. The overlap exhibits both elastic and non-elastic properties, represented as a spring and a dashpot, respectively. Furthermore, the force generated by the overlap can be decoupled into normal and tangential components. In this study, a damped linear spring model is used to describe the contact force in the normal and tangential directions. As shown in Figure 2.7, an applied contact model comprises a spring and a dashpot for the

normal component. For the tangential component, a slider is added to describe the tangential sliding. Based on this model, contact force F^c can be written as:

$$F^c = F_n^c + F_s^c,$$ (2.38)

$$F_n^c = -k_n \delta_n \hat{n} + C_n v_{rel,n},$$ (2.39)

$$F_s^c = \min(\mu_f |F_n|, k_s \delta_s + C_s |v_{rel,s}|) \hat{s},$$ (2.40)

where k, δ, C, v_{rel}, and μ_f are the stiffness of the spring, overlap displacement between the particles, damping coefficient, relative velocity, and friction coefficient, respectively. Subscripts n and s indicate normal and tangential components, respectively. $\hat{N}$ and $\hat{s}$ are the unit vectors for normal and tangential directions, respectively. The normal and tangential unit vectors are determined as the direction towards other particles and the relative velocity except for normal relative velocity, respectively. The tangential stiffness of the spring and the damping coefficient are proportional to the normal component values.

The values of k_n and C_n should be determined carefully considering they can affect the overall dynamics in the discrete element method. In the standard discrete element method, the values of k_n and C_n depend on the physical properties of the particle such, as Poisson's ratio, Young' modulus, and restitution coefficient (Mishra and Cheung 1999). The spring stiffness is given as:

$$k_n = 0.094E^*R^*, \tag{2.41}$$

$$\frac{1}{E^*} = \frac{1-\nu_1^2}{E_1} + \frac{1-\nu_2^2}{E_2}, \tag{2.42}$$

$$\frac{1}{R^*} = \frac{1}{R_1} + \frac{1}{R_2}, \tag{2.43}$$

where ν, E, and R indicates Poisson's ratio, Young's modulus, and particle radius, respectively. The subscript 1 and 2 denotes each colliding particle. This method was established subject to assumption that the nonlinear relationship between overlap and force can be interpreted linearly when the overlap is relatively small. The damping coefficient is determined by the coefficient of restitution ε directly using the following equations:

$$C_n = \sqrt{\frac{4m^*k_n}{1+\beta_C^2}}, \tag{2.44}$$

$$\beta_C = \frac{\pi}{\ln(\varepsilon)}, \tag{2.45}$$

$$\frac{1}{m^*} = \frac{1}{m_1} + \frac{1}{m_2}, \tag{2.46}$$

The value of the tangential damping coefficient was same as that of the normal damping coefficient (Tsuji et al., 1992).

Particle motion includes both translational and rotational motions. The rotational motion of a particle is determined by the equation of rotational motion, which includes rolling friction based on the directional constant torque model (Eqs. (2.47–2.49)) (Ai et al., 2011). The direction of the torque of the rolling friction is always opposite to the relative rotation between the two colliding particles.

$$A_{ac} = \frac{\Sigma \tau}{I},$$ (2.47)

$$\Sigma \tau = R \times \Sigma F + M^r,$$ (2.48)

$$M^r = -\frac{\omega_{rel}}{|\omega_{rel}|} \mu_r R^* |F_n|,$$ (2.49)

where α_{ac}, $\Sigma \tau$, I, M^r, ω_{rel}, and μ_r are the angular acceleration, net torque, moment of inertia, torque of rolling friction, relative angular velocity, and rolling friction coefficient, respectively.
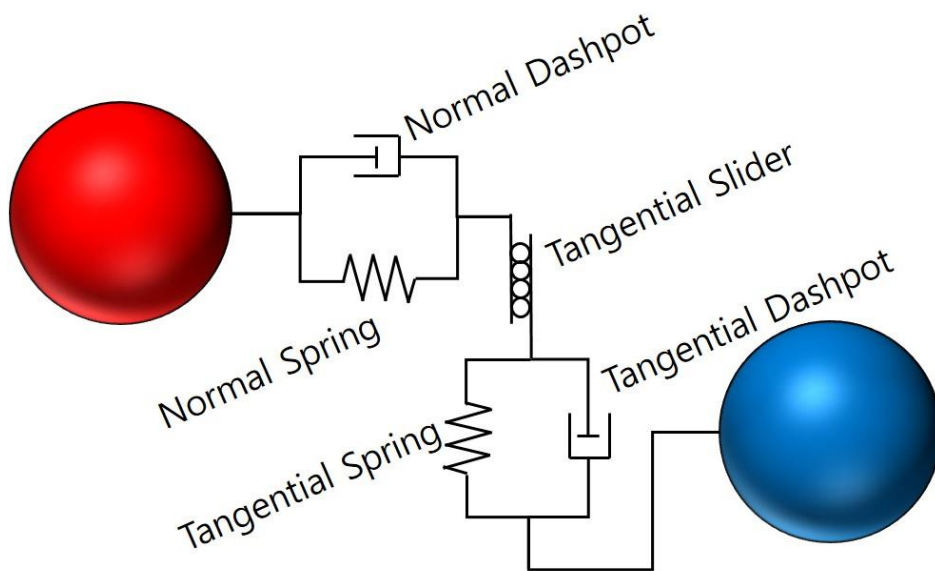
Figure 2.7. Contact force model for two colliding particles.

Chapter 3. Integration of the DEM Model into the Grinding Kinetics Model

Although the grinding kinetics model is useful for understanding the grinding characteristics considering it provides the analysis of data-tendency in a phenomenological perspective, it does not resolve the machine-dependent changes in mechanical perspective. The DEM model analyzes interactions between elements inside the mill, and hence, the changes in the collision energy spectrum inside the mill with respect to the mill-dependent condition, such as the mill dimension and operating conditions can be analyzed. Therefore, by using the DEM model, it is possible to decouple the breakage characteristics into machine- and material-dependent characteristics.

3.1. Ball Mill Operating Variables

Table 1 summarizes the mill dimensions and operating variables used for ball mill grinding simulation using the DEM model. The mill, ball media, and rocks were implemented as DEM elements in the simulations. A cylindrical mill with an internal diameter and length of 200 and 160 mm, respectively, was used. The mill was filled with a ball loading (J) with a volume fraction of 0.2, and rocks with the fractional interstitial filling of void space of the ball bed (U) was set to 0.5 according to a previous studies (Austin et al., 1984; Kwon et al., 2016). The mill rotational speed was set to 70% of its critical speed (φ_c), which is defined as the mill rotational speed

at which the ball media rotates along the mill case with the assumption of no-slipping, and is calculated by balancing gravity and centrifugal force when the ball is located on top of the mill, expressed as:

$$m(D - d)\omega^2 = 2mg_{ac},\qquad(3.1)$$

where m, D, d, ω, and g_{ac} are the mass of the ball media, radius of the mill and the ball media, angular velocity of the mill, and the gravitational acceleration, respectively. If Eq. (3.1) is rearranged, the critical speed (in rpm) can be expressed as:

$$\varphi_c = \frac{60}{2\pi}\sqrt{\frac{2g_{ac}}{D-d}} = \frac{42.2}{\sqrt{D-d}},\qquad(3.2)$$

Furthermore, 8 isosceles trapezoid-shapes lifters were equally spaced along the mill case. The length of the parallel sides of the lifters was set based on the angle from the midpoint. The angle for the lower and upper sides were $\pm1.8°$ and 80% of the lower side, respectively, and the height of the trapezoid was 12 mm. Figure 3.1 shows the shape and size of the lifter.

A single particle size fraction with size intervals of $\sqrt{2}$ was used for numerical grinding tests. However, even for a single-size fraction sample, not all particles were of the same size. Therefore, a mixture of particles classified into five sizes at constant ratios from 1 to $2^{0.4}$ for the top size were used as a starting feed, and the weight fraction of each size was set to 0.2. The top size of the feed was varied from 3.34–9.44 mm to analyze the difference depending on the particle size. Subject

to these conditions, the number of DEM particles was 70 for the ball media and approximately 500–10 000 for the rock depending on the size of the feed.
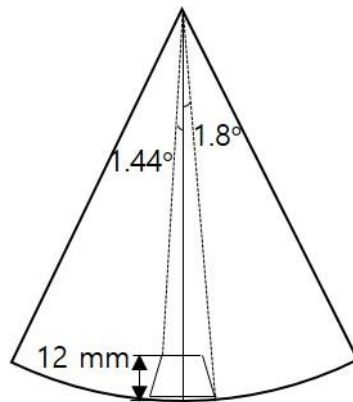
Figure 3.1. Shape and size of the lifter in the ball mill.

Table 3.1. Mill design and operational conditions of the ball mill

Components	Detailed components	Value
Mill	Diameter (mm)	200
	Length (mm)	160
	Volume (cm^3)	5024
	Rotational speed	70% of critical speed
	Number of lifters	8
	Lifter size	12% of mill radius
Ball	Diameter (mm)	25.4
	Formal ball filling, J	0.2
	Number of DEM particles	70
Rock	Diameter (mm)	3.34–9.44
	Formal powder filling, U	0.5
	Number of DEM particles	500–10 000

3.2. Parameters Used for the DEM Simulations

Several physical property values are required to calculate the equation of motion in chapter 2.3. Table 3.2 lists the parameters used in this study. All parameters were set to reflect the physical properties of the material or the values in previous studies (Bian et al., 2017; Cleary et al., 2018). The value of Young's modulus was set to approximately $1/100$ of the actual value. As this value decreased, the simulation time interval increased, which decreased the time required for simulation. However, the time interval should be small enough to maintain numerical stability. In the DEM scheme, the time interval is determined based on the contact duration calculated analytically from the reduced mass and spring constant. If the damping coefficient is zero, i.e., the collision is perfectly elastic, the contact duration is given as:

$$T = \pi \sqrt{\frac{m^*}{k_n}}, \qquad (3.3)$$

where T is the contact duration. The time interval is proportional to the contact period, and the proportionality constant is typically $1/20$ to $1/30$. In this study, the time interval considered was $1/30$ of the contact period. In Eqs. (2.22) and(2.23), the normal spring constant was calculated from Young's modulus. As Young's modulus decreased, the normal stiffness of spring is decreased, which increased the contact period and time interval. Therefore, a value smaller than the real Young's modulus is advantageous in terms of the time required for simulation. Conversely, the assumption that the length of the overlap and spring force are linear should be maintained owing to the increase in the overlap length. Additionally, as

described in the next section, the dissipation energy affecting the particle breakage is calculated by using the damping coefficient in Eq. (2.25). Considering the reduced Young' modulus does not affect the dissipation energy, it is reasonable to change the Young's modulus to decrease the simulation time.

Table 3.2. Parameters used for simulation using the DEM

Physical properties	Value
Coefficient of restitution (rock–rock)	0.3
Coefficient of restitution (rock–steel)	0.5
Coefficient of restitution (steel–steel)	0.8
Friction coefficient	0.5
Poisson's ratio	0.2
Coefficient of rolling friction	0.02
Young's modulus (rock)	500 MPa
Young's modulus (steel)	2000 MPa
Specific gravity (rock)	3.5 g/cm^3
Specific gravity (steel)	7.8 g/cm^3

3.3. DEM Schemes

The DEM simulation was conducted in two stages, as shown in Figure 3.2. During the preparation stage, the particles were generated and stacked on the bottom of the mill chamber to attain a stable state after a free fall. In the second stage, the mill began to rotate, and the information of collision energy with time was recorded and analyzed. Additionally, the state of the mill motion was changed abruptly, which affected the number of particles that broke. Therefore, it is necessary to determine whether to contain the collision that occurs before the initial stabilization in the simulation result. Depending on the change in the average velocity of each particle group over time, it was confirmed that the time required to reach a stable state was approximately 3 to 4 s (Figure 3.3). Therefore, the dissipation energy affecting particle breakage was conservatively recorded 5 s after the onset of the simulation.
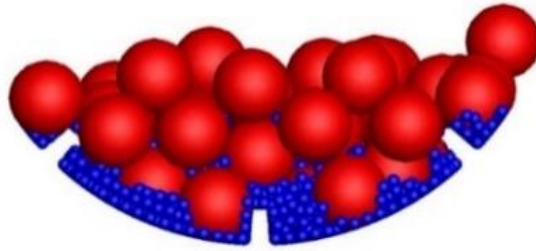
(a)
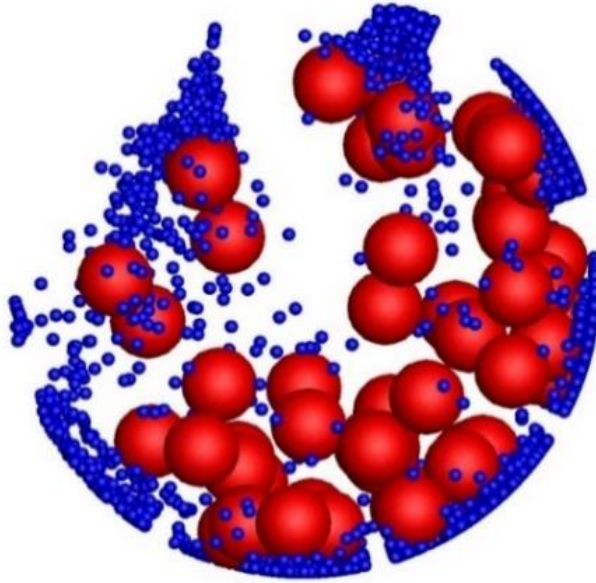
(b)

Figure 3.2. Ball mill representations at different simulation stages. (a) Particle

generation stage and (b) Mill rotation stage.
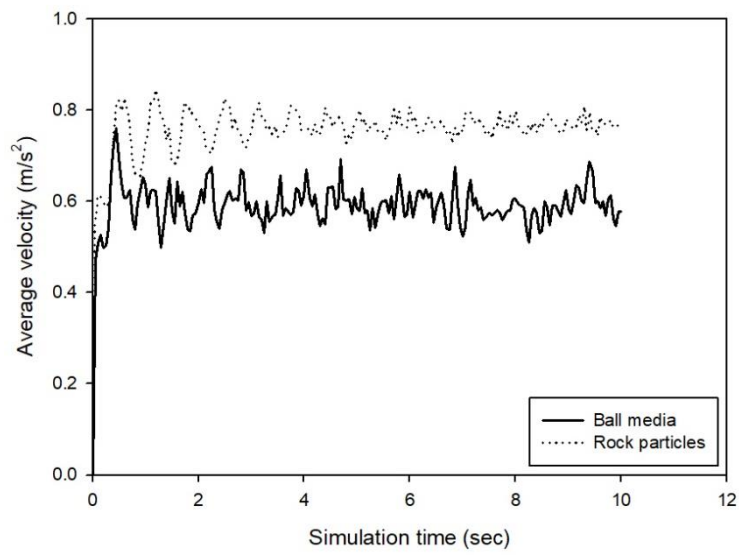
Figure 3.3. Average velocity for the ball media and rock particles over simulation

time.

It is important to determine the collision energy considering it is directly related to the occurrence of breakage of particles within the model. The collision energy can be determined from different perspectives, such as the kinetic energy at the time of impact (Mori et al., 2004; Iwasaki et al., 2010), dissipated energy (Mishra and Rajamani, 1992; Mishra and Rajamani 1994; Datta et al., 1999; Hlungwani et al., 2003), and the maximum impact energy (Wang et al., 2012). In this study, given the collision energy is the energy that affects the breakage of particles, the analysis was performed using the dissipation energy, which in turn is calculated as the numerical integration of the product of the damping force and the particle displacement during time interval.

$$E_d = \int_0^{T_c} F_d v_{rel,n} dt, \qquad (3.4)$$

where E_d, F_d, and T_c are the dissipation energy, damping force, and contact time, respectively. When slipping occurs in the tangential direction, the friction force is used instead of the damping force. Because the dissipation energy is calculated for each particle, it must be allocated to satisfy the energy conservation law. When rock particles collide with each other, the dissipation energy splits into two and is assigned to each rock particle to simplify the problem. In the collision between the ball media and rock particle, 90% of the dissipation energy is allocated to the rock particle based on the previous research (Cleary et al., 2018).

Figure 3.4 shows the fundamental algorithm of the simulation of mill rotation step. The part that determines whether or not particles are broken is introduced to the typical DEM simulation process for analysis. The analysis of the particle breakage

potential is performed 5 s after the simulation begins. Eq. (3.5) demonstrates the probability of particle breakage owing to n collisions, which is transformed from Eq. (2.33) and (2.35). If the dissipation energy is less than the threshold energy, the collision has no effect on the particle breakage. Conversely, the difference between the two values was used to calculate the probability of particle breakage. Instead of the sum of the effective energies, the difference in energy at each collision was used to determine whether to break at each collision.

$$P_B = 1 - \exp\left\{-\frac{(E_k - E_0)}{E_b}\right\}, \qquad (3.5)$$

where E_b is the energy representing the particle strength that normalizes the applied energy by collision and affects the probability of particle breakage. For convenience purposes, some studies considered this value as a constant (Cleary et al., 2018). However, considering Eq. (3.5) is a modified form of Eqs. (2.33) and (2.35), E_b should depend on the particle size, and should be related to parameter f_{Mat}. According to Shi (2016), f_{Mat} is size dependent, given as:

$$f_{Mat} = p_f x^{-q_f}, \qquad (3.6)$$

where p_f and q_f are the model parameters that can be determined through breakage tests. Therefore, it can be inferred that E_b can be expressed by:

$$E_b = p_E x^{-q_E}, \qquad (3.7)$$

where p_E and q_E are model parameters. Eq. (3.7) demonstrates that as the particle size increases, E_b and the strength of the particle decrease infinitely. However, the correlation between particle size and strength eventually converge, although the strength decreases as the particle size increases (Tavares and King, 1998). Mathematically, it is expressed as:

$$E_{50} = E_\infty \left\{ 1 + \left(\frac{x_{0,f}}{x_i} \right)^\chi \right\},$$
(3.8)

where E_{50}, E_∞, $x_{0,f}$, and χ are the mass-specific median particle fracture energy, fracture energy at coarse size, size of the fracture energy that is twice the convergence value, and the slope of the size-fracture energy plot, respectively. In this study, Eq. (3.8) was used to describe the relationship between the size and strength.

After calculating the particle breakage probability, the probability was compared with random numbers between 0 and 1. It was found that the particle broke when the probability was higher than the random number. As the simulation progressed, each particle underwent repeated collisions, and the breakage of the particles was recorded for each collision. Finally, the simulation results were interpreted based on the rate process. The first-order breakage was confirmed by plotting the change in weight fraction remaining at the top size class over time in log-linear scale. In this study, the effect of changes in the particle size distribution in the mill and particle weakening owing to repeated collisions on the first-order kinetics were investigated.
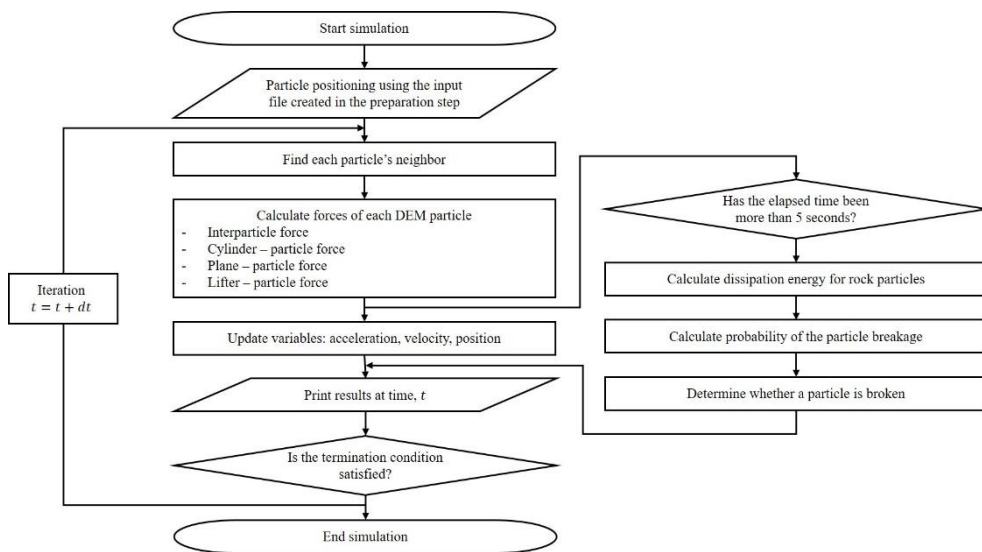
Figure 3.4. Flowchart of the DEM code.

3.3.1. Particle Weakening Simulation Method

There are various models that describe particle weakening or incremental damage caused by repeated collisions (Cleary and Morrison, 2016; Tavares and King, 2002; Han et al., 2003). In this study, the particle weakening model proposed by Tavares and King (2002) were used considering it can effectively describe material weakening using a single parameter. The model is derived from the reduction in stiffness through repeated impacts in the force-displacement profile. The relationship between the mass-specific fracture energies owing to successive impacts is expressed as:

$$E_{f,n} = E_{f,n-1}(1 - D_n), \tag{3.9}$$

where $E_{f,n}$ and $E_{f,n-1}$ are the mass-specific fracture energy of the particle before and after nth collision, respectively. D_n is the amount of damage received by the nth collision and is given as:

$$D_n = \left\{ \frac{2\gamma_D}{(2\gamma_D - 5D_n + 5)} \frac{E_k}{E_{f,n-1}} \right\}^{\frac{2\gamma_D}{5}}, \tag{3.10}$$

where γ_D is the damage accumulation constant and determined through experiment. Considering D_n is implicit in Eq. (3.10), an iterative method should be used. This study used the bisection method. The energy value E_k in Eq. (3.1) should be replaced with a corresponding value, so that the difference $(E_k - E_0)$, which is the energy available to break particles, can be substituted to calculate the damage. E_b in Eq. (3.8) corresponds to $E_{f,n-1}$ in Eq. (3.10) considering they both are related to

the particle strength. However, if the difference $(E_k - E_0)$ is to the same as E_b in Eq. (3.8), the probability of the particle breakage is approximately 63% or more, which indicates that the particle may not be broken. Then, if the damage is calculated using the ratio of the difference and E_b, the particle is considered too weak, which would result in unconditional particle breakage in the next effective collision. Therefore, the damage was calculated by using the value at which the particle breakage probability of Eq. (3.8) became 99% with respect to the applied effective energy. After calculating the damage, the weakening effect of the particle is expressed as:

$$E_{b,n} = E_{b,n-1}(1 - D_n),$$ \hspace{2cm} (3.11)

$$E_{0,n} = E_{0,n-1}(1 - D_n),$$ \hspace{2cm} (3.12)

where subscripts n and $n - 1$ indicate the parameter changes before and after the nth collision, respectively.

3.3.2. Progeny Particle Size Distribution

As described in Section 2.1, a progeny particle size distribution can be determined using the t_n-family curve. However, the size index t_{10} should be known, and is calculated as:

$$t_{10} = M\left\{1 - \exp\left(\frac{E_k - E_{0,n}}{E_{b,n}}\right)\right\},$$ \hspace{2cm} (3.13)

Eq. (3.13) shows the t_{10} value when the particle is broken by the $n + 1$th collision. Although this equation is a modified form of Eq. (2.35), the difference is that it does not consider all collision energies that have occurred because it is calculated at every collision. As seen in Eq. (2.35), the incremental damage owing to repeated collision appears in the form of a number of effective collisions. In this case, only the progeny particle size distribution changes whereas the probability of the particle breakage remains the same. In this study, by reducing E_0 and E_b based on the particle weakening effect caused by repeated collisions, the breakage probability was set to increase as the weakening progressed. Additionally, considering the previous collisions were already expressed as parameter change, the value of t_{10} can be calculated without summation, that is, there is no need to record the previous collision data.

After determining t_{10}, the t_n-family curve was used to calculate the other values of t_n. Because the t_n values are out of the geometric sequence of the size interval, it must be converted into the weight fraction for each size class, which in turn was determined using spline regression. In this case, the progeny particle cannot exist in the parent particle size class. The BII method was used to calculate the progeny particle size distribution. Furthermore, the minimum size of rock particles was set to 1.72 mm. When the broken particle was in size class j, the cumulative weight fractions from 1.72 mm (size class n) to size class $j + 1$ were calculated using the BII method. Next, the weight fraction of each size class was replaced by the number of particles. As the simulation progressed, the weight fraction of the top size decreased below the certain percentage, which stopped the simulation. Then, the

particle size distribution inside the mill was changed by performing a particle generation stage to reflect the calculated number of progeny particles.

3.4. Results

3.4.1. First-Order Breakage Kinetics

The first-order breakage kinetics indicates that the breakage rate of each size class is proportional to the weight of each size class. In the grinding kinetics model, the first-order breakage kinetics should be established to apply the analytic solution of the size-mass balance equation. Therefore, the first-order breakage kinetics in the ball mill simulation were analyzed through single-fraction breakage tests using DEM. In ball mill simulation, whenever rock particles collide, the first-order breakage kinetics determines whether the particle is broken or not. If broken, the mass of the broken particle is excluded from the calculation of the weight fraction in the top size class. The simulation is performed until the weight faction of the top size class reaches 10% of the initial mass. The breakage probability parameters xE_0 and E_b were set to 2 Jmm/kg and 8.1 J/kg, respectively.

Furthermore, it was investigated whether the first-order breakage kinetics was established when the particle size distribution inside the mill was changed as the simulation progressed. First, as shown in Figure 3.2, the rock particles comprising a single-fraction were generated in the preparation stage, and the ball mill grinding simulation was performed during the mill rotation stage. Whenever each rock particle collided, it determined whether the particle was broken depending on the collision energy and recorded the information on each particle. If the particle was

broken, the corresponding collision energy was stored in each particle. When the weight fraction of the particles unbroken in the top size class reached 70%, the fragment size distributions of all broken particles were calculated according to the stored collision energy by using t_{10} and t_n, as mentioned in Section 3.1.3.2. Then, the first simulation ends. In the next preparation step, the previously broken particles are replaced with the fragment distribution and generated with unbroken particles. Next, the ball mill simulation after the grinding time was stopped was described by repeating the simulation in the mill rotation stage. In this instance, the particle breakage was calculated after 5 s, which is the time required to reach the stable state. This process was repeated every time the weight fraction of the top size class reached 70% of the start of the mill rotation stage, and the simulation was performed until the weight fraction of the top size class reached 10% of the initial mass. Figure 3.5 shows the simulation algorithm of the change in the size distribution of the mill. As seen in Figure 3.5(b), when the weight fraction of the top size was approximately 17%, the total number of particles was approximately 12 000.

Figure 3.6 shows the change in the size distribution inside the mill. The color bar is based on the radius of the particles. Considering the ball media was large compared to the rock particles, they appeared red whereas the smallest particles appeared blue. As the weight fraction of the top size class decreased, the number of smaller particles rapidly increased.
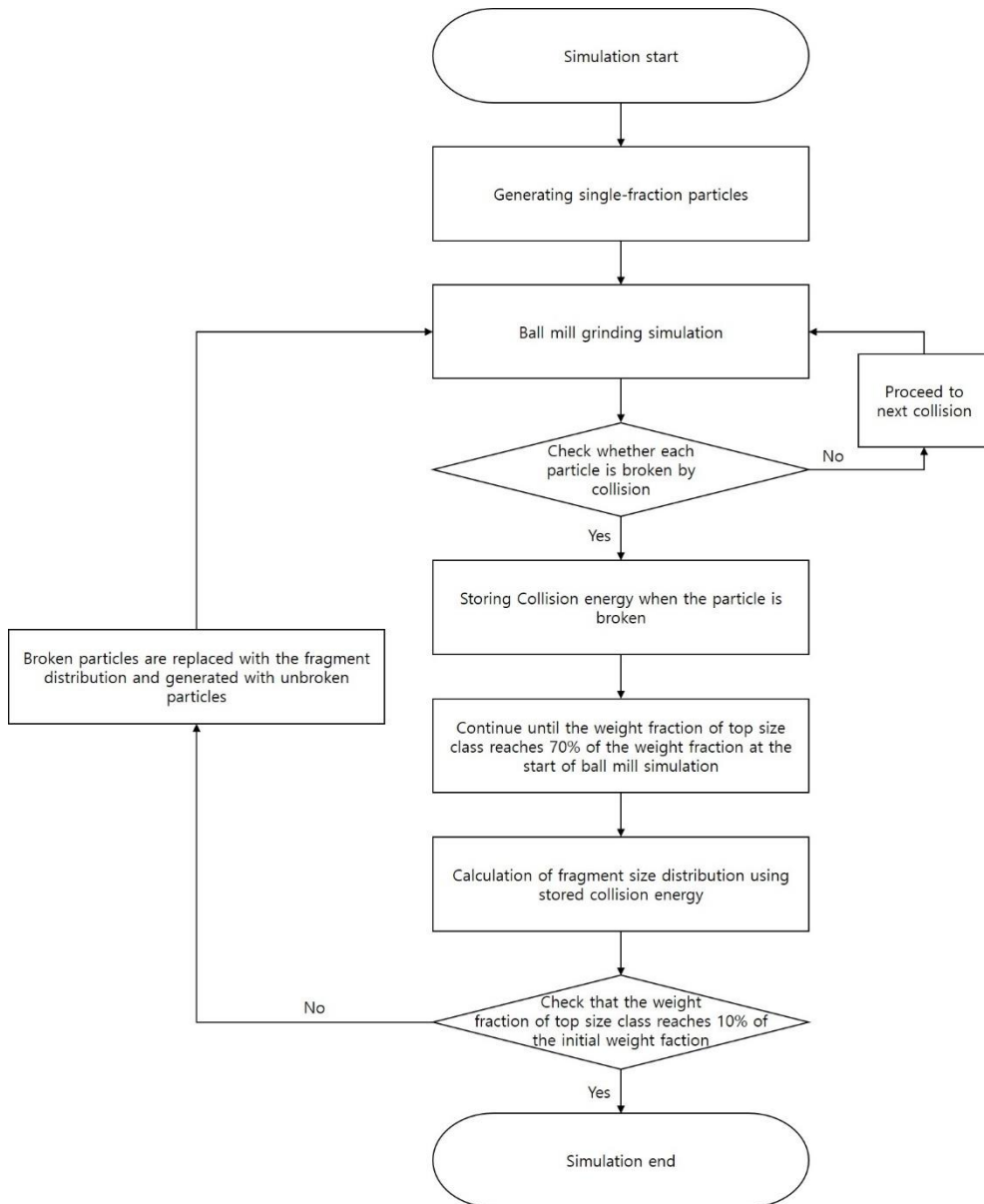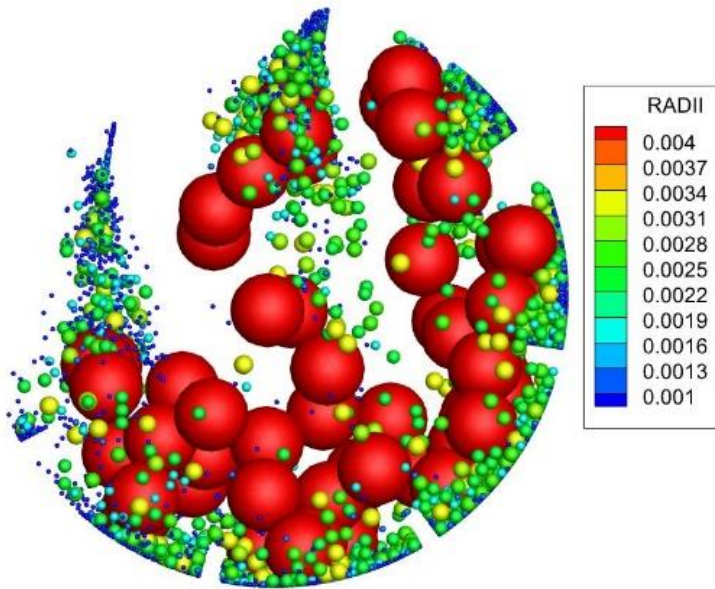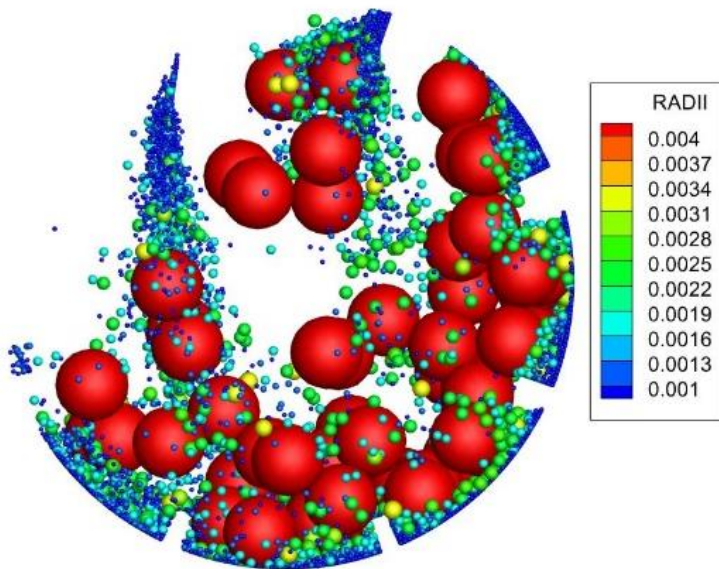
Figure 3.5. Simulation algorithm of the change in the size distribution inside the

mill.

(a)

(b)

Figure 3.6. Change in the size distribution inside the mill: (a) Weight fraction of

top size is approximately 49% and (b) Weight fraction of top size class is

approximately 17%.

The collision energy spectrum per particle can be calculated as the DEM tracks all collisions during the simulation time. The energy spectrum was derived by discretizing the energy and measuring the collision frequency for each energy class. Figure 3.7 shows the changes in the collision energy distribution of the top size class according to the particle size distribution inside the mill. The frequency of collisions with high collision energy was low considering the type of collision and ball movements that generates high collision energy was limited. The motion of the ball inside a tumbling mill can be classified into two modes, namely, cascading and cataracting stream. In the middle regime of the chamber, a ball bed is formed, and the ball raised by the lifters can roll down the surface of the bed, which is called cascading. When the ball is ejected from the lifter surface at a higher angle than the bed surface, the ball falls directly on to the bed surface or to the other side, which is called cataracting. The high collision energy is caused by the cataracting motion, which occurs relatively infrequently.
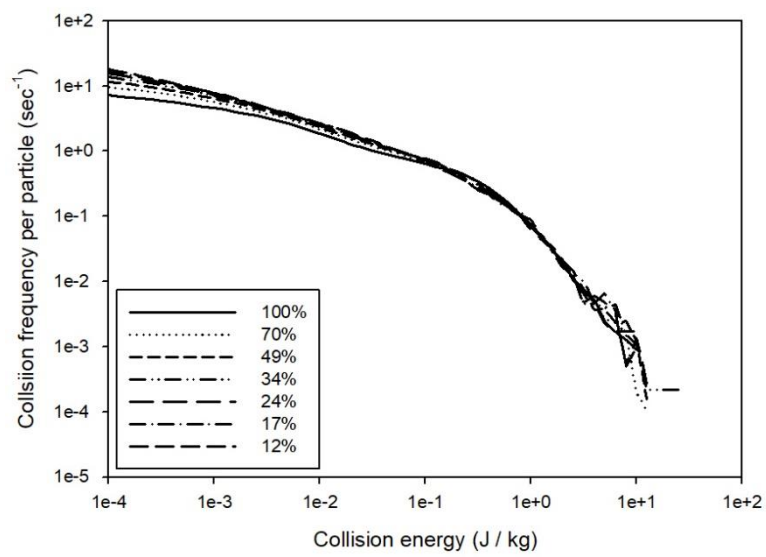
Figure 3.7. Collision frequency according to the collision energy.

As shown in Figure 3.7, almost the same collision frequency appears regardless of the weight fraction of the top size class in the high energy region, considering the collision frequency per particle is maintained even though the collision frequency decreases owing to the decrease in the number of particles of the top size class. This indicates the probability that a particle break is constant, that is, even if the particle size distribution changes with the simulation time, the probability for breaking a single particle remains constant. Therefore, changes in the number or weight of the top size over simulation time remains constant. In the low energy region, the smaller is the weight fraction of the top size class, the higher is the collision frequency, which is caused by the collisions with fragments. However, because the low energy region is smaller than the threshold energy, it has no effect on both the particle breakage and the breakage rate.

Figure 3.8 shows the rate of change of the weight fraction of the top size class with the simulation time. The rate of change appears as a straight line in the log-linear graph, regardless of the change in the particle size distribution inside the mill according to the grinding time. The specific rate of breakage can be calculated from the slope of the graph. As seen in the figure, it takes approximately 1 min for the weight fraction of top size to reach 10%, which is shorter than the grinding time for real rocks. This can be attributed to the accelerating particle breakage to ensure the simulation time does not increase significantly. Furthermore, the grinding time was reduced by decreasing the breakage probability parameter E_b. The simulation result for when the weight fraction reached 10% over about 3 min was compared with the simulation result by accelerating the breakage, which confirmed that accelerating

breakage can be used effectively to analyze the first-order breakage kinetics and the change in the weight fraction with the grinding time.
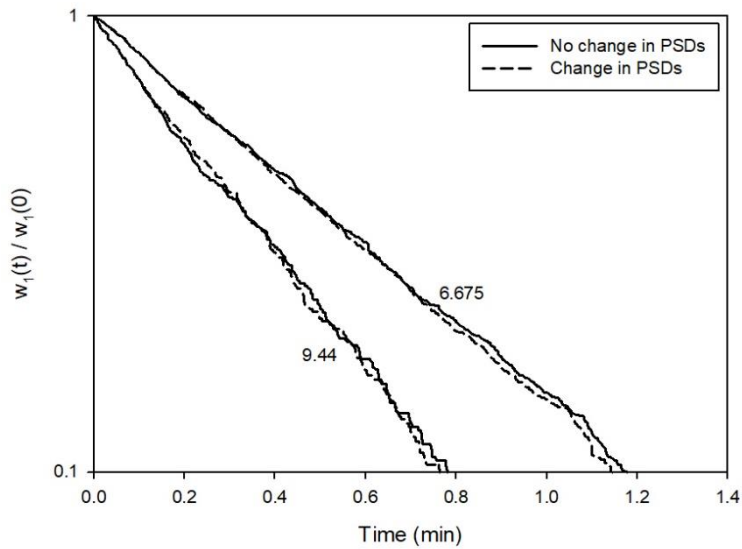

Figure 3.8. First-order breakage kinetics according to the particle size distributions (PSDs) inside the mill.

Further analysis was performed to determine the effect of changes in the particle size distribution inside the mill for a particle size of 6.675 mm. First, the particle size distribution was changed whenever the weight fraction of the top size class reached 80% of the value at beginning by shortening the fragments regeneration cycle. This made the particle size distribution similar to the actual one. Next, the first-order breakage kinetics were analyzed when M, representing the maximum value of t_{10} in Eq. (3.14), changed. Even if the particle broke owing to the same energy, if M is large, t_{10} increases. As a result, the fragment size distribution determined by t_n-family curve becomes finer. Figure 3.9 shows the change in the ratio in the weight fraction of the top size class with the grinding time for each case. The graph appears identical to the previous result, and hence, the first-order breakage kinetics can be established no matter how the particle size distribution inside the mill changes.
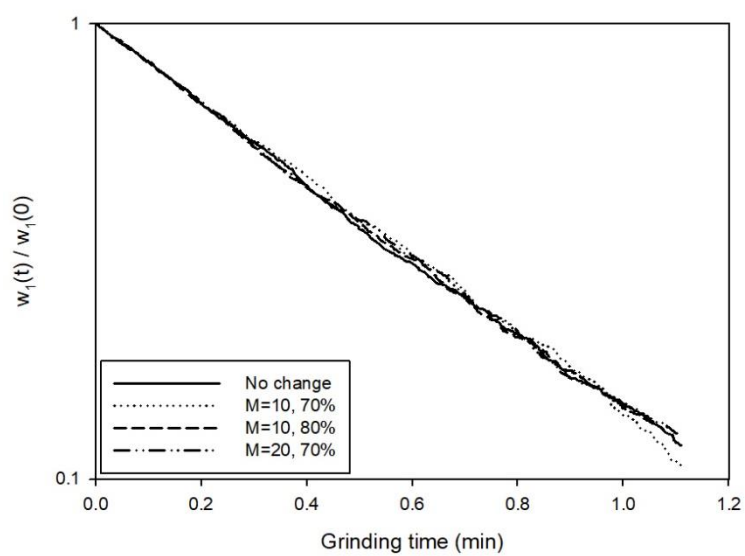
Figure 3.9. First-order plot for various conditions of the particle size distribution

inside the mill.

3.4.2. Particle Weakening

As the simulation progresses, the rock particles collide repeatedly, causing an increase in both the number of weakened particles and the degree of weakening of each particle. Therefore, the weakening effect increases the breakage rate. Figure 3.10 shows the change in the weight fraction of top size class when the weakening effect is applied to the various particle size. It was confirmed that when the weakening effect is applied for all particle sizes, the breakage rate increased with the grinding time. To compare the weakening effect quantitatively, the area surrounded by 3 lines (x = 0, y = 0.1, and the graph of weight fraction change) were calculated, which after applying the weakening effect was similar at approximately 74% regardless of the particle size, compared to before the weakening effect.

As shown in Figure 3.10, γ_D is set to 2, indicating that the weakening effect occurs even at low energies, as shown in Figure 3.11. Figure 3.11(a) shows the effect of the damage coefficient. In the case of a large γ_D, if the collision energy is lower than the fracture energy, a relatively low weakening effects occurs. Therefore, the larger the damage coefficient, the slower is the increase in breakage rate, whereas the change in the weight fraction of the top size class with the grinding time becomes more linear, as shown in Figure 3.11(b).
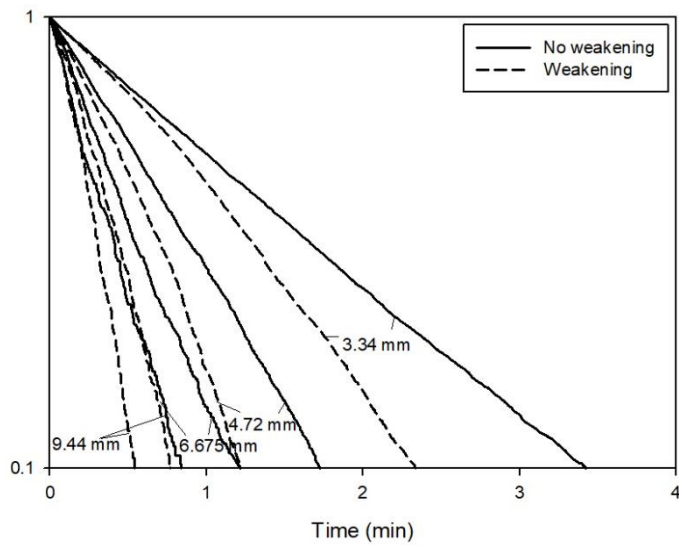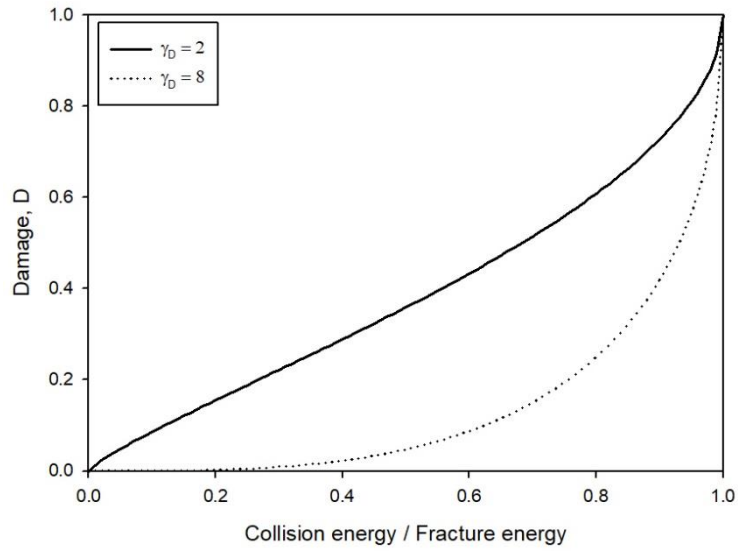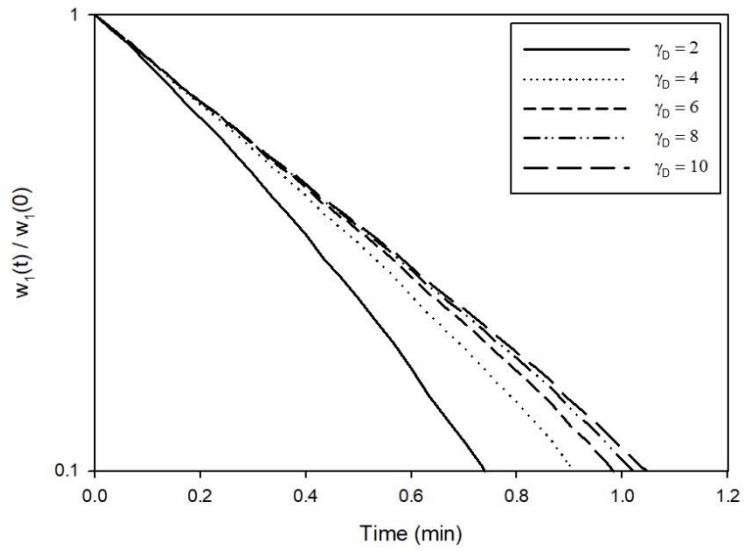
Figure 3.10. Changes in the breakage rate when the weakening effects is applied.

(a)

(b)

Figure 3.11. Effect of the damage coefficients. (a) Changes in the damage and (b)

Changes in the weight fraction of the top size class with the grinding time.

3.4.3. Calculation of the Breakage Rate

During DEM simulation, all collision energies for each particle can be obtained, indicating that the machine-dependents are determined. Therefore, by changing the material-dependents, the breakage rate of the samples with different breakage properties can be calculated. For this, it is necessary to calculate the breakage rate from the energy distribution of the DEM simulation. First, based on the energy distribution of each particle, the change in the weight fraction of the top size class over time was determined when simulating the particle breakage in a manner similar to the simulation. The collision energy and collision time were obtained for each particle from the DEM for effective collisions, where the collision energy was higher than the threshold energy. Then, the survival probability was calculated for collisions that occur within a given time. Herein, unlike the simulation where the particle breakage is determined through comparison with a random number, the weight fraction remaining in the top size class was calculated using the expected value for particle survival. Figure 3.12 shows that the calculated results according to the grinding time agree well with the simulated results.
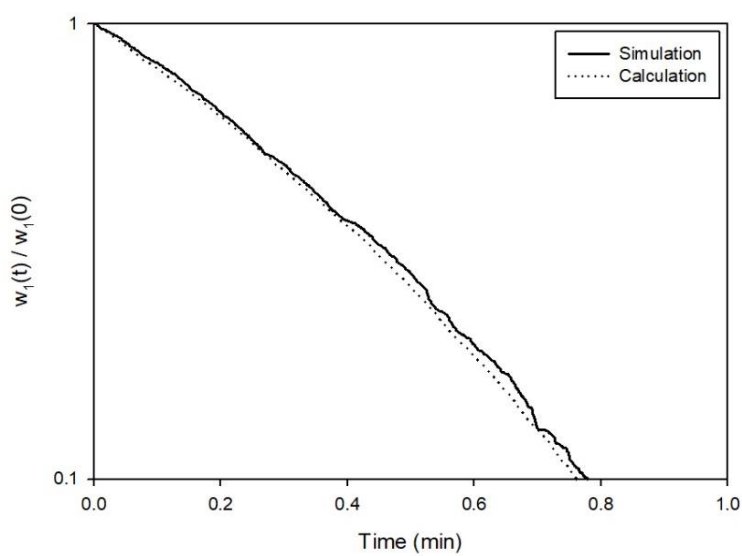
Figure 3.12. Comparison of the changes in the weight fraction over time between

the calculation and simulation results.

Although the same result as the simulation in Figure 3.12 was obtained, the simulation must be performed to obtain the required data. Therefore, for using the model effectively, it should be possible to calculate the breakage rate from the basic energy data, that is, the energy distribution when the particle breakage and weakening effects do not work. Using this data, the change in the weight fraction over time when the particle breakage and weakening effects were applied was calculated in the following processes. First, the total effective collision energy that occurred within a given time was calculated, followed by the damage using the total energy. After updating the breakage probability parameters E_0 and E_b, the total energy was recalculated considering the effective energy section is extended. Furthermore, the expected value of the weight fraction remaining in the top size class over time for all particles was determined as:

$$E_{total}(t) = \sum_{k=1}^{N_t}(E_k - E_0),$$
(3.14)

$$D = \left\{ \frac{2\gamma_D}{(2\gamma_D - 5D + 5)} \frac{E_{total}}{E_{f,0}} \right\}^{\frac{2\gamma_D}{5}},$$
(3.15)

$$P_S = \exp\left(\frac{E'_{total}}{E'_b}\right),$$
(3.16)

$$E_S(t) = \frac{\sum_{i=1}^{n}\left[w_i \exp\left(\frac{E'_{total}(t)}{E'_b}\right)\right]}{\sum_{i=1}^{n} w_i},$$
(3.17)

where $E_{total}(t)$, N_t, $E_{f,0}$, E'_{total}, E'_b, and $E_S(t)$ are the sum of the effective energy for given time t, number of effective collisions for time t, initial particle fracture energy, recalculated sum of the effective energy by using updated threshold

energy E_0', an updated parameter, and the expected remaining weight fraction in top size class for a given time, respectively. For basic energy data, it is possible to successfully describe the change in the weight fraction by applying the particle weakening effect, as shown in Figure 3.13.
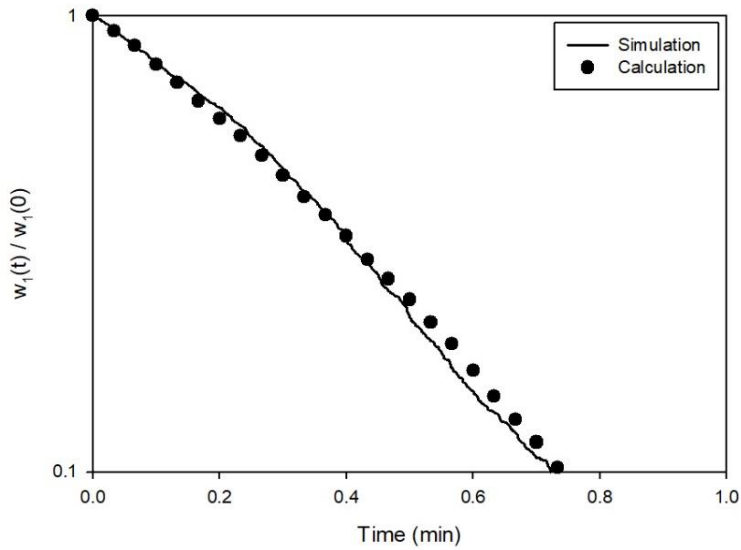

Figure 3.13. Calculation results of weakening from the basic energy data

3.4.4. Relationship Between the Breakage Rate and Breakage Probability Parameters

The breakage probability parameter has a direct relationship to the breakage of the particle. That is, it is closely related to the tendency of particles in the top size class to disappear, the specific rate of breakage. The breakage rate represents the rate of change in the weight fraction of each particle size class with the grinding time. In the single-fraction test, the weight fraction of the top size class at time t is expressed as shown in Eq. (2.2). The breakage probability is a calculated value for a single particle, and the expected survival value is the weight fraction remaining in the top size class. In this case, the average collision energy is similar to the breakage rate. The weight fraction remaining in the top size class according to the number of collisions is expressed as:

$$E_i(N_t) = \exp\left\{-\frac{\overline{(E-E_0)_i}}{E_b}N_t\right\},$$
$$(3.18)$$

where $E_i(N_t)$ and $\overline{(E-E_0)_i}$ are the weight fraction remaining in the top size class of particle i according to the number of collisions and the average effective energy for N_t collisions of ith particle, respectively.

To analyze the relationship between the breakage probability parameters and breakage rate, Eq. (3.18) is modified to a time-dependent equation. By multiplying the frequency of effective collision, Eq. (3.18) is transformed to:

$$E_i(t) = \exp\left\{-\frac{f\overline{(E-E_0)_i}}{E_b}t\right\},$$
$$(3.19)$$

where f is the frequency of collision, which is higher than the threshold energy, and $E_i(t)$ is the weight fraction remaining in the top size class with the grinding time.

On comparing Eqs. (3.19) and (2.2), it was seen that the term inside the exponential function had the same meaning as the breakage rate. However, given that the breakage rate represents the change in the weight fraction of all particles in the specific particle size class, the average of all particles should be calculated. Mathematically, it is given as:

$$S = -\ln\left[\frac{\sum_{i=1}^{n} w_i \exp\left\{-\frac{f\,(E-E_0)_i}{E_b}\right\}}{\sum_{i=1}^{n} w_i}\right], \tag{3.20}$$

Even in a single-fraction test, owing to the difference between the particle masses within a class, the breakage rate should be calculated using the weight average. The breakage rates calculated using Eq. (3.20) and obtained from the slope of the first-order plot were approximately same, with values 2.05 and 2.07, respectively, when the particle size, xE_0, and E_b were set to 6.675 mm, 2 Jmm/kg, and 8.1 J/kg, respectively. Figure 3.14 shows that the estimated and simulated values are in good agreement for various breakage probability parameters.
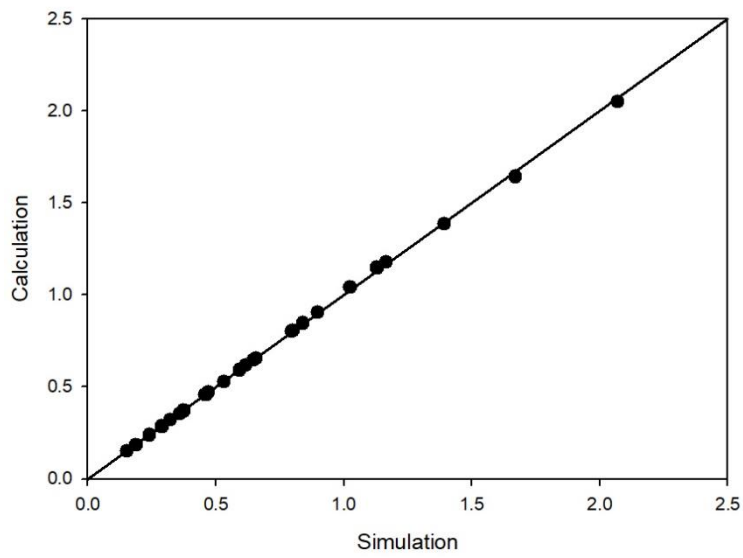
Figure 3.14. Comparison of the specific rate of breakage for the calculated and

simulation values.

Assuming the particle size in the top size class can be represented by a specific value, such as median particle size, Eq. (3.20) can be simplified to Eq. (3.21) for two cases where Eq. (3.22) holds. First, where the breakage rate is sufficiently small, that is, the terms in the exponential function are small, so that the exponential function can be assumed to be linear. And second, where the dispersion of energy applied by the particles in the top size class is very small, indicating that the particles receive almost the same energy.

$$S = \frac{f\,(E-E_0)}{E_b},\qquad (3.21)$$

$$\frac{\sum_{i=1}^{n}\exp\left\{-\frac{f\,(E-E_0)_i}{E_b}\right\}}{n} \cong \exp\left[\frac{\sum_{i=1}^{n}\left\{-\frac{f\,(E-E_0)_i}{E_b}\right\}}{n}\right],\qquad (3.22)$$

In Eq. (3.21), the relationship between the breakage rate and breakage probability parameter is easily understood, especially E_b, which can be calculated from Eq. (3.8) using the material properties obtained through experiments. Substituting Eq. (3.8) into Eq. (3.21) provides Eq. (3.23). Taking the logarithm of both sides and rearranging the equation provides Eq. (3.24). If x_i is sufficiently smaller than $x_{0,f}$, Eq. (3.24) can be modified to Eq. (3.25).

$$S = \frac{f\,(E-E_0)}{E_\infty\left\{1+\left(\frac{x_{0,f}}{x_i}\right)^{\chi}\right\}},\qquad (3.23)$$

$$\log(S) = \log\left(\frac{f\,(E-E_0)}{E_\infty}\right) - \log\left\{1+\left(\frac{x_{0,f}}{x_i}\right)^{\chi}\right\},\qquad (3.24)$$

$$\log(S) = \log\left(\frac{f\,(\bar{E}-E_0)}{E_\infty}\right) + \chi \log\left(\frac{x_i}{x_{0,f}}\right), \qquad\qquad (3.25)$$

From Eqs. (3.23) to (3.25), the relationship between the material property and the breakage rate can be analyzed. First, in the case of E_∞, it is inversely proportional to the breakage rate and A in Eq. (2.2). However, in the case of χ, if the particle size is small enough, it becomes the slope in the log-log plot of the breakage rate and relative particle size. That is, α in Eq. (2.2) is closely related to the χ.

First, the relationship between E_∞ and the breakage rate was analyzed. The change in the breakage rate for various E_∞ was plotted on a log-log scale graph. Considering E_∞ and the breakage rate are inversely proportional, the slope of the graph was calculated as -1. The graph comparing the same E_∞ with different E_b by changing $x_{0,f}$ and χ is shown in Figure 3.15. Herein, xE_0 is 2 Jmm/kg and the particle size is 6.675 mm.
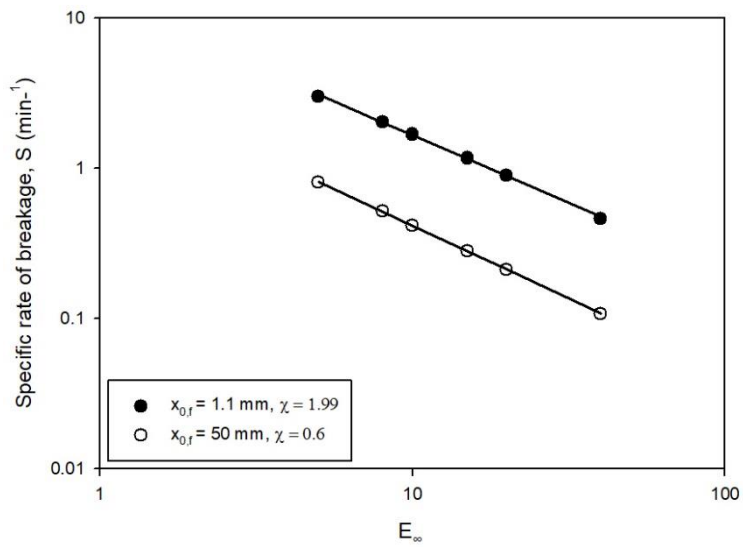
Figure 3.15. Relationship between E_∞ and the breakage rate for different $x_{0,f}$

and χ.

In both cases, the graph appears linear; however, the slope differs by -0.90 and -0.97, respectively. Particularly, when $x_{0,f}$ and χ are 50 mm and 0.6, respectively, which is the case for larger values of E_b, the slope is close to -1 to establish the relationship between the breakage rate and E_∞ identified in Eq. (3.25). For the same energy distribution, the breakage rate decreases as E_b increases. That is, the exponential function is assumed to be linear as the breakage rate decreases.

Additionally, the case where the particle size and xE_0 change were analyzed. In both cases, a decrease in the breakage rate and a change in the energy distribution worked in combination. Simulations were performed for the cases where the particle size was 6.675 and 4.72 mm, and xE_0 was 2 and 6 Jmm/kg (Figure 3.16).
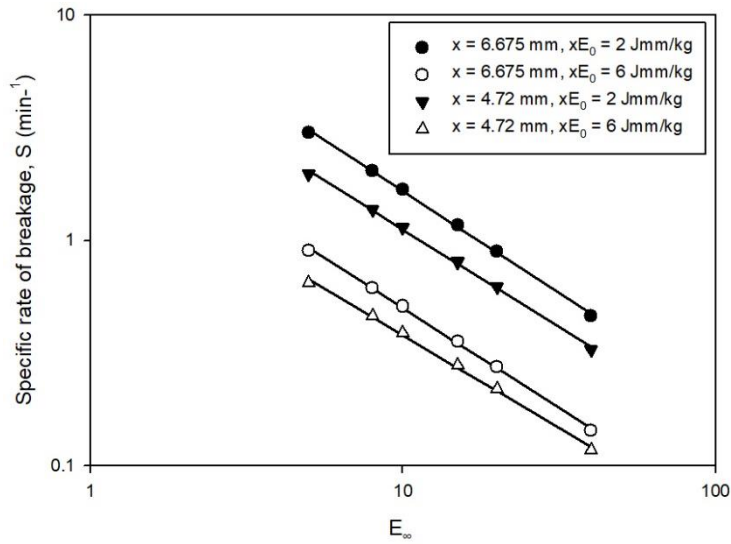

Figure 3.16. Relationship between E_∞ and the breakage rate for different particle sizes and xE_0.

Although a linear graph was observed in all cases, differences were observed in the slopes, which were not close to -1. When xE_0 increased from 2 to 6 Jmm/kg, the breakage rate and absolute value of the slope decreased, indicating that Eq. (3.22) does not hold, and the change in energy distribution has a greater effect than the change in the breakage rate. This also occurs when the particle size changes. As the particle size decreases, the breakage rate and absolute value of the slope of the graph decrease. Figure 3.17 shows the histogram of the average collision energy for each particle in each case.
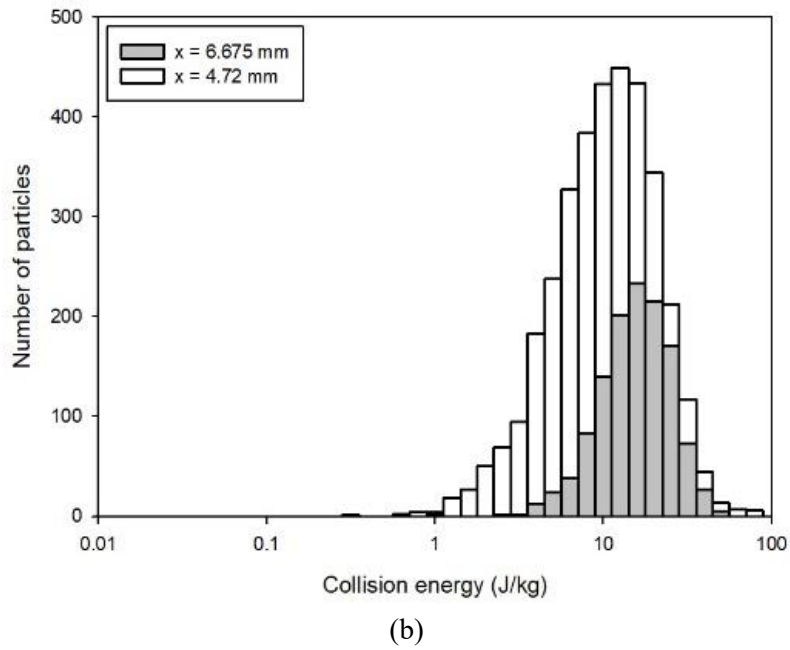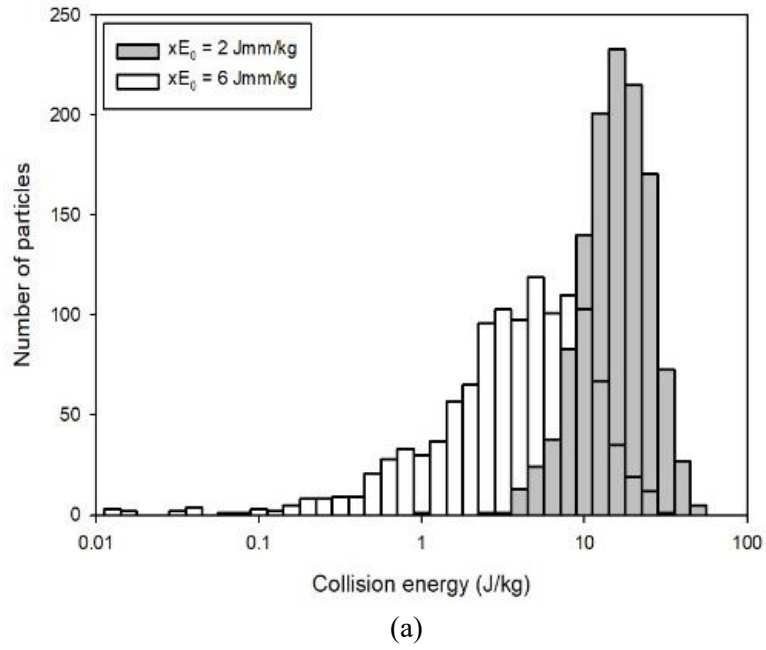
(a)

(b)

Figure 3.17. Histogram of the average collision energy. (a) Change of xE_0 and (b)

Change of particle size.

Figure 3.17 shows the number of particles for each energy class according to the log-scale energy class. As xE_0 increased, the average energy decreased and the energy distribution dispersed, as shown in Figure 3.17(a). The same result is shown in Figure 3.17(b) for when the particle size decreases. The breakage rate decreased as E_b increased and average energy decreased.

The breakage rate parameter α is related to χ in the Eq. (3.25). However, considering the frequency and energy distribution are also functions of particle size, α does not exactly correspond to χ. Figure 3.18 shows the change of α with χ for particle sizes ranging from 3.34–9.44 mm. In this case, $x_{0,f}$ was set to 50 mm to simulate a region where E_b is linear according to the particle size. Additionally, the graph in the case of different values of E_∞ was plotted.
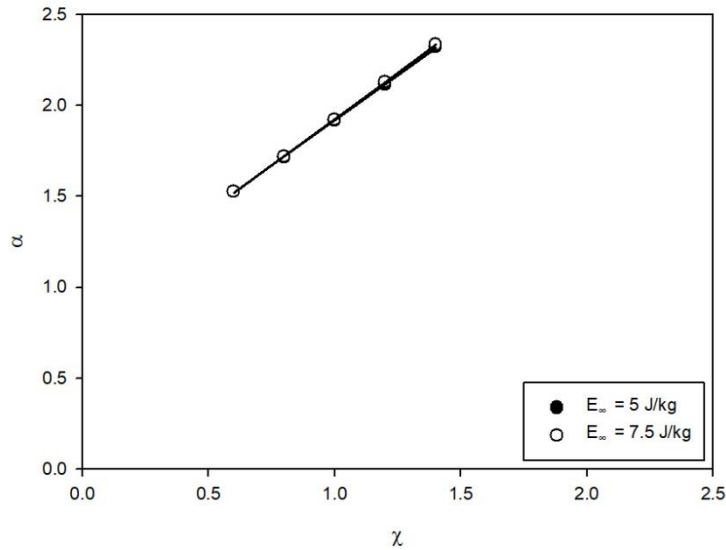

Figure 3.18. Relationship between χ and α.

As shown in Figure 3.18, χ and α have a linear relationship and their slope is 1, which indicates that the relationship in Eq. (3.25) is reflected except for the difference in the energy distribution owing to the particle size. Also, this relationship is maintained regardless of E_∞, and confirms that E_∞ does not affect α.

Additionally, an analysis was performed for the case where xE_0 is not considered, which is adopted in several studies (Carvalho and Tavares, 2013). An xE_0 value of 0 means that collision energy affects particle breakage. Even very small energies directly affect the breakage when the number of collisions is large. However, given that a small amount of energy is generated during the DEM simulation, it should be excluded. In this section, only energies with mass-specific energy greater than 0.1 J/kg were considered.

First, the relationship between E_∞ and breakage rate was confirmed. Figure 3.19 shows the results of the simulation under the conditions applied in Figure 3.15.
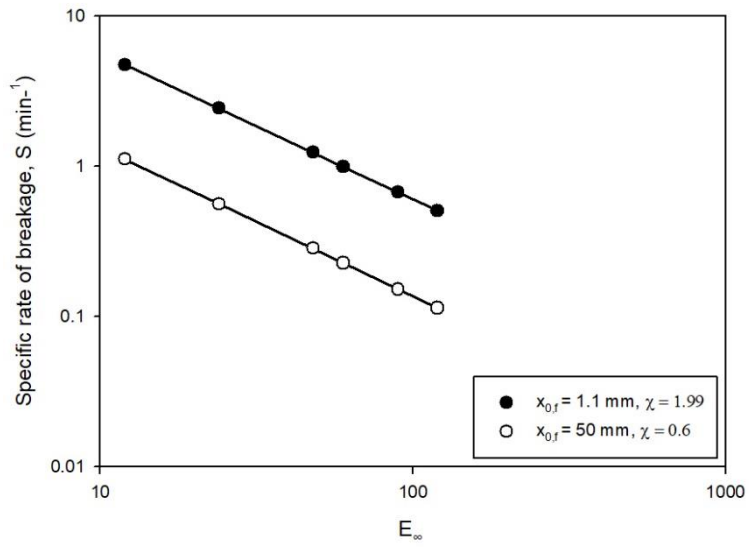
Figure 3.19. Relationship between E_∞ and breakage rate when xE_0 is 0.

Even if the value of E_b changes, the slope is almost constant, and the values are -0.97 and -0.99. Unlike in Figure 3.15, the slope here is close to -1 even when the breakage rate is relatively large. This can be attributed to the fact that the distribution of energy is dense and the probability calculation using the average energy is possible. In fact, as shown in Figure 3.20, when xE_0 is 0, the energy is denser than when xE_0 is 2 Jmm/kg.
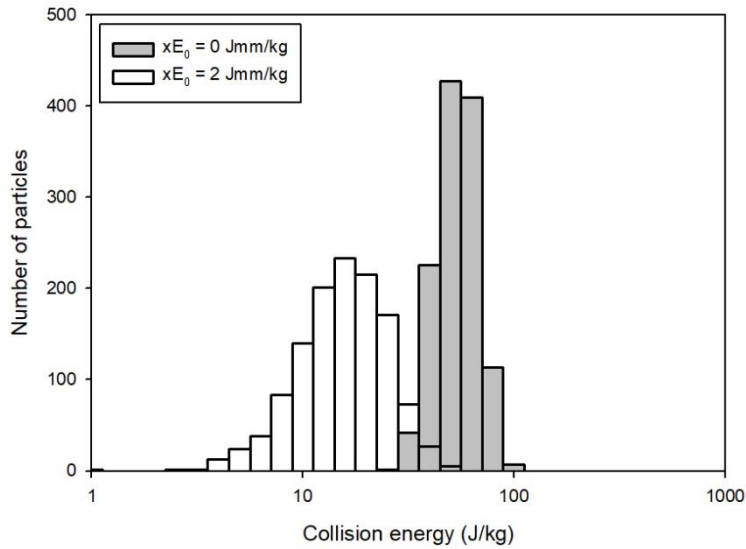

Figure 3.20. Histogram of the average collision energy for different values of xE_0.

Figure 3.21 shows the graph of change of α according to χ under the conditions shown in Figure 3.18. Not only is the graph linear, but the values of α and χ are almost the same. This result is in perfect agreement with Eq. (3.25). Additionally, when xE_0 is 0, the difference between the average collision energy and collision frequency according to the particle is not big. When xE_0 is non-zero, E_∞ has no effect on α.
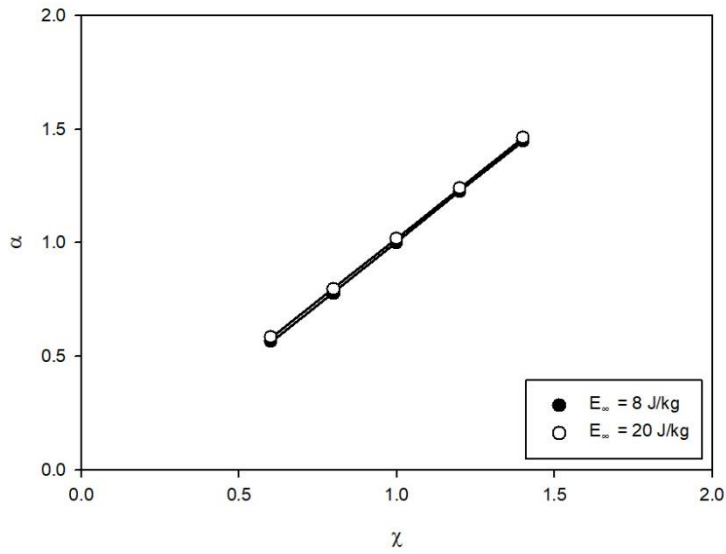

Figure 3.21. Relationship between χ and α when xE_0 is 0.

Results show that the probability parameter and breakage rate exhibit the relationship demonstrated in Eq. (3.20), that is, when the breakage rate is small or the average energy distribution of the particles is dense, it exhibits a more simplified relationship, as demonstrated in Eq. (3.23). Herein, E_∞ is inversely proportional to the breakage rate and does not affect α, which is related to particle size sensitivity of the breakage rate. Additionally, χ and α have a linear relationship with a slope of 1, as demonstrated in Eq. (3.25).

3.4.5. Scale-Up Factor

Operating conditions applied in industries is different from those applied in laboratories. Therefore, a scale-up factor must be considered to apply the experimental results in industrial-scale mill operations. For the grinding kinetics model, an empirical formula based on the scale-up factor is used to predict the changes in the specific rate of breakage when the operating conditions change (Austin et al., 1984). Here, DEM simulations were performed under various operating conditions. Correspondingly, the breakage rate was calculated based on the results and was then compared with the values obtained using the empirical formula. Additionally, when machine-dependents were determined by DEM simulation, results were obtained for various materials by changing the material-dependents.

3.4.5.1. Formal ball and powder filling

First, the formal ball filling J and formal powder filling U were changed, and the motion of the particles inside the mill and collision energy distribution were

compared as shown in Figures 3.22 and 3.23. It was seen that J varied from 0.2–0.6 whereas U varied from 0.5–1.3.
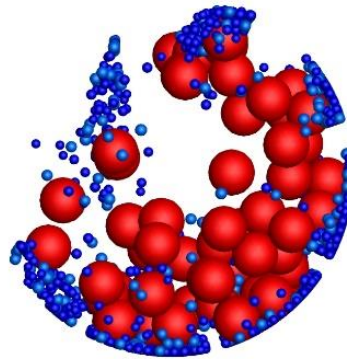
(a)
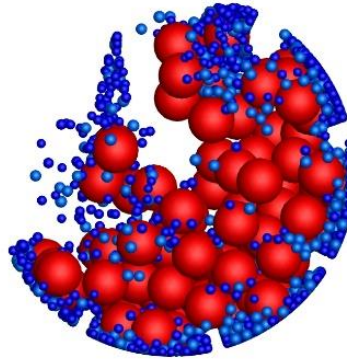
(b)

(c)

Figure 3.22. Simulation snapshots for different formal ball filling (J) when the

formal powder filling (U) was 0.5, (a) J = 0.2, (b) J = 0.3, and (c) J = 0.4.

Figure 3.23. Energy distribution as a function of formal ball filling (J) when the
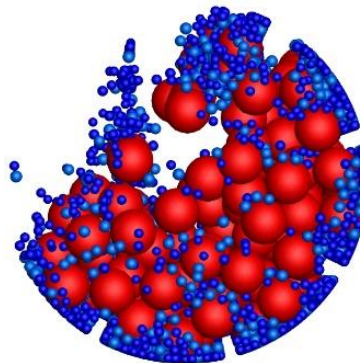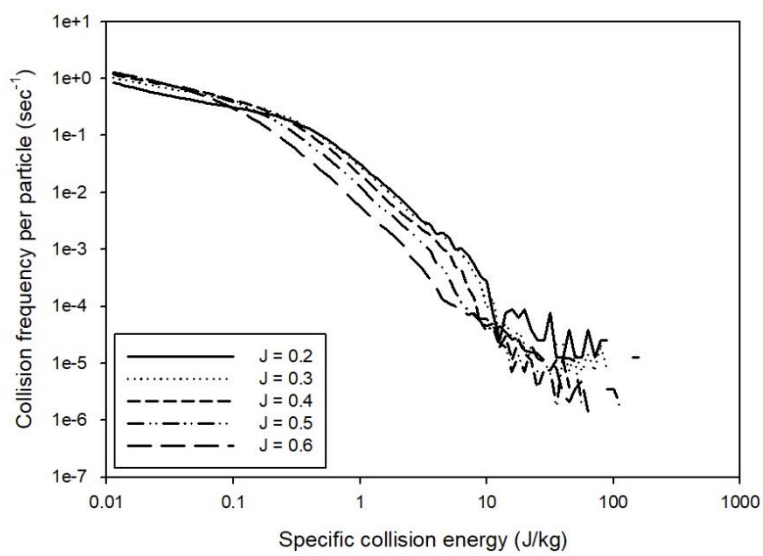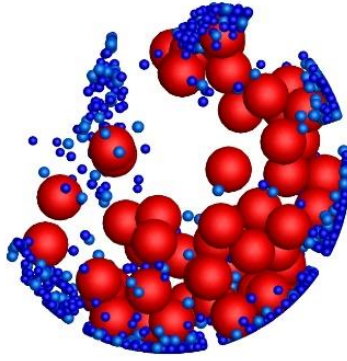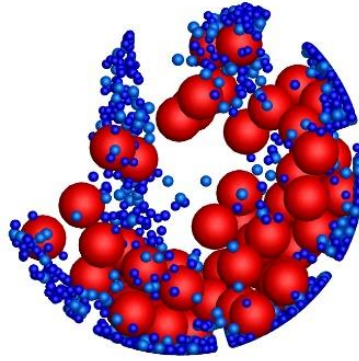
formal powder filling (U) is 0.5.

As shown in Figure 3.22, as the formal ball filling J increased, the behaviors of both the balls and powders changed, resulting in more cascading streams. Additionally, the position of the shoulder, where the balls and powders were ejected after being lifted to a certain height in the mill by a lifter was almost constant; however, the particle bed expanded and the toe where the ejected balls fell on the particles and collided shifted to the left. Therefore, there was difficulty in moving the particles ejected by cataracting stream to a sufficient distance. The change in the energy distribution according to J caused by changes in the movements is shown in Figure 3.23. As the cascading stream increased, the low energy collision increased and the high-energy collision caused by the cataracting stream decreased, considering the fall distance of cataracing stream decreases as J increases.

Figure 3.24 shows the changes in the behaviors of the particles inside the mill according to U. It was observed that U does not significantly affect the movement of particles inside the mill, especially the ball media. Therefore, there is minimal difference in the energy distribution compared to other operational conditions, as shown in Figure 3.25. Furthermore, relatively large energies of approximately 0.3 J/kg or more occur more frequently considering U is smaller. This is because, even if the balls show similar movements, the number of particles differ, and hence, the collision frequency per particle decreases.

(a)

(b)
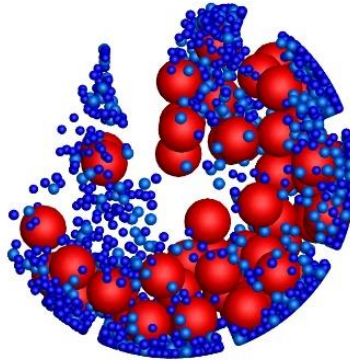
(c)

Figure 3.24. Simulation snapshots for different formal powder filling (U) when the

formal ball filling (J) is 0.2. (a) U = 0.5, (b) U = 0.7, and (c) U = 0.9.

Figure 3.25. Energy distribution as a function of formal powder filling (U) when

the formal ball filling (J) is 0.2.

Formal ball filling J and formal powder filling U affect the specific rate of breakage. Austin et al. (1984) explained the effect in terms of the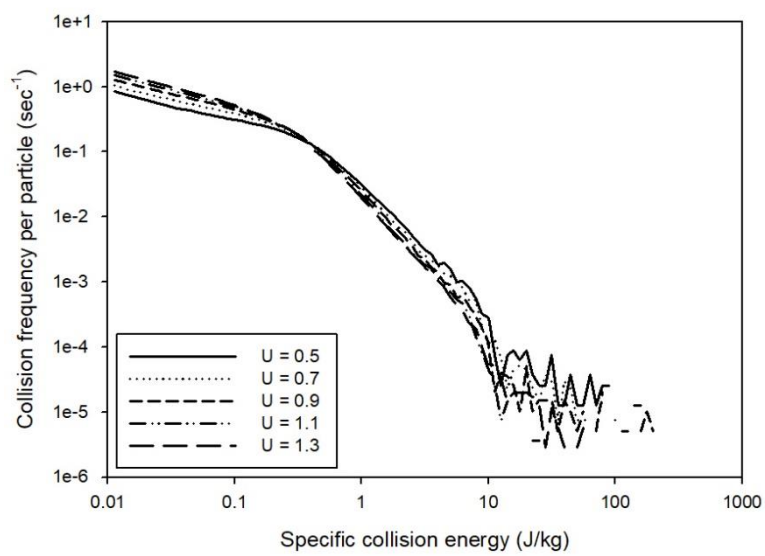 probability of a ball-powder collision that caused breakage. As J and U increase, the probabilities of the ball-ball and powder-powder collisions, which are not effective for breakage, increase. As a result, the specific rate of breakage decreases. Through experiments, these authors proposed regression models to analyze the relationship between the breakage rate and J and U, give as:

$$S \propto \frac{\exp[-cU]}{1+6.6J^{2.3}}, \qquad (3.26)$$

where c is the wet/dry coefficient, which is typically 1.2 and 1.32 for dry and wet grinding, respectively. Figures 3.26 and 3.27 show the change in the specific rate of breakage according to J and U, respectively. To conveniently compare simulations and empirical formulas, the ratio between the breakage rates for different parameters, and a reference value of J = 0.2 and U = 0.5 were used. The breakage probability parameters xE_0 and E_b were set to 2 Jmm/kg and 8.1 J/kg, respectively. Furthermore, the breakage rate was calculated with various xE_0 and E_b values to compare the results for various materials.
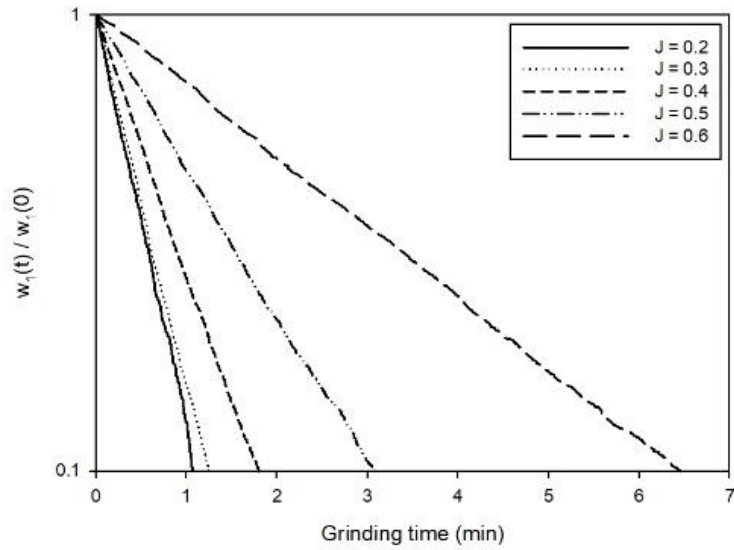
(a)
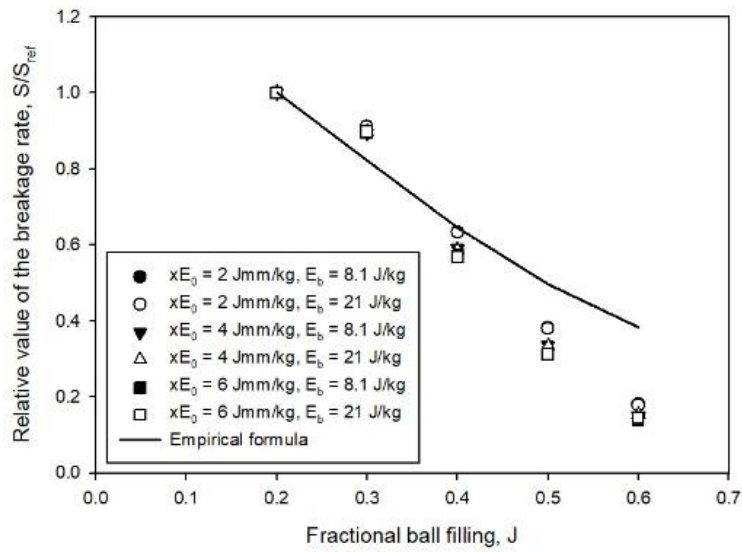
(b)

Figure 3.26. Changes in the specific rate of breakage according to the formal ball

filling (J): (a) First-order plot and (b) Relative breakage rate values.
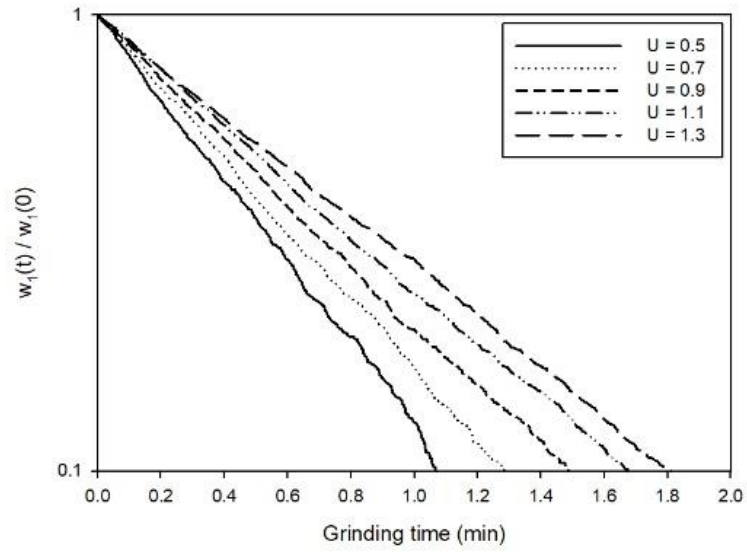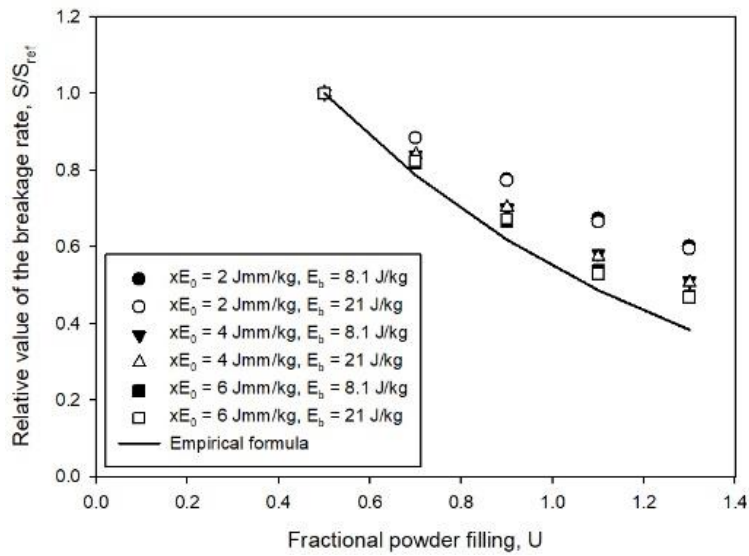
(a)

(b)

Figure 3.27. Change in the specific rate of breakage according to the formal

powder filling (U). (a) First-order plot and (b) Relative breakage rate values.

The simulation and empirical results showed a similar tendency or a reasonable agreement according to the material properties in Figures 3.26(b) and 3.26(b). In the energy distribution of Figures 3.23 and 3.25, it was observed that the energy greater than E_0 occurred more frequently as J and U decreased, thereby resulting in an increase in the breakage rate. In both operational conditions, E_b does not affect the change in the breakage rate. As discussed in Section 3.4.4, the breakage rate is inversely proportional to E_b. Next, each operating condition was analyzed in detail.

When J is 0.3 or more, the decrease in the breakage rate appears faster than the empirical formula. In the empirical formula, the relationship with the breakage rate was derived by considering the effective number of collisions; however, in the simulation, an additional factor decreased the breakage according to the changes in the ball movement. If these effects are excluded by changing other operating conditions, results consistent with the empirical formula could be achieved. In Section 3.4.6, the effect of changing the lifter size was analyzed. Additionally, when J was changed, the simulated results appeared almost the same regardless of the material-dependents. This is because the energy distribution of approximately 0.3 J/kg or more in the energy distribution in Figure 3.23 was almost parallel. Although a difference was observed in the maximum energy region, it was difficult to directly affect the breakage rate considering the frequency was very low.

In case of U, only when xE_0 was 2 Jmm/kg, it differed from other material properties owing to the energy distribution. As shown in Figure 3.25, the energy distribution in high energy regions was almost parallel, but the graphs intersected around 0.3 J/kg. When xE_0 was 2 Jmm/kg, given that the threshold energy was

about 0.3 J/kg, it was interpreted that the energy distribution was affected and the difference in the breakage rate according to U decreased significantly.

3.4.5.2. Diameter of the mill and ball media

The diameters of the mill and ball media are essential in the scale-up of a grinding mill. In particular, for the mill diameter, the size of the mill used in the industry is much larger than that used in the laboratory for high-capacity operation. Accordingly, the sizes of the ball media varies. Simulations were performed for various diameter conditions; however, the lifter size remained constant even if the mill and ball diameter changed. The simulation snapshot and energy distribution according to change in mill diameter are shown in Figures 3.28 and 3.29, respectively. The mill diameter D varied from 0.2–0.5 m.
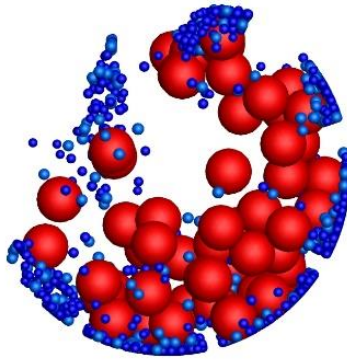
(a)
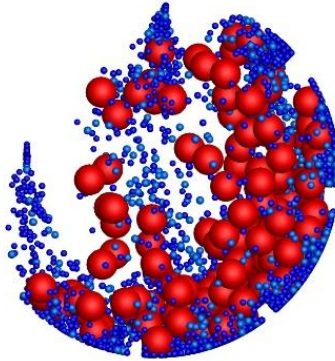
(b)
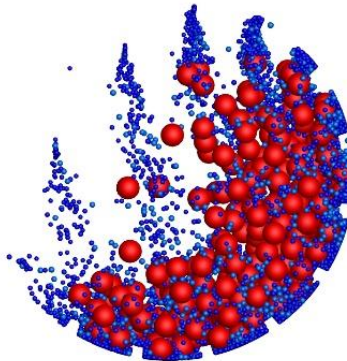
(c)

Figure 3.28. Simulation snapshots for various mill diameters (D) when the ball

diameter (d) was 25.4 mm. (a) D = 0.2 m, (b) D = 0.3 m, and (c) D = 0.4 m.
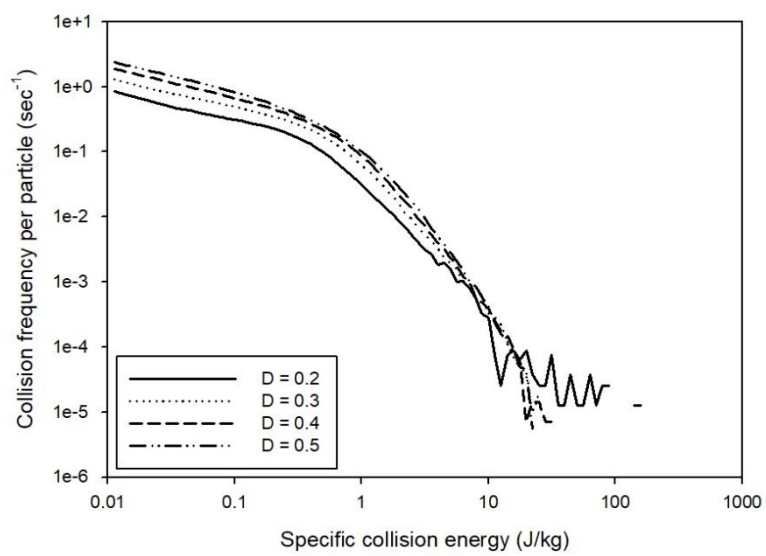
Figure 3.29. Energy distribution as a function of the mill diameter (D) when the

ball diameter (d) is 25.4 mm.

As shown in Figure 3.28, although the fractional volume filling remained constant, the behavior of the particles differed. As the mill diameter increased, the shoulder position gradually lowered, resulting in weak cataracting. In addition, as the cascading bulk of the charge increased, its depth also increased. The location of the toe varied slightly as a function of the mill diameter. The collision energy distribution according to the mill diameter is shown in Figure 3.29. It can be seen that the number of collisions increased as the mill diameter increased for all collision energy regions, despite the weakening of the cataracting stream. For high collision energy regions, the actual travel distance increased owing to the increase of the mill diameter. Furthermore, as the surface area of the cascading bulk of the charge increased, traveling a sufficient distance at once when the particles cascaded down became feasible, thereby resulting in an increased collision energy.

The simulation snapshot and energy distribution according to change in ball diameter are shown in Figures 3.30 and 3.31. The ball diameter d varied from 19.05–44.45 mm. Figure 3.30 shows the changes in the behavior of the flow when the ball diameter varied. The visually dominant part of the change was the position of the shoulder, which was affected by the lifter. The lifter size remained constant when the ball diameter changed, indicating that the lifter size became relatively small, which in turn prevents the ball from being effectively transported to the top of the mill, resulting in a weak cataracting stream. In addition, the number of balls decreased as the ball diameter increased, which affected both the collision energy and the number of collisions between balls and powders, and resulted in the change in the energy distribution, as shown in Figure 3.31. As the ball diameter increased, the number of collisions decreased in almost all energy regions. Only collisions close to the

maximum energy occurred more frequently considering the collision energy per mass increased as the ball size increased.
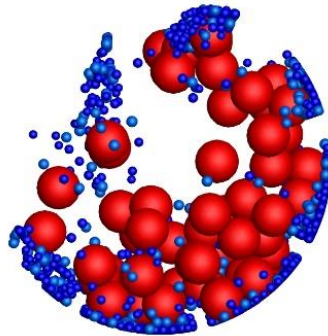
(a)
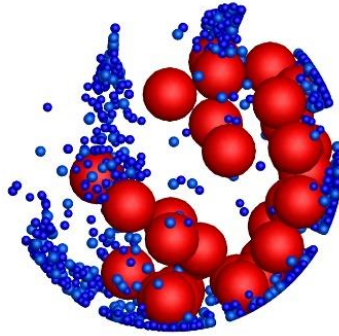
(b)
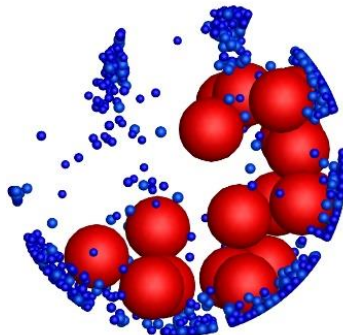
(c)

Figure 3.30. Simulation snapshots for various ball diameter (d) when the mill diameter (D) was 0.2 mm. (a) d = 25.4 mm, (b) d = 31.75 mm, and (c) d = 38.1 mm.
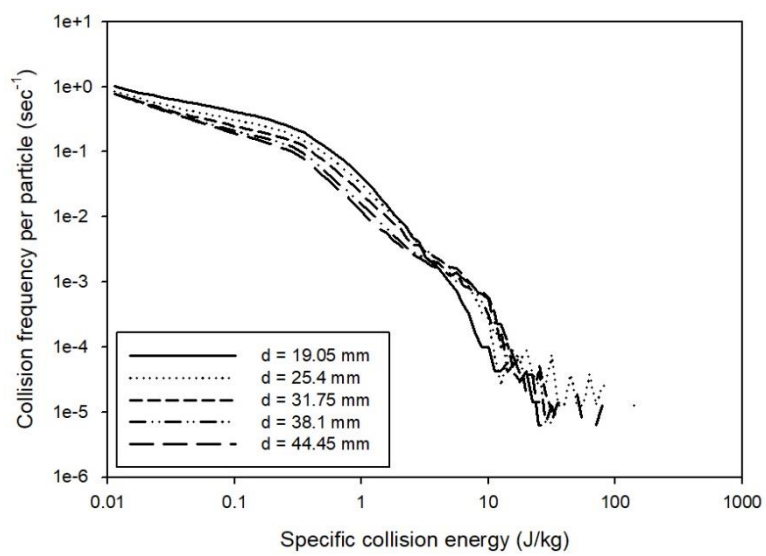
Figure 3.31. Energy distribution as a function of d when the mill diameter (D) is

0.2 m.

The probability of collision between the balls and powder increased in proportion to the mill diameter; however, the critical mill rotational speed decreased inversely proportional to the square root of the mill diameter. As a result, the specific rate of breakage was proportional to the square root of the mill diameter. For the diameter of the ball media, as the ball size decreased, the number of ball media increased, and the number of collisions with the particles increased. Therefore, an inverse relationship was observed with the specific rate of breakage. The empirical formula for the change in the specific rate of breakage according to the mill diameter and the diameter of the ball media in the grinding kinetics model is given as (Austin et al., 1984):

$$S \propto \frac{\sqrt{D}}{d},\tag{3.27}$$

Figures 3.32 and 3.33 shows the changes in the specific rate of breakage according to D and d, respectively. The ratio between breakage rates for different parameters and a reference value of D = 0.2 m and d = 19.05 mm was used. The breakage probability parameter xE_0 and E_b were set to 2 Jmm/kg and 8.1 J/kg, respectively. Furthermore, to compare the results for various materials, the breakage rate was calculated for different values of xE_0 and E_b.
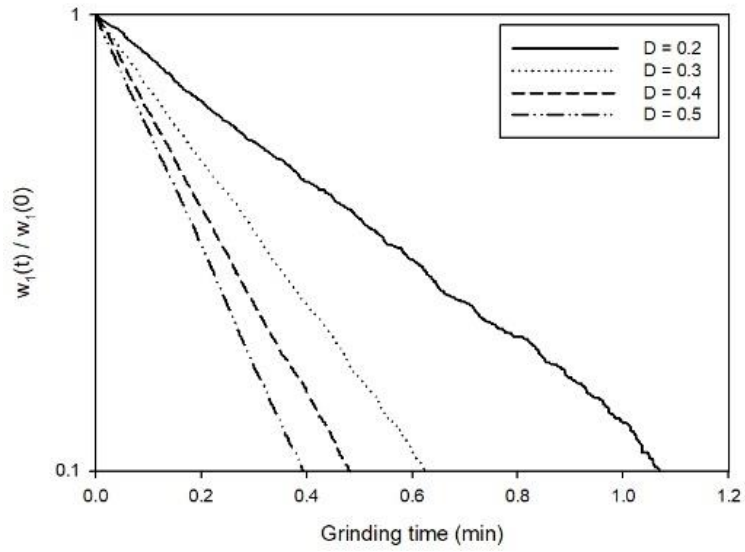
(a)
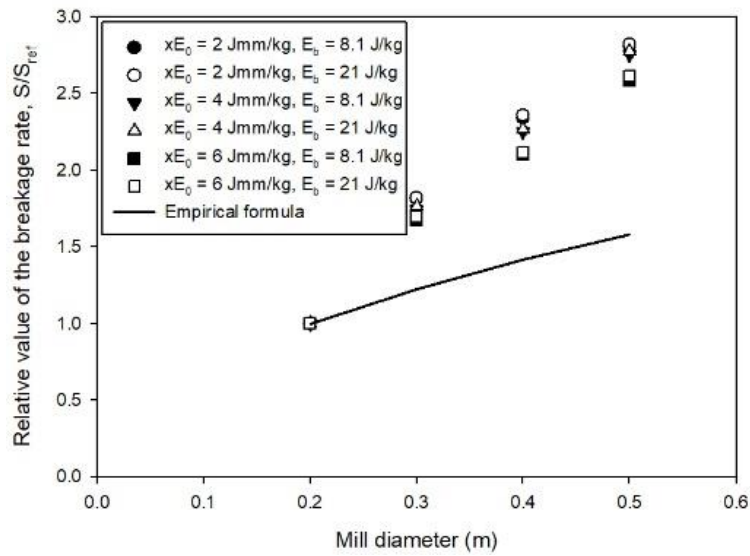
(b)

Figure 3.32. Changes in the specific rate of breakage according to the mill diameter

(D). (a) First-order plot and (b) Relative breakage rate values.
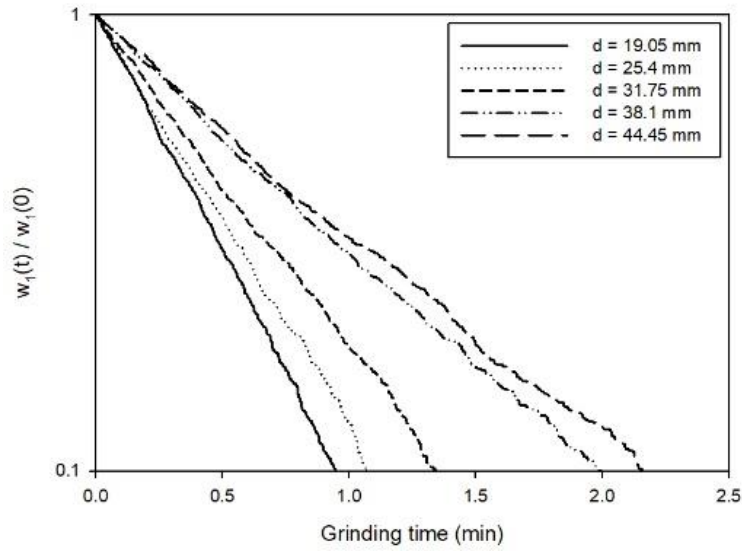
(a)
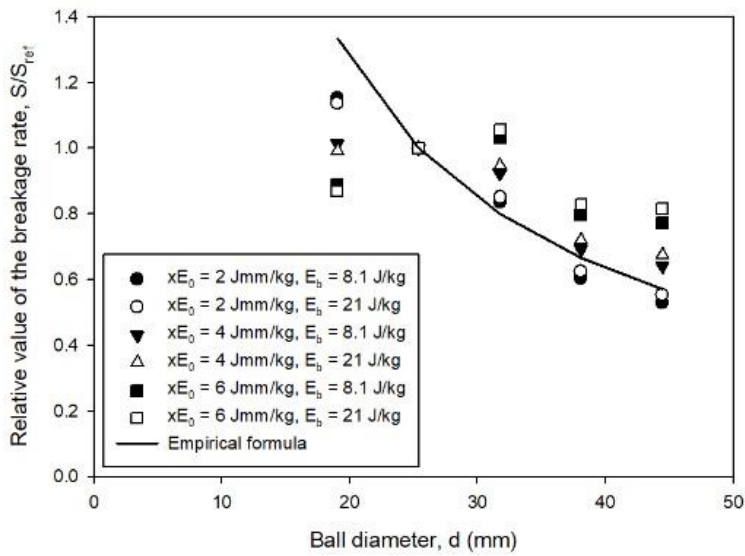
(b)

Figure 3.33. Changes in the specific rate of breakage according to the ball diameter

(d). (a) First-order plot and (b) Relative breakage rate values.

As shown in Figure 3.32, the change in the breakage rate according to the mill diameter was significantly different from that of the empirical formula, as a result of the difference in the simulation snapshot shown in Figure 3.28. In the empirical formula, the relationship between the mill diameter and the breakage rate was explained based on the collision probability and the changes in the mill rotational speed. Although the changes in rotational speed in the simulation exhibited the same effect, the collision probability did not. In the simulation, as the cataracting stream occurred actively, the effect of increasing the collision energy became greater than the increase in the number of collisions. Unlike the number of collisions, the collision energy was not proportional to breakage rate considering it exhibited an exponential relationship with the breakage probability. This made the simulation results different from that of the empirical formula, and it is predicted that this gap will be reduced if the cataracting stream is weakened by changing the operational conditions.

The effect of changes in the diameter of the ball media on the breakage rate showed a different tendency from the previous operating conditions. As shown in Figure 3.33(b), the simulation results of the reference condition, represented by the filled circle dots, were in good agreement with the empirical formula. Additionally, compared to the previous results, E_b does not affect the change in the breakage rate. However, big differences were observed in the results depending on xE_0, considering the graphs in the energy distribution in Figure 3.31 were not parallel but intersected each other. At energies greater than 0.3 J/kg, which is the threshold energy when xE_0 is 2 Jmm/kg, the energy distribution of particle whose size is 19.05 mm intersected with the energy distribution of the reference size and

positioned below, indicating that as xE_0 increased, the decreasing ratio of effective energy for particle breakage was relatively large. Therefore, the breakage rate decreased faster than the reference size. The case where the relative breakage rate becomes large is also explained in a similar manner. In conclusion, this difference can be attributed to the changes in the collision frequency occurring due to the difference in the size of the ball media.

3.4.5.3. Mill rotational speed

Figures 3.34 and 3.35 show the simulation snapshot and energy distribution according to the change in the rotational speed, respectively. The mill rotational speed was determined by the fraction of the critical speed, which varied from 0.5 to 0.9. As shown in Figure 3.34, as the rotational speed increased, both the balls and the powders traveled up the wall to a higher position, resulting in a cataracting stream and an increase in position of the shoulder. Additionally, the toe moved to the left as the ball was ejected from the lifter surface at a higher angle. In particular, when the fraction was 0.5, cataracting hardly occurred, and only cascading occurred. Conversely, when the fraction was 0.8, the centrifugal force became too large, and the ball and powder rotated along the wall past the top of the circle. Because this is caused by lifters, not all balls were carried, and some balls fall along the way.
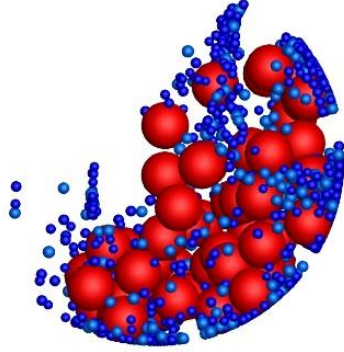
(a)
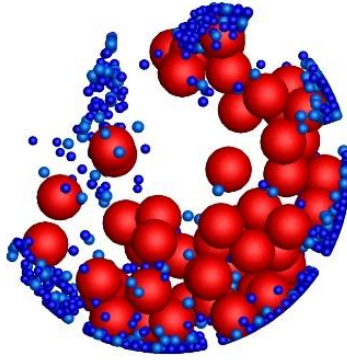
(b)
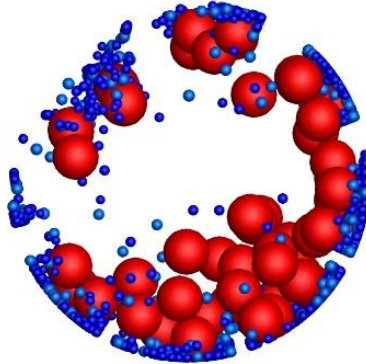
(c)

Figure 3.34. Simulation snapshot according to the changes in the rotational speed.

(a) $0.5\varphi_c$, (b) $0.7\varphi_c$, and (c) $0.8\varphi_c$.
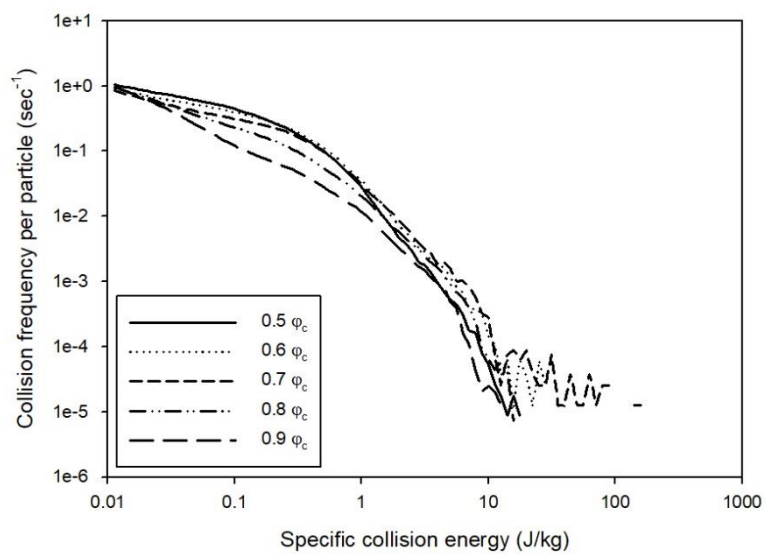
Figure 3.35. Energy distribution according to the changes in the rotational speed.

As shown in Figure 3.35, the changes in energy distribution according to the mill rotational speed is more complex compared to other operating conditions. First, energy with a magnitude between 0.1 and 1 J/kg was different when the ratio to critical speed was greater than or equal to 0.8 and less than 0.8, respectively. When 0.8 or more, the collision frequency was relatively small considering the number of effective collisions decreases as the ball rotates attached to the wall, as shown in Figure 3.34(c). Furthermore, when the energy is 1 J/kg or more, the frequency in the case of the fraction of 0.5 decreases sharply, and the frequency in the case of the fraction of 0.8 is reversed. As shown in Figure 3.34(a), when the fraction is 0.5, cataracting stream does not occur significantly, and hence, it is rare that a collision energy of 1 J/kg or more could occur. The maximum collision energy generated by each mill rotational speed was the greatest when the fraction was 0.7, followed by 0.6 and 0.5.

The relationship between the breakage rate and mill rotational speed suggested by Austin (1984) is related to the net power required to rotate the mill. The maximum in net power is usually found in range from 0.7 to 0.85 of the critical speed, considering the range where the maximum value occurs is different depending on the diameter of the mill and the type of lifter. The empirical relationship between the breakage rate and mill rotational speed proposed by Austin (1984) is given as:

$$S \propto (\varphi_r - 0.1) \left(\frac{1}{1+\exp\{15.7(\varphi_r - 0.94)\}} \right), \tag{3.28}$$

where ϕ_r is the fraction of the rotational speed to the critical rotational speed. Figure 3.36 shows the changes in the specific rate of breakage according to

the mill rotational speed expressed as the fraction of the critical speed. As a reference value, the breakage rate when the fraction was 0.7 was used. The breakage probability parameter xE_0 and E_b were set to 2 Jmm/kg and 8.1 J/kg, respectively. Additionally, the breakage rate was calculated for different values of xE_0 and E_b to compare the results for various materials.
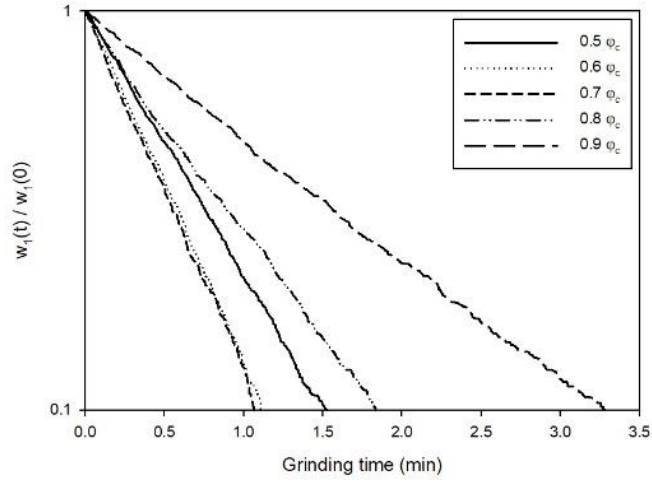
(a)
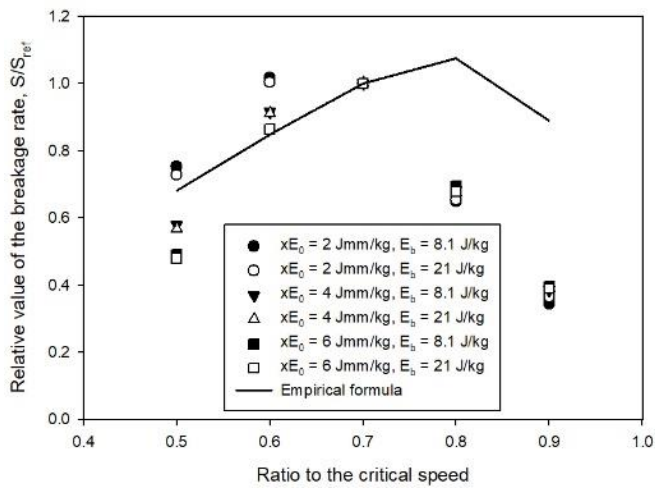
(b)

Figure 3.36. Change in the specific rate of breakage according to the mill rotational

speed. (a) First-order plot and (b) Relative breakage rate values.

As shown in Figure 3.36, the change of breakage rate according to the mill rotational speed differed from that of the empirical formula. In the empirical formula, the maximum value of the breakage rate appeared when the fraction of the critical speed was about 0.8. However, in the simulation results, it appeared when it was about 0.7, and the breakage rate decreased when it was 0.8. This could be due to the mill conditions in the simulation, especially the size of the lifter. As shown in Figure 3.34(c), as the balls rotated along the wall surface, the breakage was inevitably inefficient. In the energy distribution shown in Figure 3.35, the order of the mill rotational speed with the largest maximum collision energy was the same as the order of the breakage rate. Considering the energy distribution graph according to mill rotational speed in Figure 3.35 also intersected, the change in the breakage rate varied significantly with xE_0. When the rotational speed fraction was larger than the reference value, the changes in the breakage rate was similar considering the graphs are parallel. However, when the rotational speed is smaller than the reference value, the ratio of the breakage rate decreases considering the graphs intersect and locate below.

3.4.6. Effect of the Lifter Size

The specific rate of breakage changes not only according to the operating conditions of the mill, but also according to the lifter size. In particular, as shown in Figure 3.34, the lifter significantly influences the movement of the ball according to the mill rotational speed. The critical rotational speed, which is the standard of the mill rotational speed, is the speed at which the ball rotates attached to the wall without falling considering gravity and centrifugal force acting on the ball are balanced. The

lifter moves the ball to the top of the mill more easily, and hence, depending on the lifter, the balls centrifuge on the mill and do not tumble even below the critical speed. In this study, a trapezoidal lifter, as shown in Figure 3.1, was used. To analyze the effect of the lifter size on the breakage rate, simulation was performed for lifter height of 8 and 16 mm. The probability parameters and operating conditions were same as in Section 3.4.5. The change in the breakage rate according to operating conditions was compared with Section 3.4.5. After calculating the breakage rate using the empirical formula, one point of the results matched to the breakage rate determined from the simulation results with a ball mill with an 8 mm lifter. Then, the empirical formula and simulation results were compared.

3.4.6.1. Formal ball and powder filling

Figure 3.37 shows the simulation snapshot according to the formal ball filling when the size of the lifter changes. In particular, it shows the cases where J is 0.2 and 0.3 with a noticeable difference.

(a)   (b)   (c)

(d)   (e)   (f)
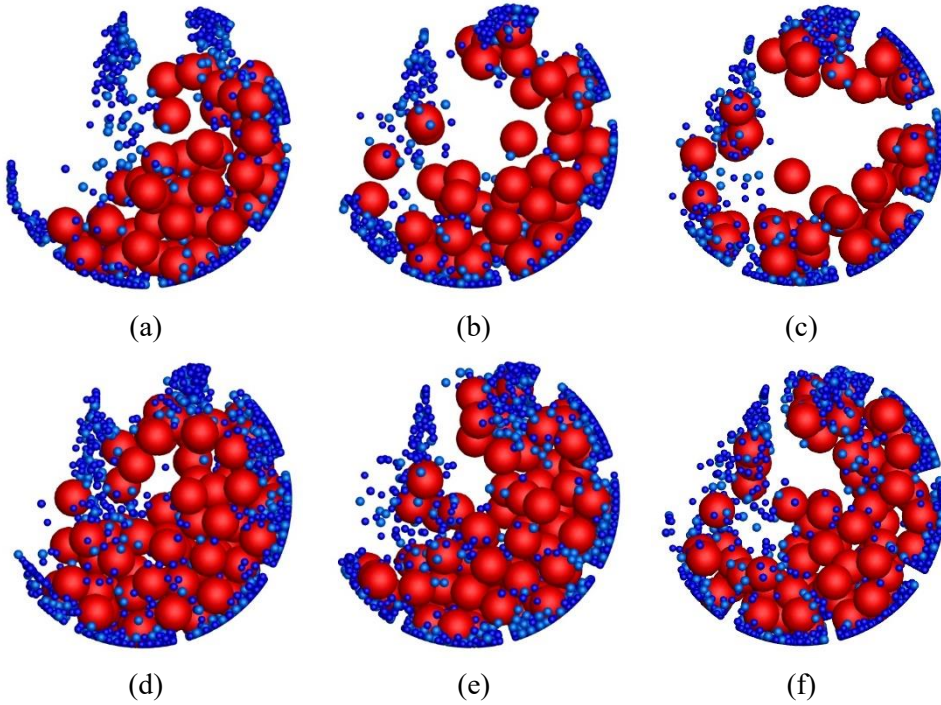
Figure 3.37. Comparison of the simulation snapshots when the lifter size and formal ball filling (J) vary. (a) J = 0.2 and 8 mm lifter, (b) J = 0.2 and 12 mm lifter, (c) J = 0.2 and 16 mm lifter, (d) J = 0.3 and 8 mm lifter, (e) J = 0.3 and 12 mm lifter, and (f) J = 0.3 and 16 mm lifter.

When the lifter size is 8 mm and J is 0.2 mm, a cascading stream is predominantly generated, whereas a cataracting stream occurs occasionally. However, unlike when the lifter size is larger, the ball media often fall on the particle bed without reaching the toe (Figure 3.37(a)). For larger lifter sizes, the cataracting stream dominates. As shown in Figure 3.37(c), although the ball does not centrifuge on the mill, the energy received by the particle is relatively small considering the ball is ejected from near the top of the mill. When J is larger than 0.3, the distance between the shoulder and toe decreases regardless of the lifter size, even when a cataracting stream occurs as the particle beds expand like the size of the lifter is large. This results in collisions that are inefficient for particle breakage. The energy distribution for 8 and 16 mm lifters are shown in Figure 3.38.

(a)

(b)
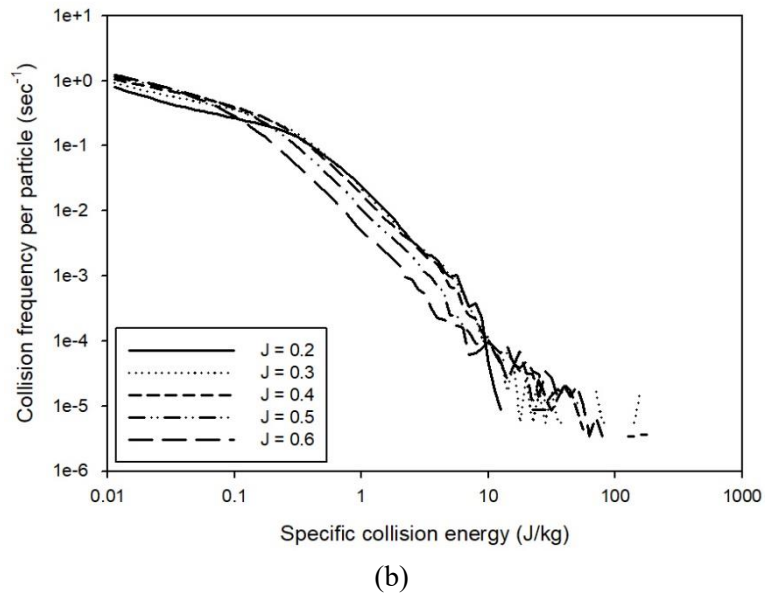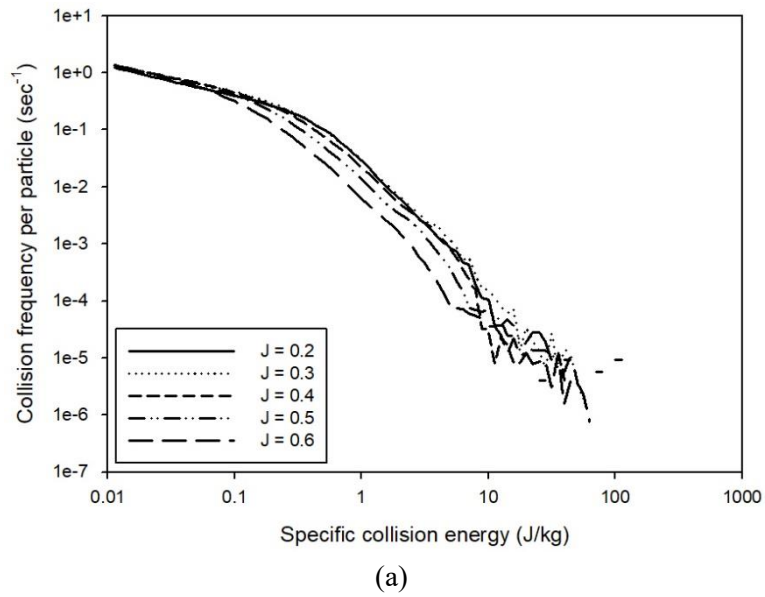
Figure 3.38. Change in the energy distribution according to the formal ball filling

(J). (a) 8 mm lifter and (b) 16 mm lifter.

The energy distribution changes according to the difference in the ball movement. When J is 0.3 for small lifter sizes, it shows a higher collision frequency in the whole energy section compared to when J is 0.2 owing to the weakened cataracting stream (Figure 3.38(a)). Except for this phenomenon, the energy distributions in Figure 3.38 showed a similar trend. However, on comparing the energy distribution in the case of simulation with an energy distribution of 12 mm lifter in Figure 3.23, it was found that the collision frequency slightly increased for small lifter sizes in the change of the collision energy distribution according to J. This is because particle beds are formed gently owing to the decreased in the lifter size, which allowed the cataracting stream to travel more easily. Conversely, when the lifter size was large, the distance traveled by the cataracting stream decreased considering the lifter carries the ball closer to the top of the mill, and hence, the energy of collision becomes relatively low.

Figure 3.39 shows the changes in the ratio of breakage rate according to the formal ball filling using the breakage rate when the J is 0.2 as a reference value. Here, the empirical formula and results of 3.4.5.1 when xE_0 is set to 2 Jmm/kg are denoted as straight lines.
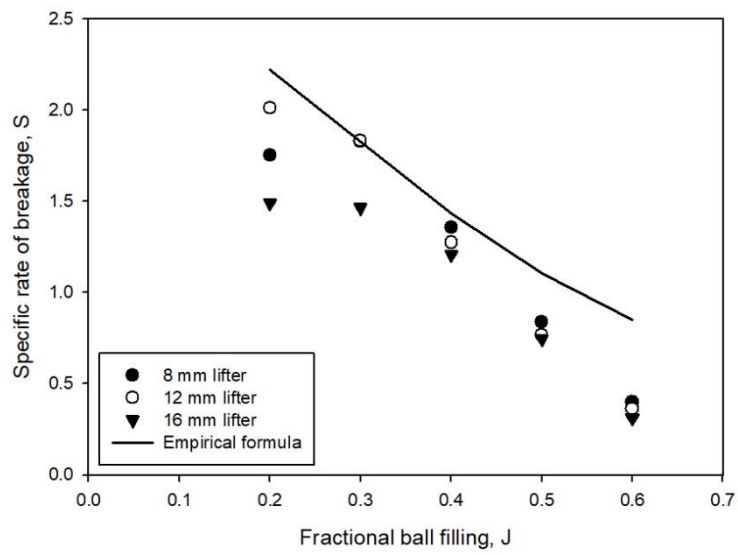
Figure 3.39. Changes in the specific rate of breakage according to the formal ball

filling (J) for different lifter sizes.

The change in the breakage rate is similar to that shown in Figure 3.26, except that the breakage rate is relatively large when J is 0.3. Although the size of the lifter had changed, the decrease in the breakage rate owing to the increase of J is faster than the decrease in the breakage rate explained by the empirical formula. This can be attributed to the fact that only the decrease in the effective number of collisions is considered as the cause of the decrease in the breakage rate in the empirical formula. However, as a result of the performing simulation, it can be confirmed that there is another factor. In the ball movement in Figure 3.37, as J increases, the occurrence of a blockage of the cataracting stream as the particle beds expand affects the breakage rate.

Next, the effect of lifter size on the relationship between formal powder filling and breakage rate was analyzed. Because the difference according to U is not significantly affected by the size of the lifter, a simulation snapshot is shown in Figure 3.40 only when U is 0.9.
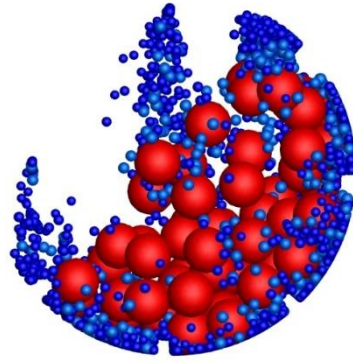
(a)
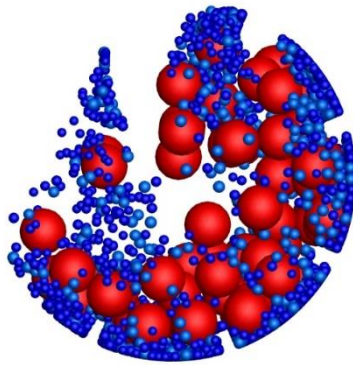
(b)
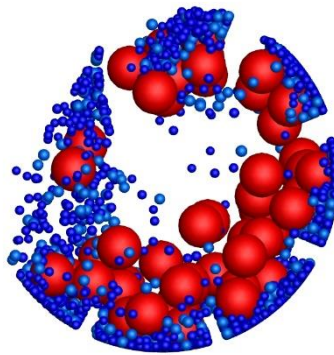
(c)

Figure 3.40. Comparison of the simulation snapshots when the lifter size and

formal powder filling (U) vary. (a) U = 0.9 and 8 mm lifter, (b) U = 0.9 and 12 mm

lifter, and (c) U = 0.9 and 16 mm lifter.

As the size of the lifter decreased, the cascading stream became more active, as shown in Figure 3.40. However, even if the size of the lifter changes, the movement of the ball remains almost the same regardless of the U, as in Figure 3.24. However, the energy distribution according to U becomes denser as the size of the lifter increases, as shown in Figure 3.41. The larger the lifter size is, the more dominantly the cataracting stream occurs. Herein, the collision frequency between the ball and powder is relatively low depending on the location where the ball falls. Generally, when U increases, the number of effective collisions decreases owing to the increase of the powder. However, when the lifter size is large, the number of collisions increases considering the powder in the mill increases, and hence, the change in the number of collisions is offset. Therefore, the larger the lifter size is, the smaller is the change in the energy distribution as U increases, resulting in a denser energy distribution. Finally, when the lifter size decreases, the change in the breakage rate according to U becomes closer to the empirical formula, as shown in Figure 3.42, considering the smaller the lifter size is, the lower is the number of collisions, given that U dominantly affects the breakage rate. The difference according to material properties is similar to Section 3.4.5.1 for small lifter sizes. However, for large lifter sizes, the material properties do not affect the change in the breakage rate considering the energy distribution according to U is almost identical as that shown in Figure 3.41(b).

(a)

(b)

Figure 3.41. Change of the energy distribution according to the formal powder

filling (U). (a) 8 mm lifter and (b) 16 mm lifter.
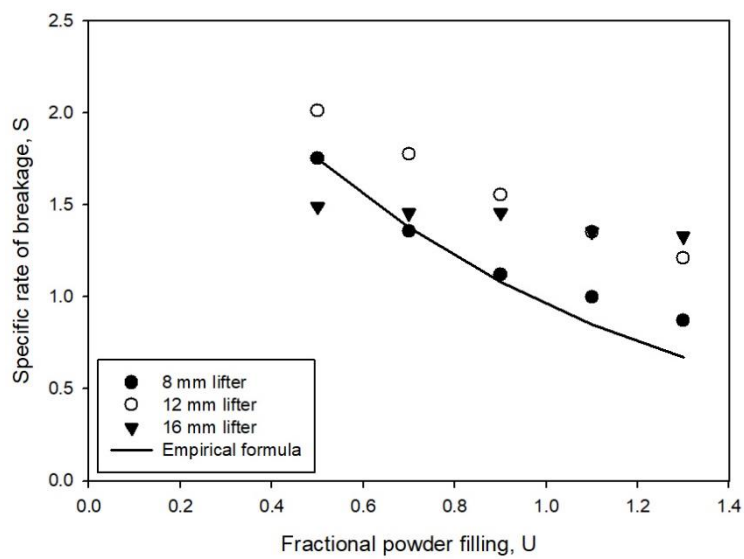
Figure 3.42. Changes in the specific rate of breakage according to the formal

powder filling (U) for different lifter sizes.

3.4.6.2. Diameter of the mill and ball media

Figure 3.43 shows the difference in the ball behavior according to the lifter size when the mill diameter is 0.3 m. The cataracting stream weakened as the lifter size decreased. However, changes the ball behavior towing to an increase in mill diameter was the same as that in Figure 3.28. As a result, the energy distribution appeared similar to that in Figure 3.29, and as shown in Figure 3.44, and the difference in energy distribution according to the change in the mill diameter decreased as the lifter size decreased. This is because the larger the lifter size is, the easier it is to cause a high collision energy by cataracting stream to travel a sufficient distance as the mill diameter increased.

Figure 3.45 shows a comparison of the breakage rate, which clearly shows the effect of reducing lifters. Considering the cataracting stream weakens as the lifter size decreases, the difference in the number of collisions is more pronounced compared to the difference in the collision energy as the mill diameter changes, as mentioned in Section 3.4.5.2. Additionally, as shown in Figure 3.44, when the lifter size decreases, the difference in energy distribution according to mill diameter decreased. As a result, the change in the breakage rate according to the mill diameter becomes closer to the empirical formula, as shown in Figure 3.45.
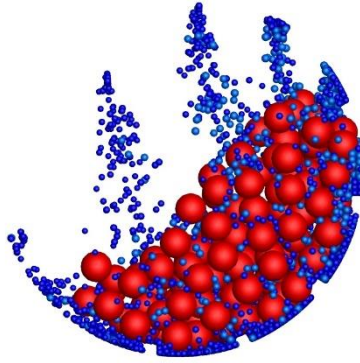
(a)

(b)
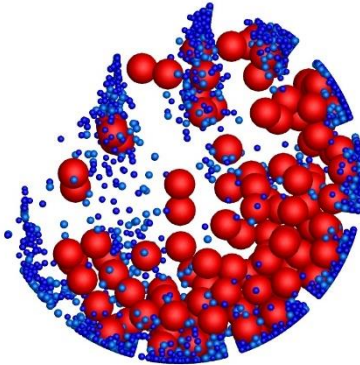
(c)

Figure 3.43. Comparison of the simulation snapshots when the lifter size and mill

diameter (D) vary. (a) D = 0.3 m and 8 mm lifter, (b) D = 0.3 m and 12 mm lifter,
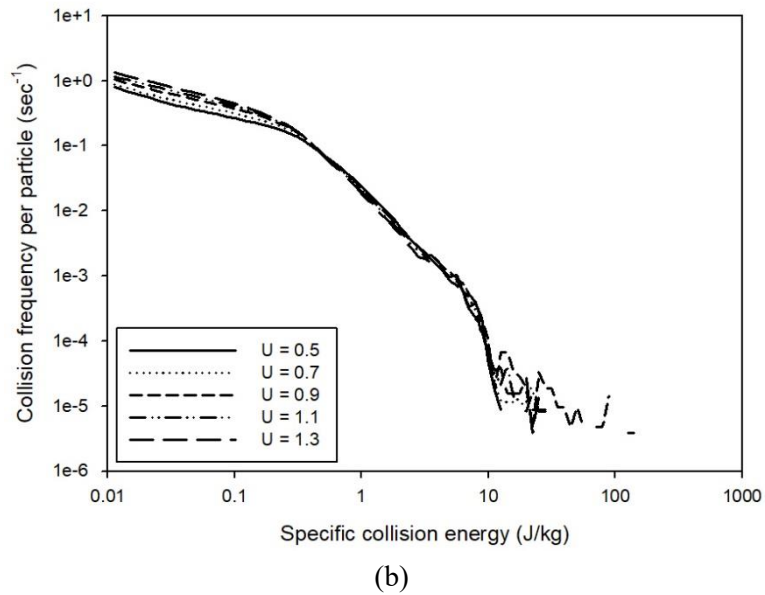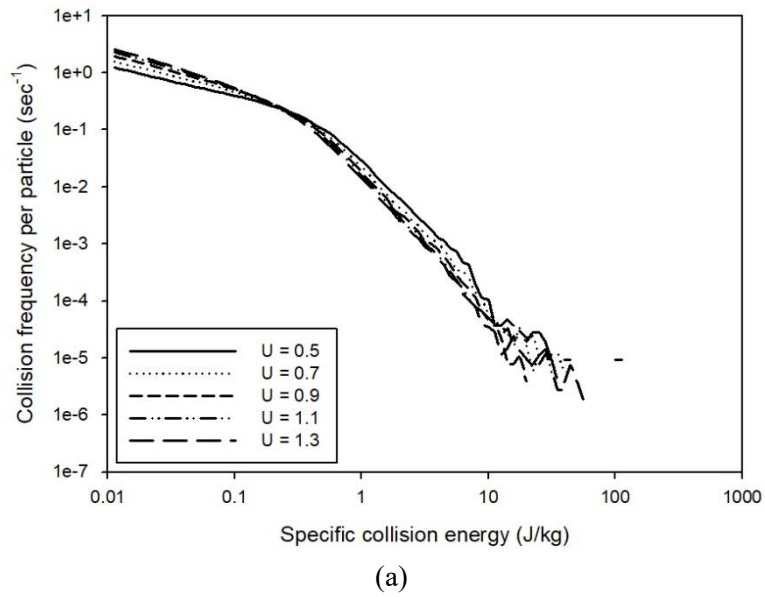
and (c) D = 0.3 m and 16 mm lifter.

(a)

(b)

Figure 3.44. Changes in the energy distribution according to the mill diameter (D).

(a) 8 mm lifter and (b) 16 mm lifter.
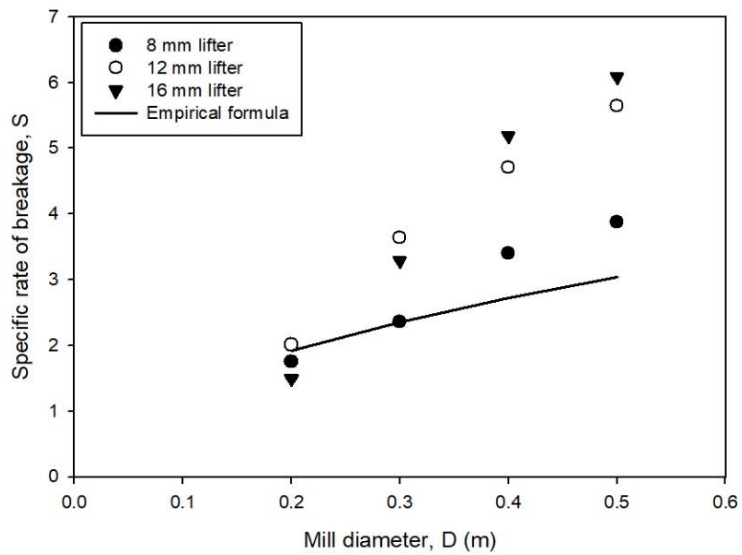
Figure 3.45. Changes in the specific rate of breakage according to the mill diameter
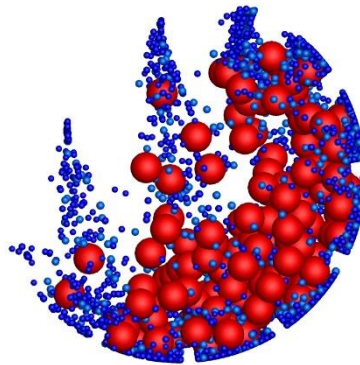
(D) for different lifter sizes.

Changes in the ball diameter when the lifter size is the same causes variations in the relative size of the lifter, indicating that the ability of the lifter to carry the ball to the top of the mill has changed. To analyze the change in ball movement caused by the decrease in the lifter size, ball diameters of 19.05, 31.75, and 44.45 mm were analyzed, are shown in Figure 3.46.

In Figure 3.46, the difference in the relative size of the lifter is the greatest when the ball dimeter is 19.05 mm, so the difference in the movement of the ball is also the greatest. The smaller the lifter size, the relatively weaker the cataracting stream. If the diameter of the ball is larger than 19.05 mm, in case of the 8 mm lifter, the movement of the ball changes with a similar tendency with 12 mm lifter. However, there is a difference in ball movement for 16 mm lifter. Even with the reference size of 25.4 mm, the ball does not fall from a height that can cause an effective collision to breakage, but travels higher along the wall and then falls. Therefore, when the ball becomes large, the size of the lifter becomes relatively small, so that a fall from an optimal height can occur. This can offset the effect that the number of balls decreases as the balls become larger. It means that the number of collisions is reduced, thereby reducing the breakage rate. Figure 3.47 shows the energy distribution change according to the change of the ball diameter.
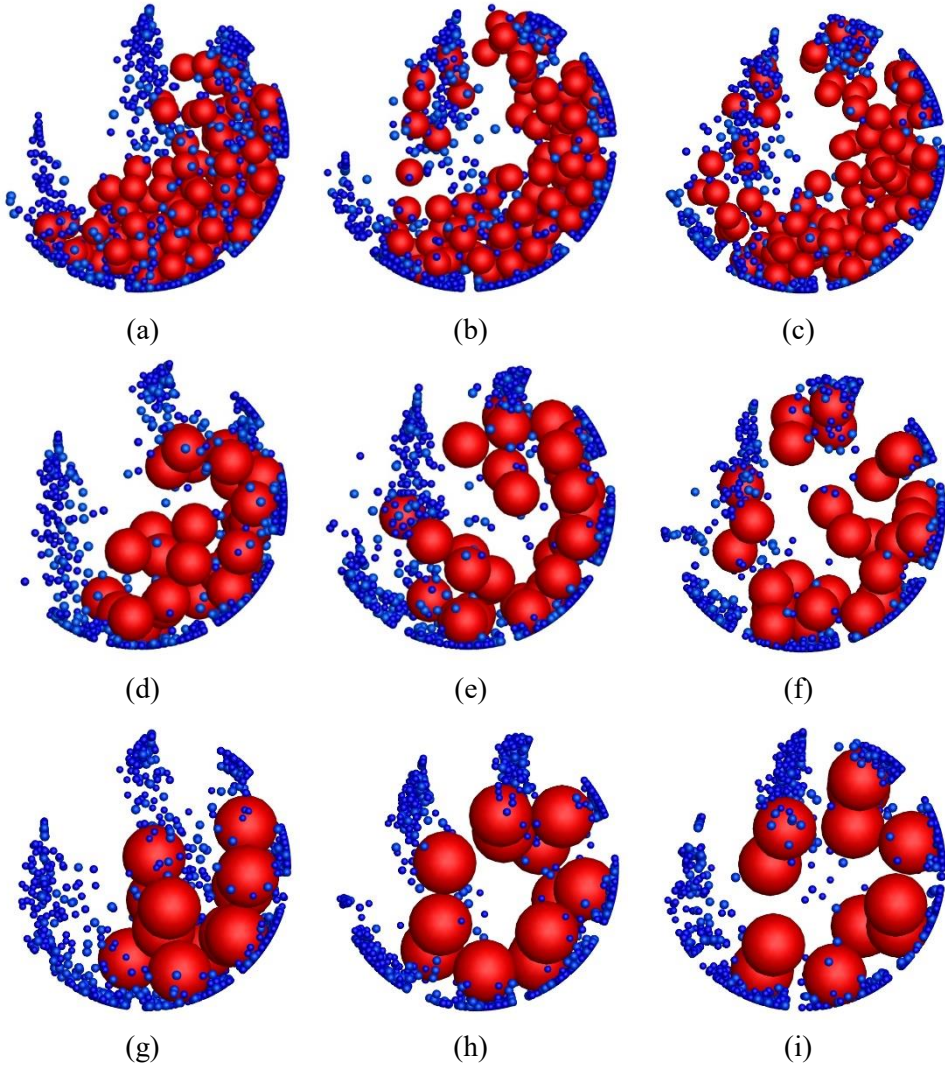
Figure 3.46. Comparison of the simulation snapshots when lifter size and ball

diameter (d) vary. (a) d = 19.05 and 8 mm lifter, (b) d = 19.05 and 12 mm lifter, (c)

d = 19.05 and 16 mm lifter, (d) d = 31.75 and 8 mm lifter, (e) d = 31.75 and 12 mm

lifter, (f) d = 31.75 and 16 mm lifter, (g) d = 44.45 and 8 mm lifter, (h) d = 44.45

and 12 mm lifter, and (i) d = 44.45 and 16 mm lifter.
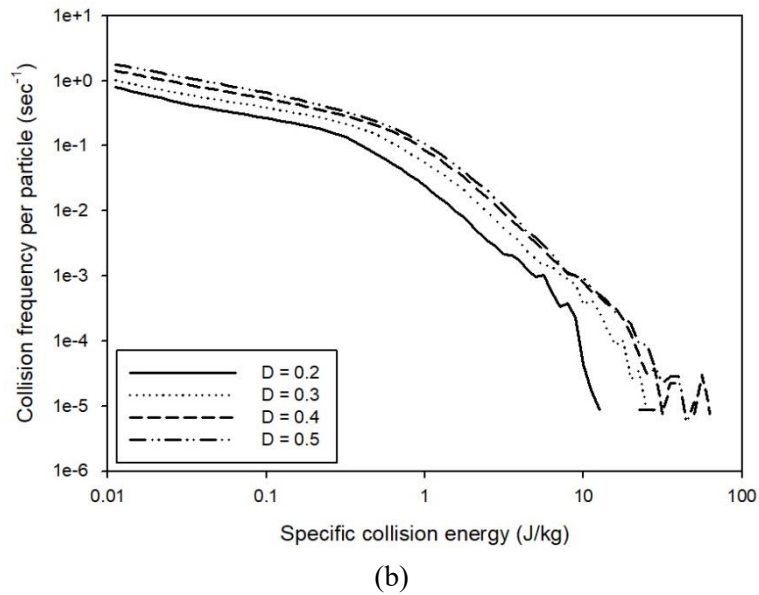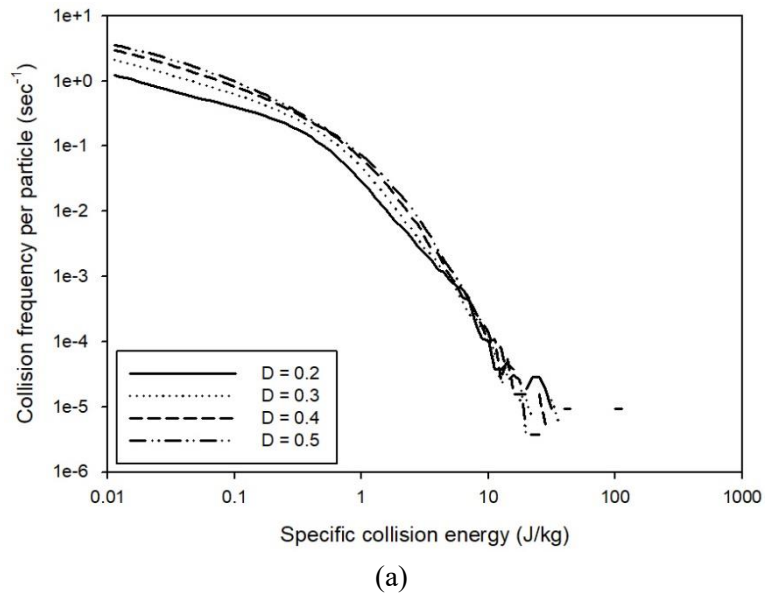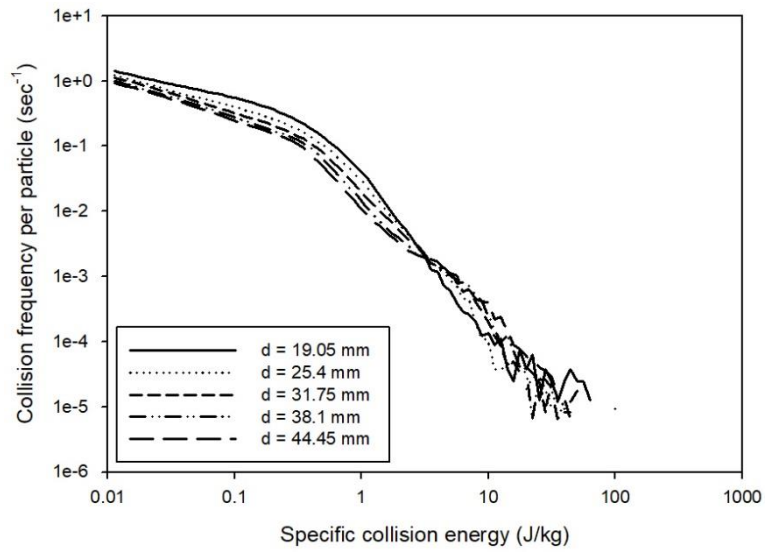
(a)
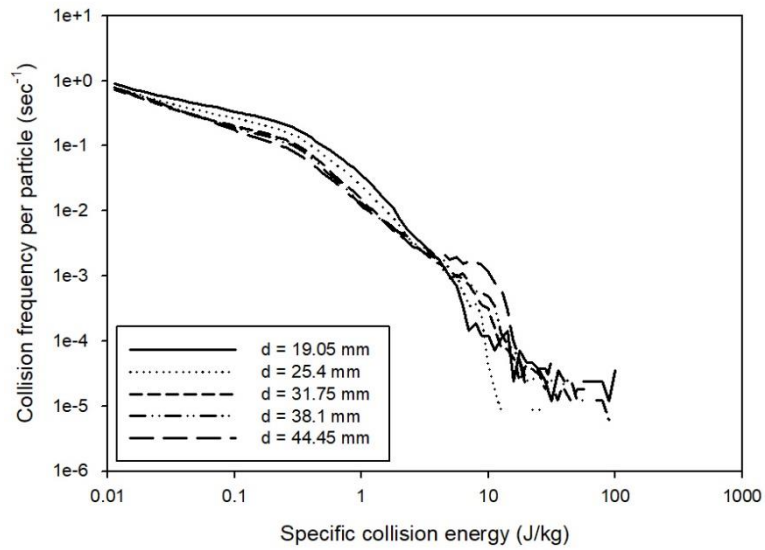
(b)

Figure 3.47. Changes in the energy distribution according to the ball diameter (d).

(a) 8 mm lifter and (b) 16 mm lifter.

As shown in Figure 3.47. the energy distribution shows that the smaller the ball diameter is, the higher is the collision frequency up to a certain energy level. As the ball diameter increased, the magnitude and frequency of the maximum collision energy become relatively high, however, because the absolute value remains small, it is not directly related to the breakage rate. As shown in Figure 3.31, the breakage rate changes according to the ball diameter. However, comparing the collision frequency at the minimum ball size, it is lower for the 12 mm lifter in Figure 3.31 than the 8 mm lifter in Figure 3.47. This can be attributed to the fact that the ball reaches the top of the mill when the lifter is large. The energy distribution according to ball diameter in Figures 3.31 and 3.47 show that it intersects in high energy regions, wherein, the larger the ball diameter is, the greater is the frequency of the high energy region. This indicates that the cataracting stream causes an effective collision for breakage even though the ball becomes larger considering large balls can be moved by larger lifters, as in Figure 3.46.

Changes in breakage rate, as shown in Figure 3.48, for small lifter is similar to that in Figure 3.33. When xE_0 is 2 Jmm/kg, it appears in a form that is almost consistent with the empirical formula, which indicates that the change in the number of collisions according to the change in the diameter and number of balls is inversely proportional to the particle breakage. For a large lifter, even when xE_0 is 2 Jmm/kg, the change in the breakage rate according to the ball diameter is different from the empirical formula. If the ball diameter is 31.75 mm or more, the breakage rate increases as a result of combining the effect of reduction in the number of collisions owing to the reduction in the number of balls and the effect that the cataracting stream favorably acts on the particle breakage by the large lifter. When xE_0 is larger

than 2 Jmm/kg, the larger the ball diameter is, the smaller is the decrease in the number of collisions greater than the threshold energy. Therefore, similar to Figure 3.33, Figure 3.48 shows a large difference in the breakage rate depending on the changes in the material properties.
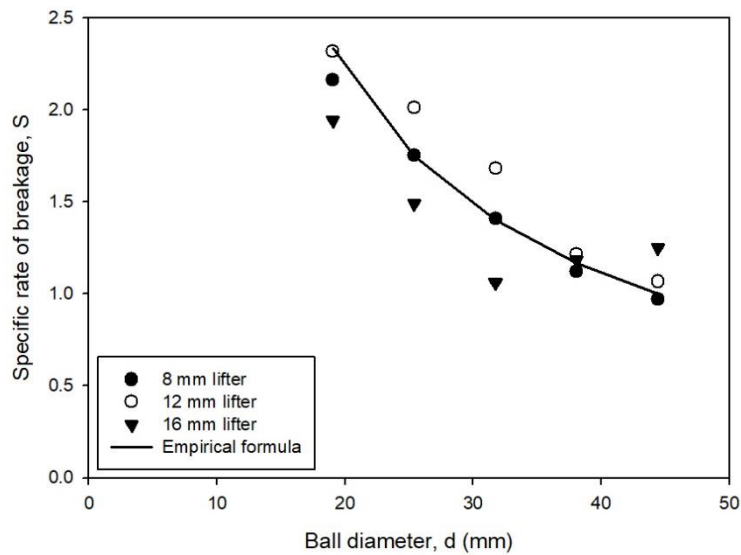
Figure 3.48. Changes in the specific rate of breakage according to ball diameter (d) for various lifter sizes.

3.4.6.3. Mill rotational speed

The changes in the breakage rate according to the mill rotational speed is the most sensitive operating condition to the lifter size. Figure 3.49 shows the simulation for different mill rotational speed and lifter size, with the critical rotation speed ratios of 0.6 and 0.8, where the difference according to the lifter size is most evident.

In both cases, a big difference was observed in the stream of the ball. When the fraction was 0.6, the ball bed formed a steeper slope as the lifter size increased, as shown in Figures 3.49(a) to (c). When the lifter size decreased, the cascading stream occurred predominantly; however, when the lifter size increased, the cataracting stream occurred actively. When the fraction increased to 0.8, the cataracting stream became active even when the lifter size was small, as in Figure 3.49(d). Conversely, when the lifter size was large, the ball gets attached to the wall and rotates (Figure 3.49(e), (f)), which indicates that the increasing mill rotational speed prevents the ball from falling effectively and causing breakage. This phenomenon occurred when the fraction was 0.9 for small lifter sizes. Figure 3.50 shows the change in energy distribution depending on the mill rotational speed caused by changes in the ball movement when the lifter size is changed.

(a)　　　　　　　　(b)　　　　　　　　(c)

(d)　　　　　　　　(e)　　　　　　　　(f)
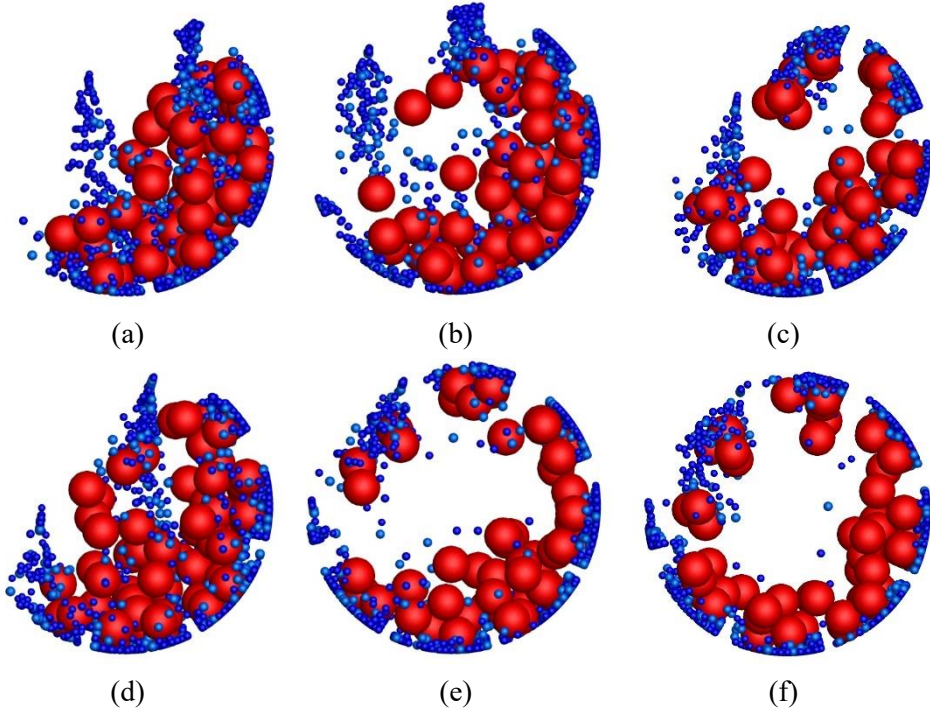
Figure 3.49. Comparison of the simulation snapshots when the lifter size and mill

rotational speed vary. (a) $0.6\varphi_c$ and 8 mm lifter, (b) $0.6\varphi_c$ and 12 mm lifter, (c)

$0.6\varphi_c$ and 16 mm lifter, (d) $0.8\varphi_c$ and 8 mm lifter, (e) $0.8\varphi_c$ and 12 mm lifter,

and (f) $0.8\varphi_c$ and 16 mm lifter.

(a)

(b)
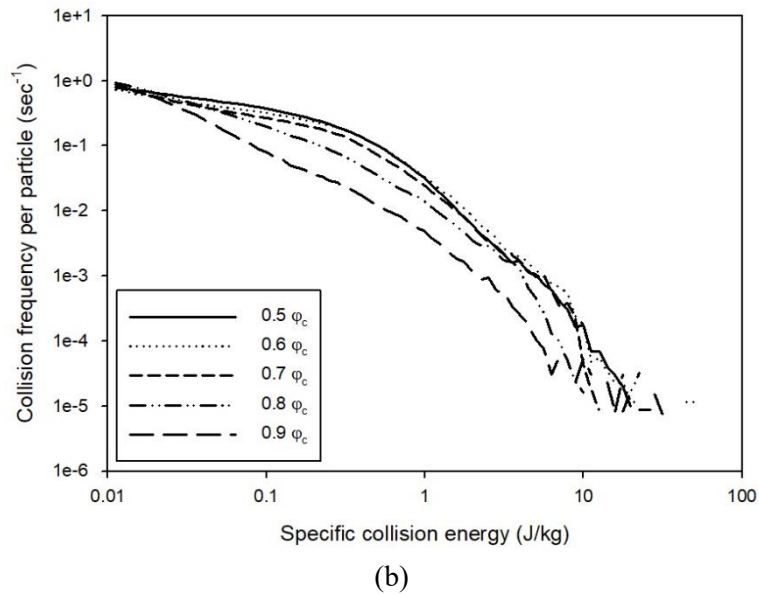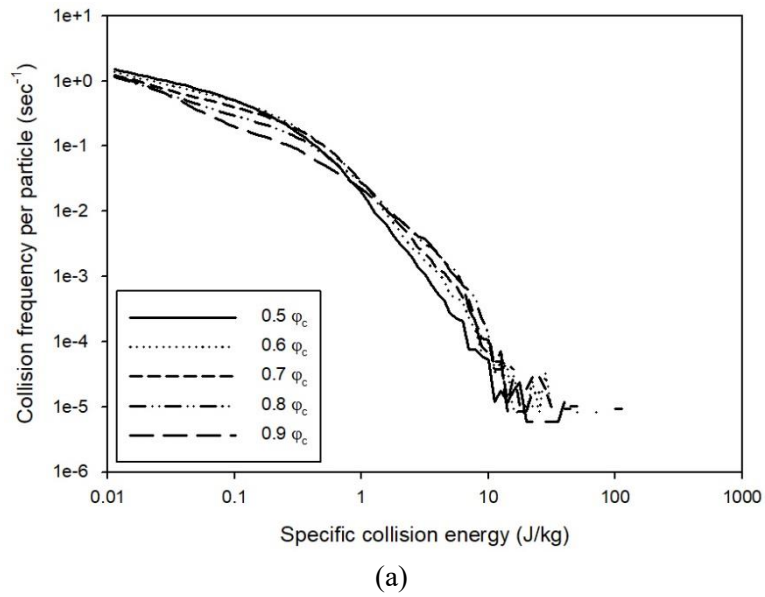
Figure 3.50. Changes in the energy distribution according to the mill rotational

speed. (a) 8 mm lifter and (b) 16 mm lifter.

For smaller lifters, the overall change in the energy distribution for the mill rotational speed is similar to the energy distribution for the original lifter size, as shown in Figure 3.35. However, a difference of 0.1 was observed in the mill rotational speed having a similar energy distribution, that is, the distribution of fractions 0.7 and 0.8 in Figures 3.50 and 3.35, respectively, are similar. Another difference is the maximum collision energy at each rotational speed. As shown in Figure 3.35, the maximum collision energy is greater at the mill rotational speed at which the breakage rate is greater, and the order of the mill rotational speed with a large breakage rate is 0.7, 0.6, and 0.5. Although the same phenomenon does not appear in Figure 3.50, the product of effective energy and collision frequency above the given threshold energy of 0.3 J/kg appears larger in the order of 0.8, 0.7, and 0.6 (0.352, 0.350, and 0.325 J/kg/sec, respectively). When larger lifter sizes, the energy distribution shows a different pattern. When the fraction of the mill rotational speed is 0.8 or more, the energy distribution is lower than that in for 0.5. This is because cataracting occurs actively even if the fraction of the mill rotational speed is small, as in Figure 3.49. Additionally, when the fraction of the mill rotational speed is 0.6, the effective collision occurs more frequently, and the energy distribution when the mill rotational speed changes appear almost parallel.

Changes in the breakage rate according to the mill rotational speed is shown in Figure 3.51 by using the breakage rate when the rotational speed is 0.7 of the critical speed as a reference value. Herein, the calculation results for various xE_0 are shown together, and the empirical formula and results of 3.4.5.3 are indicated as straight lines.
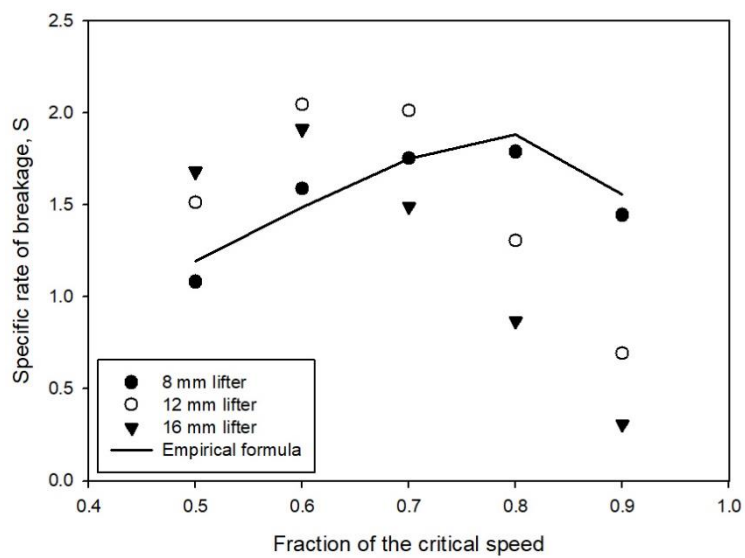
Figure 3.51. Change in the specific rate of breakage according to the mill rotational

speed for different lifter sizes.

Figure 3.51 shows that the relationship between the breakage rate and mill rotational speed, which agrees well with the empirical formula for the small lifter. This is due to the change of energy distribution according to the change in the lifter size. As the lifter size decreased, breakage occurred most effectively when the rotational speed fraction was 0.8, as in the empirical formula. As the balls eject from the lifter surface in the most efficient position, the effective collision energy occurs more frequently. Furthermore, the scale-up changes significantly depending on the properties of the material. For a large lifter, the breakage rate is relatively highest when the fraction of the mill rotational speed is 0.6 of the critical rotational speed. This is because the aforementioned ball movement and energy distribution are most favorable for particle breakage. Additionally, as shown in Figure. 3.50, because the energy distribution was almost parallel to the mill rotational speed, there was little difference in the breakage rate according to the material properties.

Chapter 4. Prediction of the Size-Grade Distribution of the Breakage Products by Coupling the Grinding and Liberation Model

Liberation is a one of the purposes of the grinding and an important factor in the subsequent separation process. A model that predicts the particle size and grade distribution is essential for designing an efficient grinding process. As equipment for measuring grade distribution has developed, it has become possible to easily measure various information. However, there are few cases where the measured data was effectively applied to the particle size-grade coupled model. In this chapter, the grinding and liberation parameters were determined by performing ball mill grinding experiments and MLA analysis of iron ore samples with various grades and sizes. Based on the grain size distribution, a method for determining the liberation size was developed. In addition, as one of the model applications, the target particle size of ball mill grinding process was set based on the degree of liberation.

4.1. Materials

The experiment was conducted using an iron ore from the Sinyemi mine, Jeongseon, Korea. Because the test ore was large to perform the ball mill grinding, the ore was crushed using a hammer mill (Large Holmes Hammermill Coal Crusher). The rotation speed of the shaft of the hammer mill was 1260 rpm, and screen plates in round-hole perforation had a diameter of 9.5 mm. Then, the breakage products of the

hammer mill were subjected to X-ray fluorescence (XRF) analysis to compare the element content based on particle size. The weight fraction of oxides of five elements Fe, Si, Al, Ca, and Mg was analyzed according to the particle size, as shown in Figure 4.1. Deviation in the weight fraction of each oxide with respect to the particle size was found to be insignificant, that is, the size reduction of the test ore occurred owing to the non-preferential breakage. Then, the breakage products were sieved to prepare single-size fraction (0.59–0.42 mm) sample, which was then subjected to magnetic separation to prepare samples of various iron grades for analyzing the difference of breakage characteristics according to the grade: concentrate, middling, and tailing. The grade of the samples were analyzed using inductively coupled plasma optical emission spectroscopy (ICP-OES). Table 4.1 summarizes the mass and iron grade of the samples.
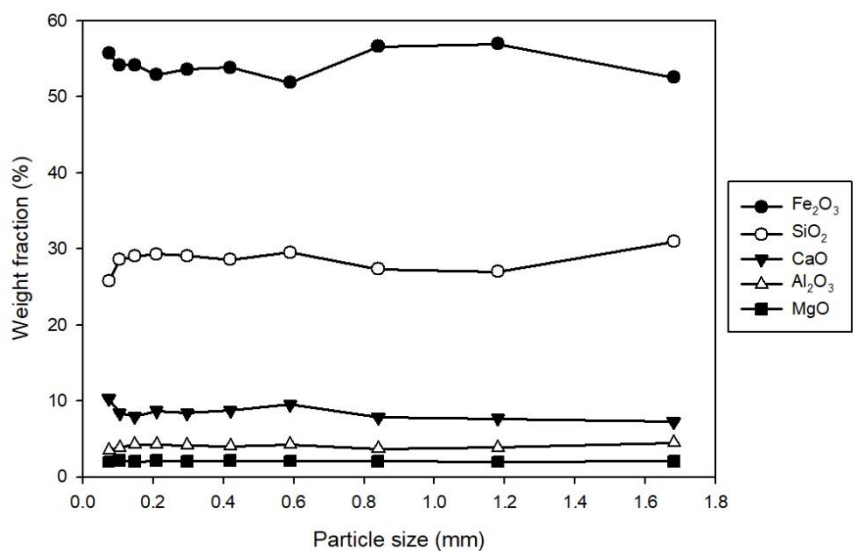
Figure 4.1. Weight fraction of the oxides according to the particle size.

Table 4.1. Mass and iron grade of the samples

| Item | Feed | Products of magnetic separator | | |
		Concentrate	Middling	Tailing
Mass (%)	100	42	47.3	10.7
Fe (%)	32	52	28	6

4.2. Methodology

Samples of various size-grade classes were treated separately to analyze the grinding and liberation characteristics. A ball mill was used to investigate the grinding kinetics of the samples based on the particle population balance modeling technique. Four grade classes of samples were ground using a stainless-steel mill charged with stainless steel balls and samples. Table 4.2 summarizes the mill design and operating variables. The specific gravities of the four grade classes of the samples (feed, concentrate, middling and tailing) were 2.20, 2.33, 2.06, and 1.80 respectively. Several grinding times (1, 2, 4, 8, and 16 min) were applied to each sample. After each grinding time, the mill was emptied and the discharge of the mill was sieved into nine fractions using a series of $\sqrt{2}$ spaced sieves from -0.59 +0.42 mm to -0.038 mm. A new sample was loaded for each test, considering over 5 g of each size classes was required for the following mineral liberation analysis. In other words, the total amount of the samples cannot be conserved. In case of tailing, only the grinding test was conducted considering there was not enough sample for the mineral liberation analysis.

Table 4.2. Mill design and operating conditions for the grinding test

Components	Detailed component	Value
Mill	Inner diameter, (mm)	200
	Length, (mm)	160
	Volume, (cm^3)	5024
	Rotation speed	75% of critical speed
Ball	Diameter, (mm)	25.4
	Specific gravity, (g/cm^3)	7.85
	Formal ball filling, J	0.2
Material	Formal powder filling, U	0.5
	Mass of injected feed, (kg)	0.440
	Mass of injected concentrate, (kg)	0.466
	Mass of injected middling, (kg)	0.412
	Mass of injected tailing, (kg)	0.360

Samples before and after grinding were analyzed to investigate mineral grade distribution by MLA. For the breakage products, all four size classes (- 0.59 + 0.42 mm, - 0.29 + 0.21 mm, - 0.15 + 0.10 mm, and - 0.073 + 0.052 mm) were used to analyze the mineral liberation. Each sample was characterized using the FEI Mineral Liberation Analyzer (FEI MLA) at KIGAM, which is an automated mineral analysis system based on SEM and provides mineral composition of particles in the polished section (Gu, 2003). The XBSE measurement mode was used and the quantitative data was obtained using the MLA Dataview software. By analyzing the sample before grinding, the minerals contained in the sample, magnetite, olivine, diopside, actinolite and phlogopite, were examined. Magnetite, an iron oxide, was selected as the target mineral. In addition, the size distribution of the magnetite grain of the three starting input sample were analyzed. The grade distributions of the magnetite were obtained for all samples before and after grinding. Based on the experimental data, the optimal parameters characterizing the liberation properties of samples were found and applied to the coupled grinding and liberation model to predict the breakage products. Figure 4.2 shows the flowchart of the whole process.
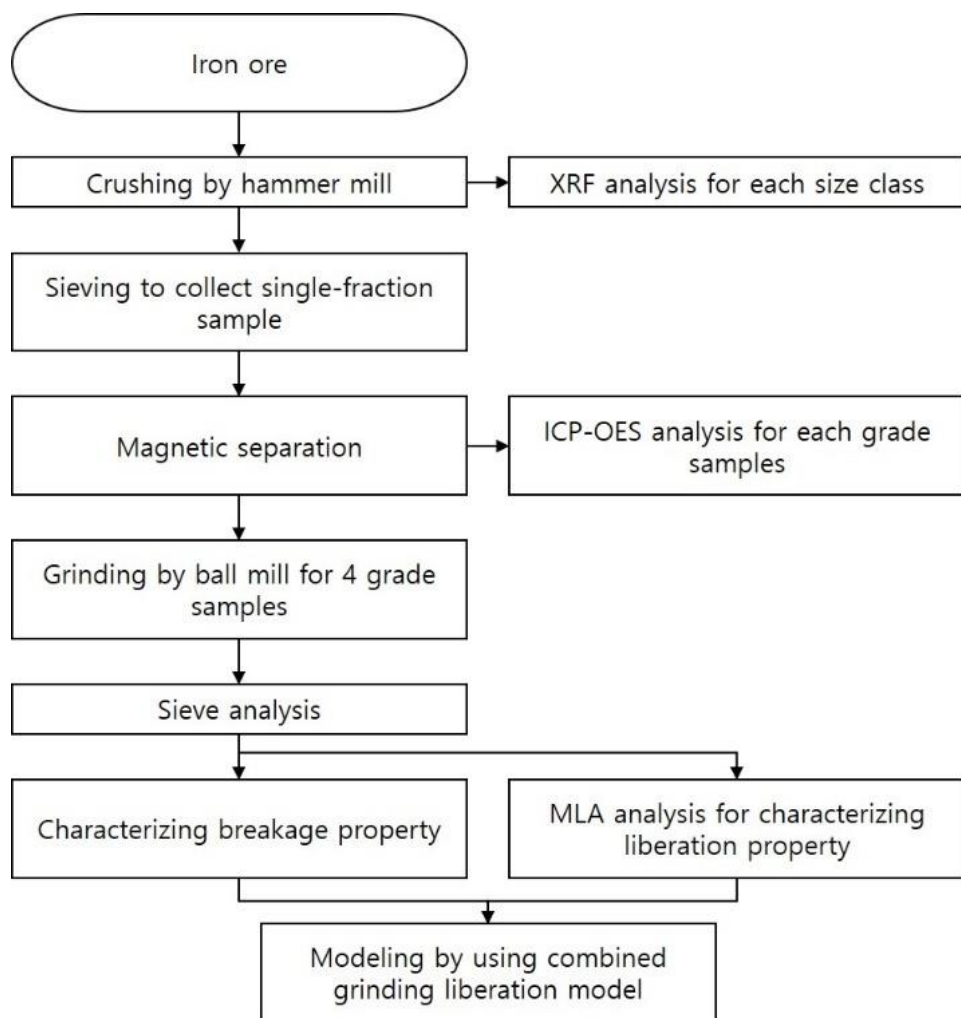
Figure 4.2. Flowchart of the overall process.

4.3. Results

4.3.1. Breakage Characteristics

The breakage rate of the single-size fraction sample was determined by plotting the ratio of the weight fraction that remained in the original size and the initial weight fraction over the grinding time. Figure 4.3(a) shows the results. As seen from the figure, the first-order kinetics of grinding were established for all except the tailing. The specific rate of breakage of the top size was obtained from the slope of the plot, and was found to be similar, as shown in the graph. For the tailing, the slope was calculated after 2 min of grinding time. Furthermore, the cumulative breakage distributions were estimated from the size distribution of short grinding time (1 min) using the BII method. The value of B_{ij} for all samples was plotted against the relative size, which can be fitted by the empirical function of breakage distribution, shown in Eq. (2.8). Figure 4.3(b) shows the cumulative breakage distribution of the ore, and Table 4.3 shows the estimated parameters for each sample.
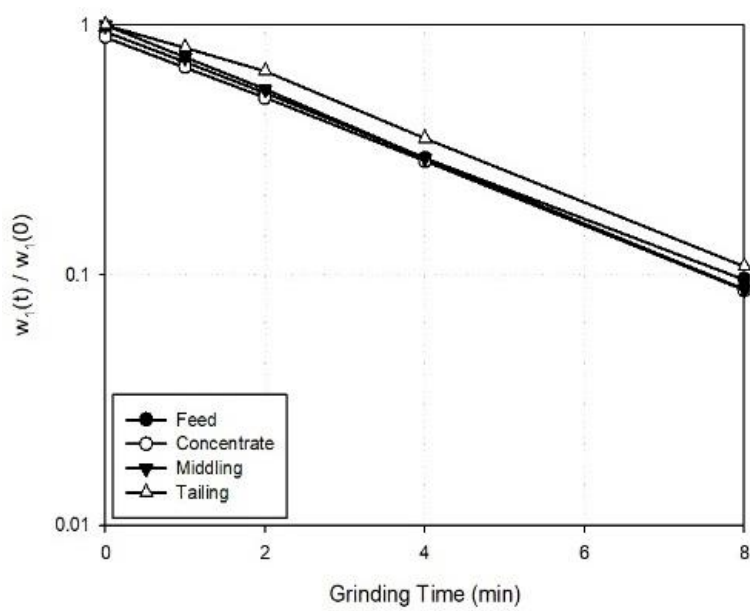
(a)
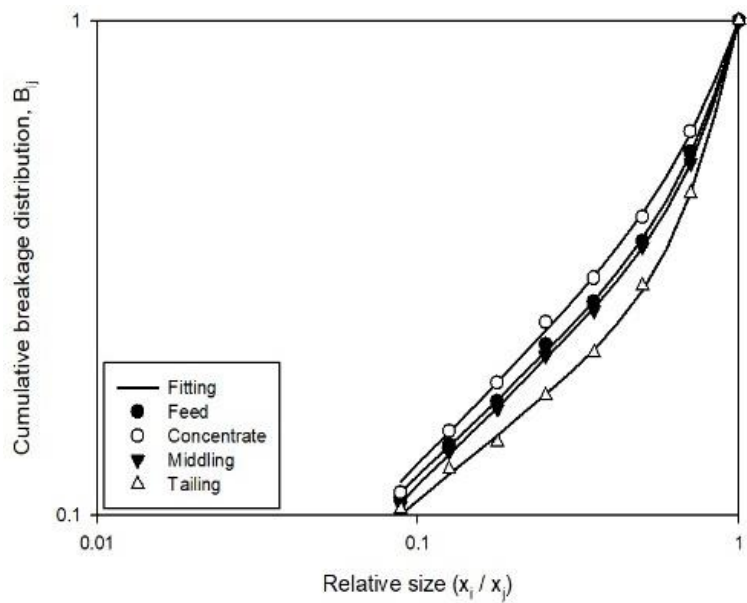
(b)

Figure 4.3. Breakage characteristics of iron ore. (a) First-order kinetics and (b)

Cumulative breakage distribution.

Table 4.3. Breakage distribution parameters

Breakage parameters	Feed	Concentrate	Middling	Tailing
Φ	0.4956	0.5757	0.4996	0.3591
γ	0.6152	0.6569	0.6378	0.5242
β	3.6968	3.3023	4.2308	4.1820

Back-calculation was performed to estimate the specific rate of breakage parameters. When an experiment is performed in a small particle size region, the breakage rate in Eq. (2.2) was simplified to Eq. (4.1). In other words, it excludes the reduction in the breakage rate occurring in the large particle size region.

$$S = A \left(\frac{x_i}{x_0} \right)^{\alpha} \tag{4.1}$$

By using Eqs. (2.8) and (4.1), breakage parameters A and α were determined and it is listed, as shown in Table 4.4. Tables 4.3 and 4.4 show that A is constant regardless of the grade; however, the other breakage function parameters exhibit different values depending on the grade of the samples. As shown in Figure 4.4, the estimated results using breakage function parameters in Tables 4.3 and 4.4 showed good agreement with experimental results.

Table 4.4. Breakage rate parameters

Breakage parameters	Feed	Concentrate	Middling	Tailing
A	0.295	0.295	0.295	0.295
α	0.8323	0.8844	0.8477	0.7014
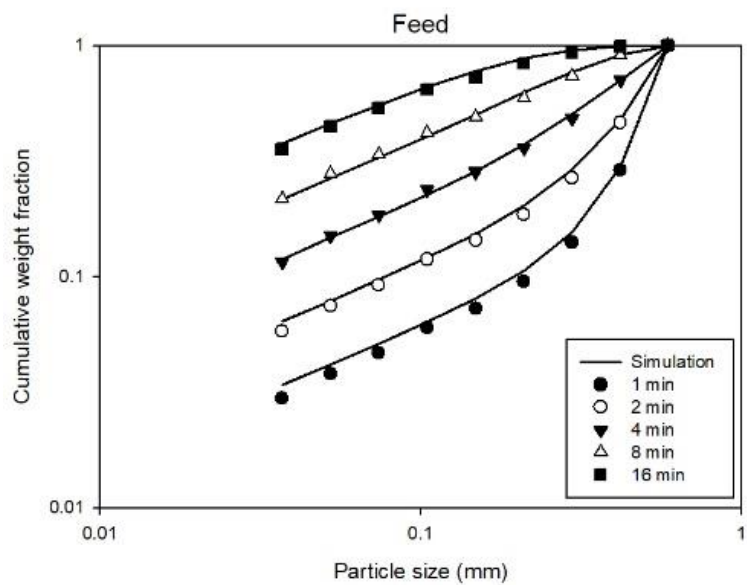
(a)
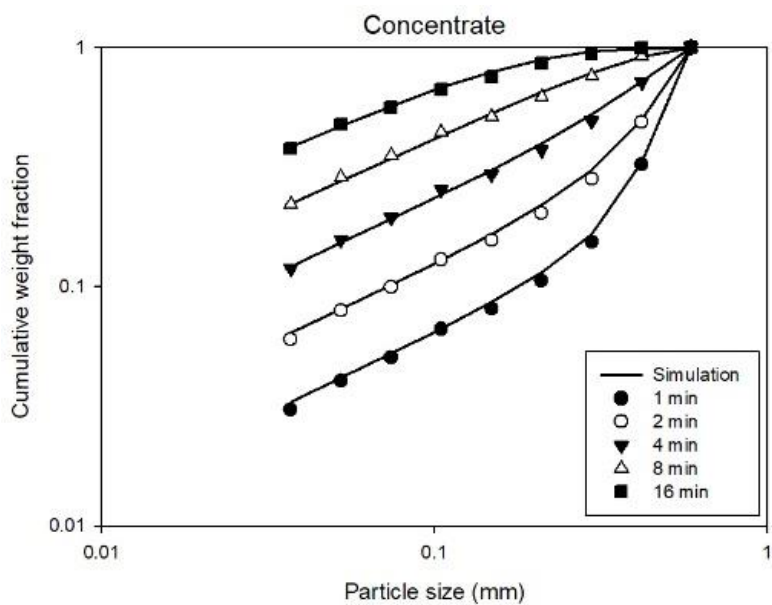
(b)
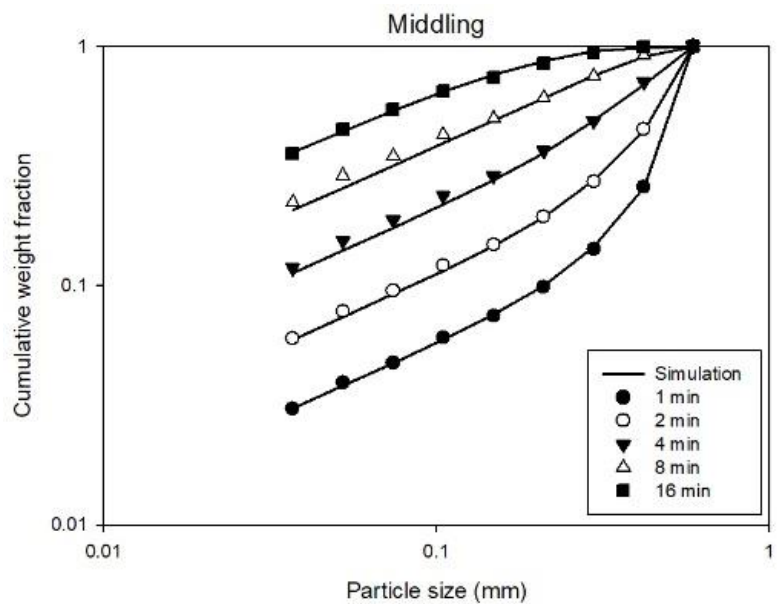
(c)
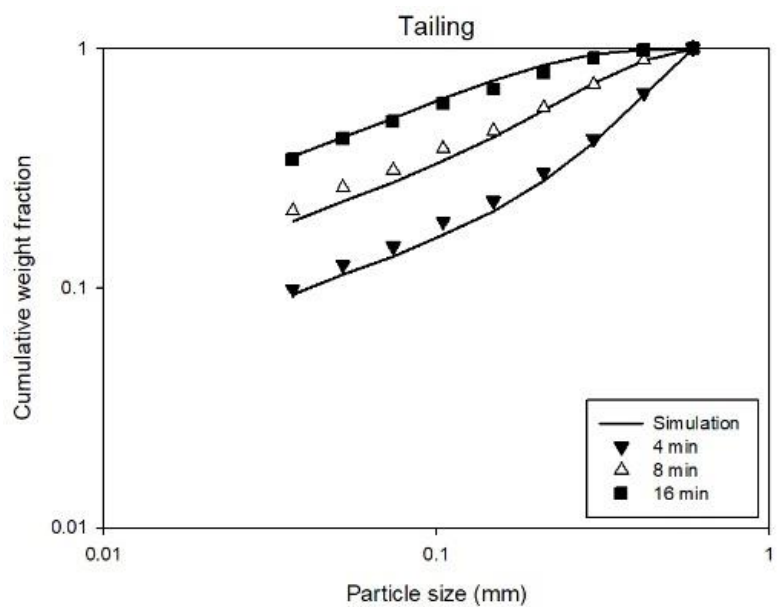
(d)

Figure 4.4. Measured and predicted size distributions. (a) Feed, (b) Concentrate, (c)

Middling, and (d) Tailing.

In the population balance equation Eq. (2.12), two breakage functions according to the particle size and grade are required. Breakage parameters, except for A, were assumed to vary linearly with the magnetite grade depending on the experimental results shown in Figure 4.5. The grade of magnetite is measured using MLA in the next section, and the grades of feed, concentrate, and middling were calculated as 0.44, 0.73, and 0.41, respectively. For the tailing, the grade was set to 0 considering MLA analysis was not performed, and the tailing was expected to have very low magnetite content. As shown in Table 4.1, the iron grade of the tailing is 6%. If all iron-bearing minerals are assumed to be magnetite, the grade of magnetite would be approximately 0.08. According to Eq. (4.1), Figure 4.5(a), and parameter A, which remains constant regardless of the grades shown in Table 4.4, calculate the breakage rate according to the particle size for each grade. For the same particle size, the higher the grade is, the larger is the breakage rate, and larger is the difference as the particle size decreases. This indicates that greater the content of magnetite compared to other minerals, greater is the resistance to breakage. The effect of grade on the breakage distribution parameters can be analyzed from Figures 4.5(b), 4.5(c), 4.5(d), and 4.3(b). As shown in Figure 4.5(b), the higher the grade is, the larger is the value of Φ. Generally, a larger Φ indicates that the particle breakage is caused by shatter, and fine particles are more likely to occur. In other words, the higher the grade, the finer is the breakage distribution. If Φ remains the same, the smaller γ becomes, and finer is the breakage distribution. As shown in Figure 4.5(c), the higher the grade, the larger is the value of γ, which indicates that the effect of γ is opposite to the effect of Φ according to the grade. However, γ has a relatively small difference in grade compared to Φ, and hence, the effect can be weaker. If the slope

of the breakage distribution is maintained up to a particle size region smaller than 37 μm, the tailing with a small γ could exhibit the highest weight fraction of the ultra-fine particles.

As shown in Figure 4.3(b), the higher the grade, the higher is the B_{ij} plot located in the graph, which indicates that there are more fine particles. β in Figure 4.5(d) reflects the distribution in the large particle section, and it can be seen that the smaller the grade, the larger is the value of β, which indicates that the smaller the grade, the more distributed the coarser particles are. If the trend is interpreted based on the breakage rate, the higher the grade is, the higher is the particle resistance to breakage for a particle size of 1 mm or less, and the finer is the particle size distribution (PSD) after grinding. When both the breakage rate and breakage distribution are considered, the PSD over time can be determined. If the grinding time is short, the breakage products of the high-grade sample exhibit a finer PSD. However, as the grinding time increases, the α of the breakage rate significantly influences PSD as the amount of fine particle increases. Accordingly, the PSD of the breakage product of the high-grade sample with a large α becomes coarser. In fact, if the PSD of the breakage product of each sample after 8 min is calculated, the lower the grade, the finer the PSD of the breakage product after grinding for over 32 min.

(a)

(b)

151
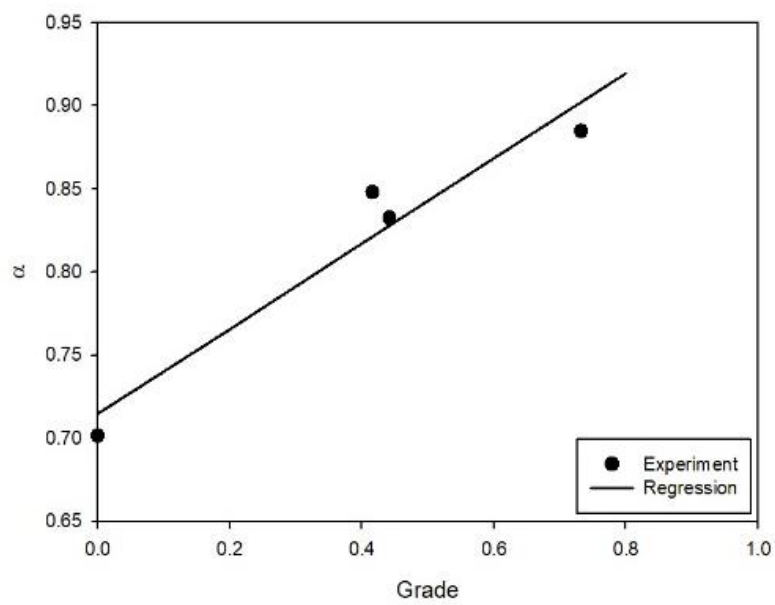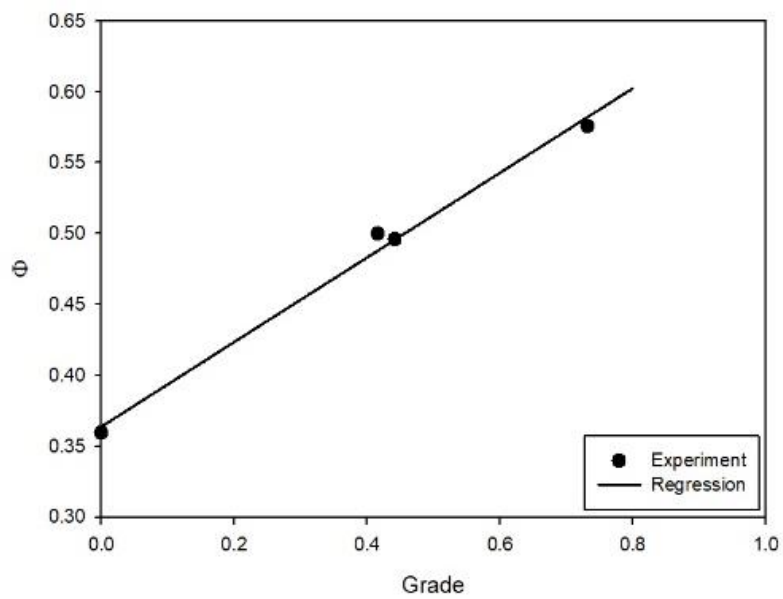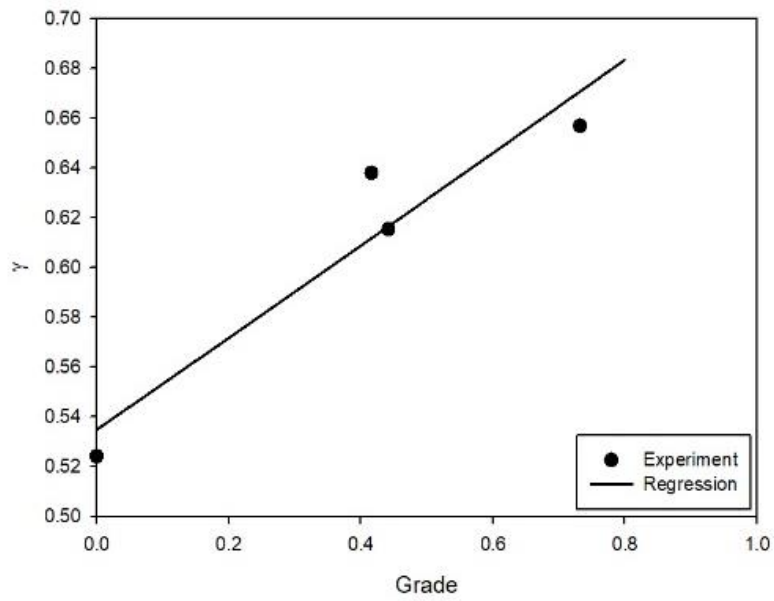
(c)
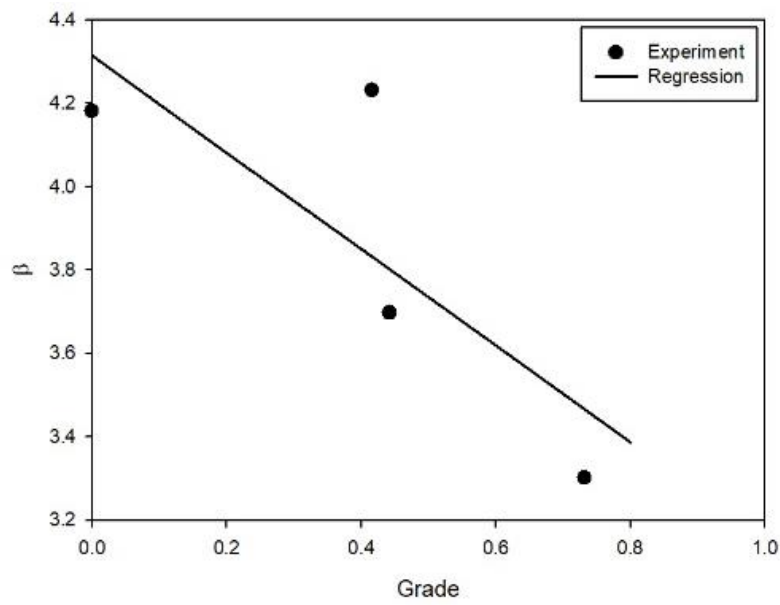
(d)

Figure 4.5. Breakage parameters according to the grade: (a) α, (b) Φ, (c) γ, and

(d) β.

4.3.2. Mineral Liberation Analysis

The grade distribution for each particle size class of various breakage products was analyzed using MLA to describe the liberation characteristics. Four size classes among the breakage products of various grade classes samples were analyzed, and the MLA results of the maximum and minimum size of the 4 min breakage product of middling are shown in Figure 4.6. The different colors in Figure 4.6 represent the different minerals. Magnetite, the target mineral in this study, is represented in purple. Approximately 5000–20 000 particles were analyzed to ensure representativeness of the analyzed particles. As shown in Figure 4.6(a), the grain size of magnetite is relatively small compared to the particle size, which confirms that the magnetite grains are mixed with other minerals in each particle. Conversely, as shown in Figure 4.6(b), a large number of particles were close to perfectly liberated particles considering the particle size was sufficiently small as the grain size.
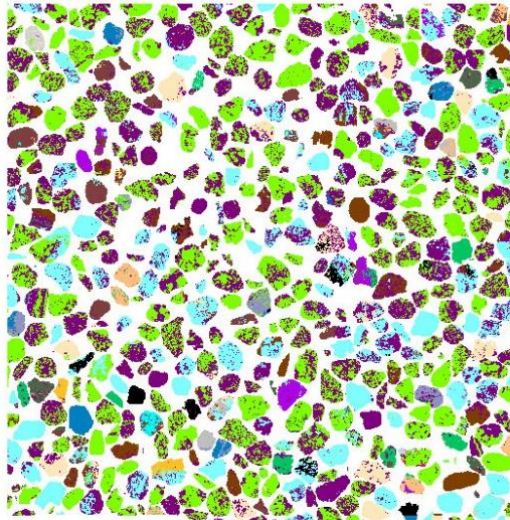
(a)
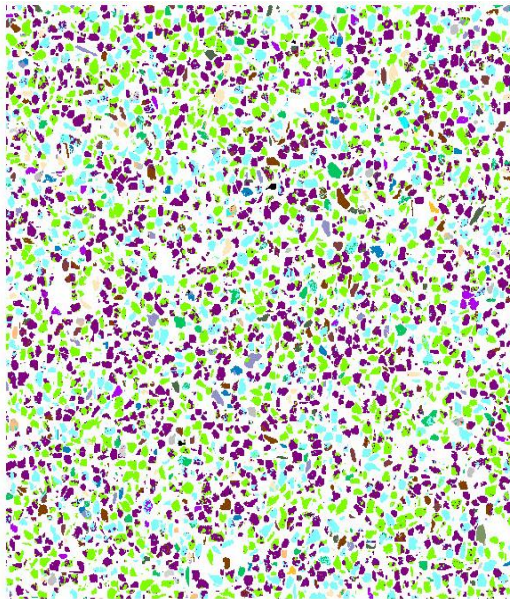
(b)

Figure 4.6. Examples of the MLA results for the middling samples. (a) – 0.59 +

0.42 mm and (b) – 0.073 + 0.052 mm.

The grade distribution obtained using MLA was separated into 12 classes, comprising 0, 1, and 10 classes equally spaced from 0 to 1. However, because the results were presented in 10 classes, grades 0 and 1 were added to grade classes 0 to 0.1 and 0.9 to 1, respectively. The analyzed results before grinding are shown in Figure 4.7. As shown in Figure 4.7(a), high-grade particles were concentrated in the concentrate. Furthermore, the feed sample comprised liberated particles. The average grade of magnetite in the feed sample was approximately 45%, but a difference was observed in the weight fraction of the liberated gangue and valuable minerals. Considering the ore is not an ideal binary mineral system, only magnetite should be excluded for the liberated gangue, which is relatively easier than producing a particle made entirely of magnetite. Additionally, during middling, the weight fraction of liberated gangue was found to be similar to that of the feed. It is inferred that a large amount of liberated gangue exists in tailings. As shown in Figure 4.7(b), the grain size exists over a wide range from 0.048 to 0.59 mm, which indicated that the grains contained in concentrate were coarser than the feed and middling.
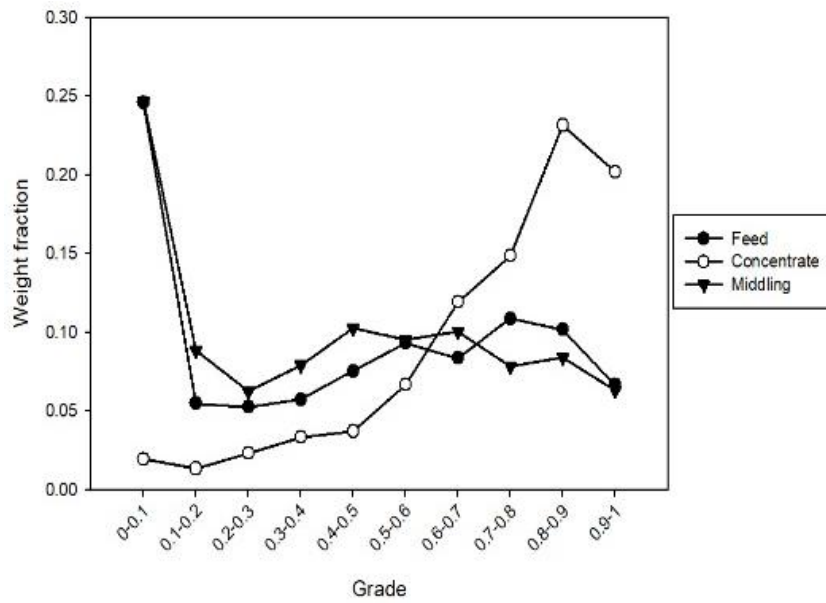
(a)
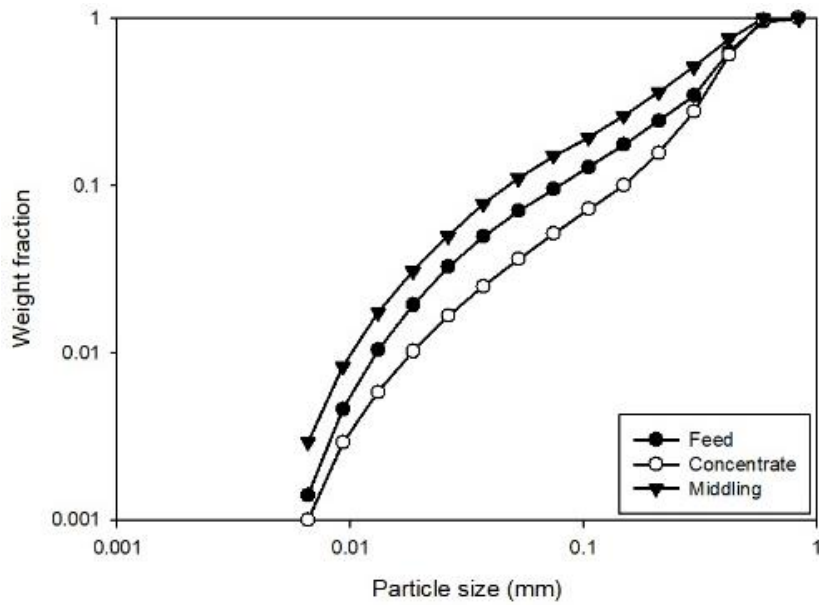
(b)

Figure 4.7. MLA results of the samples before grinding. (a) Grade distribution and

(b) Grain size distribution.

Figure 4.8 shows the grade distribution depending on the particle size for the 4 min breakage products of all samples using MLA analysis. As the particles become finer, the weight fraction of grades between 0.1 and 0.9 decreases, which increases the almost pure gangue and magnetite particles, taking a more distinct U-shape distribution.

(a)
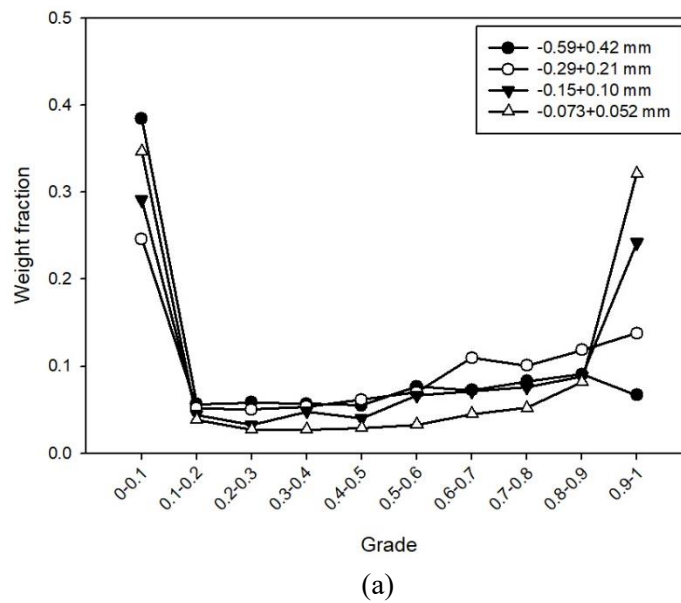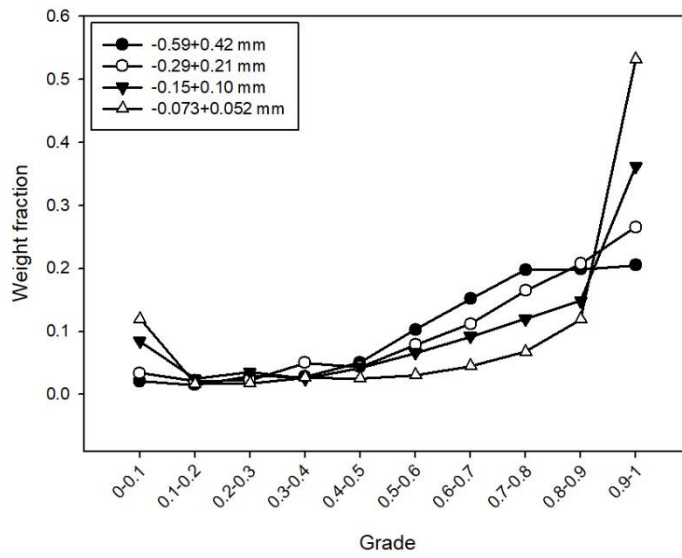
(b)
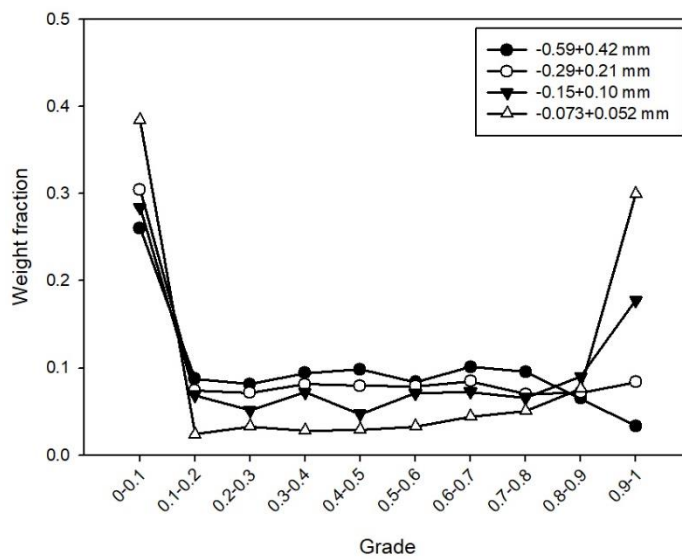
(c)

Figure 4.8. Grade distribution according to the particle size. (a) Feed, (b)

Concentrate, and (c) Middling.

Figure 4.9 shows the grade distribution of the three size fractions obtained after grinding the middling sample at various grinding times. For the same size fractions, the grade distributions were similar regardless of the grinding times, thereby indicating that for a given composition of a particles, the liberation characteristics does not change with time, and hence, can be described by the same set of liberation model parameters, η and δ_0. These aspects decrease the number of model parameters significantly, making modeling more practical.
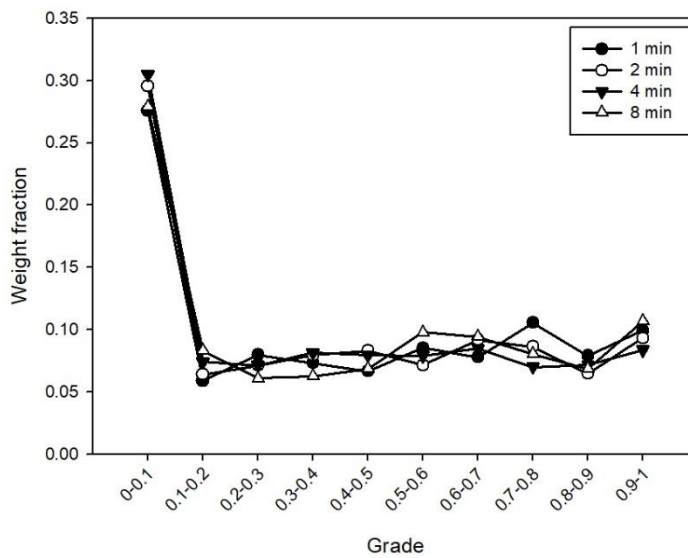
(a)
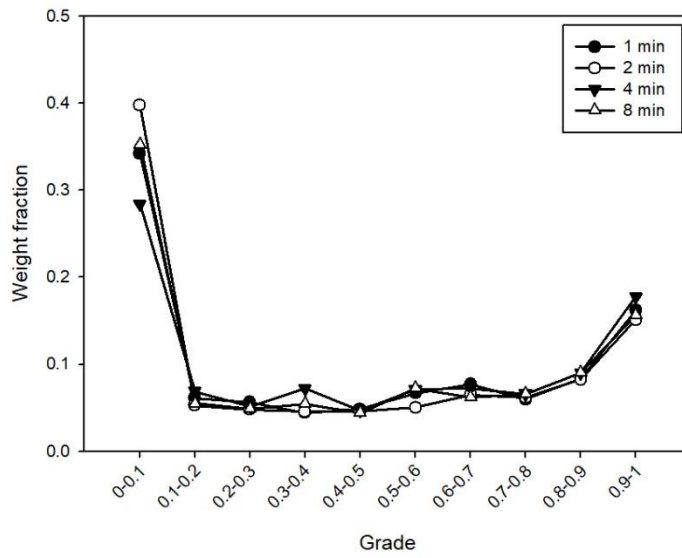
(b)
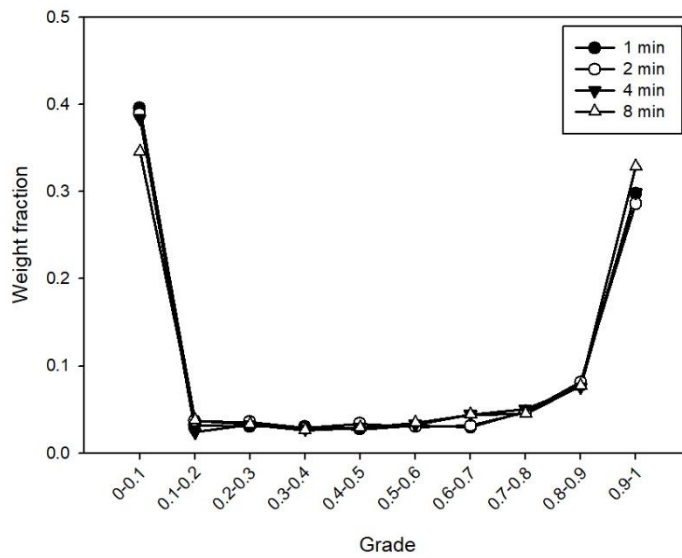
(c)

Figure 4.9. Grade distribution according to the grinding times. (a) – 0.29 + 0.21

mm, (b) – 0.15 + 0.10 mm, and (c) – 0.073 + 0.052 mm.

If the particle size and grade distribution is known, the degree of liberation can be determined. Considering only the measured data for four particle size classes was known, the overall grade distribution for a certain grinding time was calculated using the average of the total weight fraction of the measured classes, given as:

$$w_{i,all}(t) = \frac{\sum_j w_j(t) w_{ij}(t)}{\sum_j w_j(t)} \qquad (4.2)$$

where $w_{i,all}(t)$ is the weight fraction of grade class i considering all size classes at grinding time t. Then, the degree of liberation was calculated by using the ratio of the weight fraction of liberated particle to that of the total magnetite, while using particles with a grade of 90% or higher. As shown in Figure 4.10, the degree of liberation increases from 15% to 40% depending on the grinding time. However, there is a limit to determining the degree of liberation using the experimental value. As the grinding time increases, more fine particles occur, and based on the grain size distribution, the degree of liberation of particles smaller than -0.073+0.052 mm increases. Because it is practically impossible to develop a polished sample for the MLA analysis of smaller particles, the grade distribution of smaller particles cannot be reflected. Owing to this, the increase in the degree of liberation at 16 min is smaller than that at 8 min. Therefore, it is necessary to establish a model that can describe the overall size-grade distribution based on the MLA analysis.
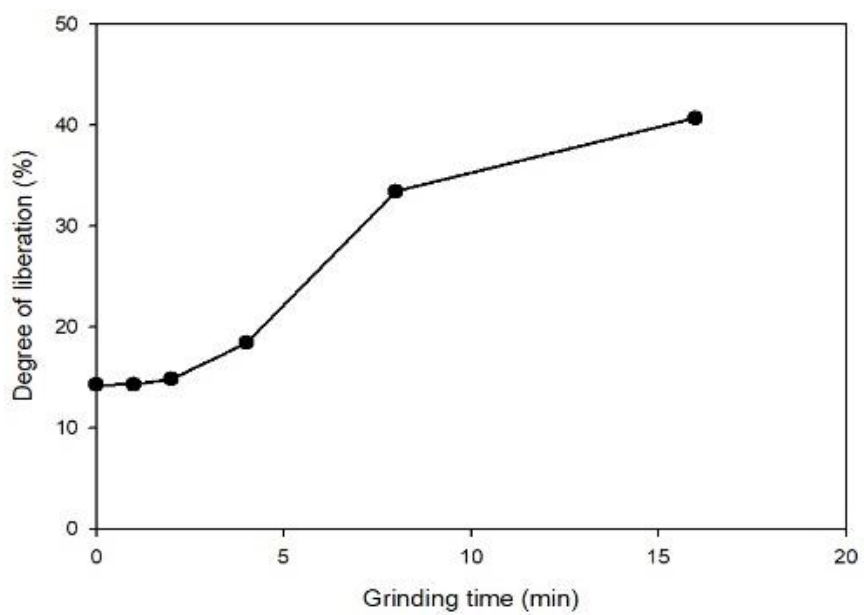
Figure 4.10. Degree of liberation over grinding time.

4.3.3. Simulation with the Coupled Grinding and Liberation Model

To predict the particle size-grade distribution, three liberation model parameters D_{lib}, δ_0, and η were required. The liberation size, D_{lib}, is the particle size at which the mineral starts liberating to be replaced by the grain size. However, the grain size distribution in Figure 4.7(b) shows the cumulative weight fraction of grains present in all particles according to their sizes. Considering grains present in individual particles have not been considered, Figure 4.7(b) cannot be considered to reflect the grain characteristics of the particles in each sample. Therefore, information on all grains constituting each particle can be obtained using MLA, and information on approximately 1000 or more particles and approximately 30 000 or more grains was measured for each sample before grinding. Based on the MLA data, the average grain size of magnetite contained in each particle was calculated, and the grain size distribution was reconstructed, as shown in Figure 4.11.
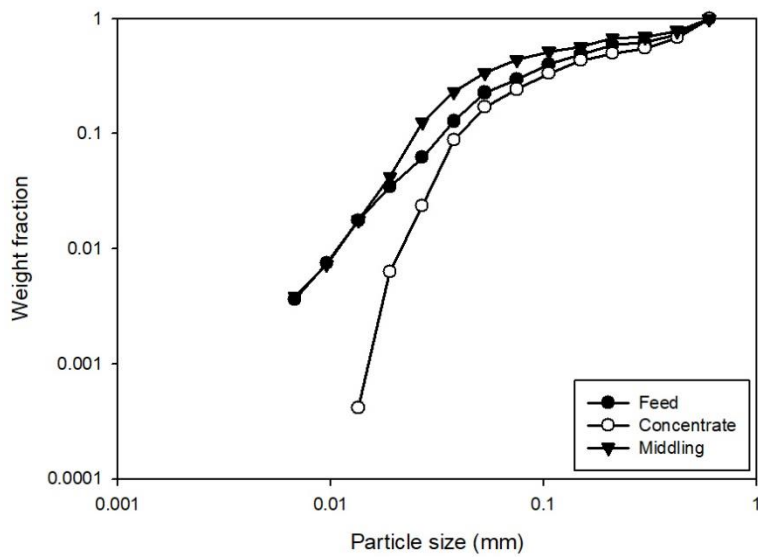
Figure 4.11. Grain size distribution based on the average grain size within each

particle.

Figure 4.11 shows that the concentrate comprises particles with large grain size, which are clearly distinguished from the other two samples. Additionally, although the feed and middling showed a similar distribution, the fine grain appeared relatively more in the middling. Considering the grain size is distributed over a wide range, the liberation size cannot be set as a single value. Furthermore, to reduce the computational load, the liberation size is grouped into five size fractions based on the grain size distribution. Then, the total size-grade distribution is estimated by weight averaging the results obtained for each liberation size. From d_{10} to d_{90}, it was separated into 5 sections at the same interval and same weight fraction of 20%.

Table 4.5. Liberation size of each sample

Samples (μm)	Feed	Concentrate	Middling
$D_{lib,1}$	533.85	545.03	515.50
$D_{lib,2}$	386.74	433.38	304.10
$D_{lib,3}$	156.42	214.20	98.53
$D_{lib,4}$	75.68	93.80	47.51
$D_{lib,5}$	33.77	40.48	25.06

The other liberation model parameters, δ_0 and η, were determined using back-calculation that was in good agreement with the experimental data. Figure 4.12 shows the model algorithms. Using the initially assumed values of δ_0 and η, first, the upper and lower grade bounds were determined, followed by calculating the beta distribution parameters that determine the distribution of grades within the grade range. After calculating the grade distribution within a progeny particle class, the breakage matrix, $b_{i,jkl}$ was generated by summing up the results for each feed size and grade fraction. Simulations are performed on various combinations of variables to determine the optimal parameters. As the feed for grinding had the grade distribution, the breakage rates of each grade class were calculated using the relationship shown in Figure 4.5 to generate the S_{ij} matrix. The breakage of a particle of a certain grade and size produces a whole suit of progeny particles, which was calculated using Eq. (2.8) with the values for Φ, γ, and β varying with the grades, as shown in Figure 4.5. Finally, a numerical scheme was used to calculate the product size-grade distribution for a grinding time t for a given feed size and grade.

Three grade samples
(Feed, Concentrate, Middling)

Grain size distribution from MLA analysis used for determining liberation size

Initial guess of liberation parameters
δ_0, λ

Calculating upper and lower grade boundaries

Determination of p and q for beta distribution

Iteration with updating liberation parameters for a given number of times

Calculating $b_{i,jkl}$

Is the iteration end?

No

Yes

Breakage function parameters
S_{ij}, $b_{j,kl}$

Determining of optimal liberation parameters

Estimation of breakage distribution
$b_{ij,kl} = b_{j,kl} * b_{i,jkl}$

Calculating breakage product using Explicit Euler method

$$\frac{dw_{ij}(t)}{dt} = -S_{ij}w_{ij}(t) + \sum_{l=1}^{j-1}\sum_{g_l}^{g_u} S_{kl}b_{ij,kl}w_{kl}(t)$$

Product size-grade distribution for given grinding time

Figure 4.12. Simulation model algorithm.

167

Parameters δ_0 and η that best fit the experimental data were found to be 1.3 and 1.6, respectively. The δ_0 value of 1.3 indicates that a stricter constraint is given by the ore texture compared to the constraint of preserving the total amount of minerals. Similarly, the η value of 1.6, which is a parameter indicating how quickly the degree of liberation changes as the particle size decreases, indicates that the change of the particle size affects the shape of the grade distribution. Therefore, when larger than the liberation size, the grade distribution is dense and does not spread easily owing to the decrease in particle size. When smaller than the liberation size, the grade distribution changes rapidly to a U-shape.

Figure 4.13 shows the simulated and experimental results, which confirms that the results are in good agreement.
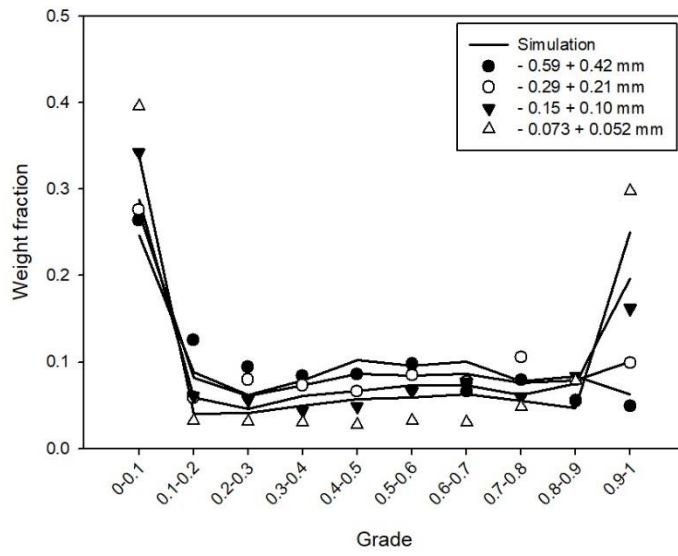
(a)
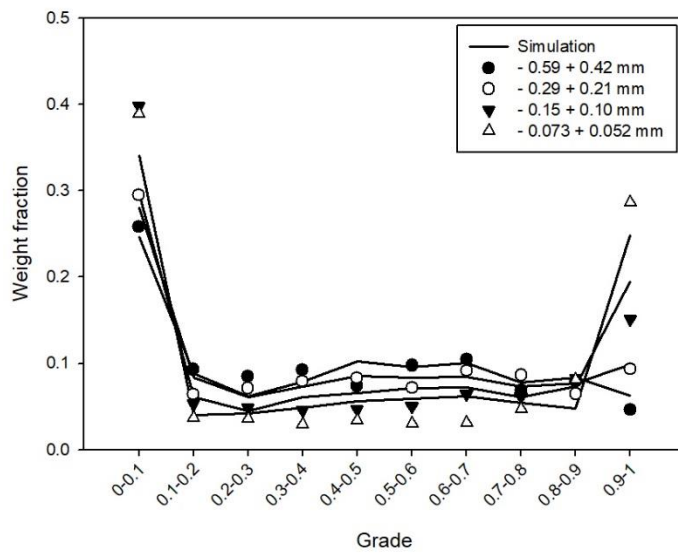
(b)
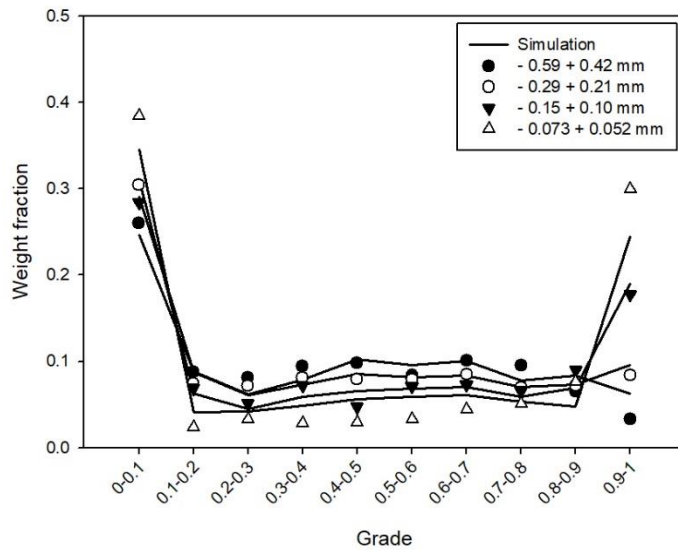
(c)
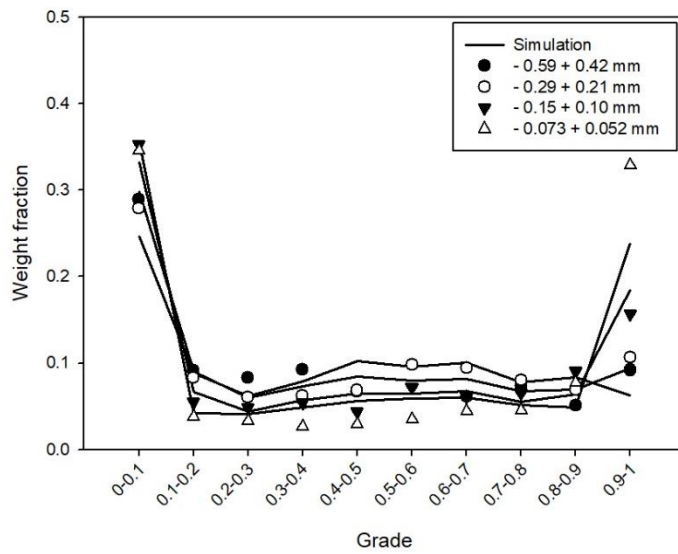
(d)

Figure 4.13. Simulation and experimental results of the middling sample: (a) 1 min,

(b) 2 min, (c) 4 min, and (d) 8 min.

To quantitatively compare the measured and predicted values, the degree of liberation of all measured samples was calculated through experiments and simulations, respectively. Figure 4.14 shows the comparison for all measured samples, and the coefficient of determination was 0.9004.
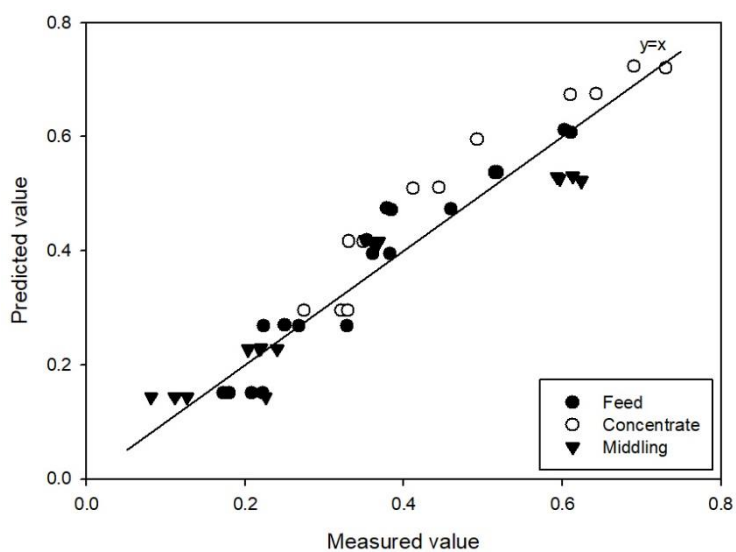
Figure 4.14. Comparison of the degree of liberation for the analyzed sample.

The coupled model can be used to set the target particle size to achieve the desired degree of liberation. Based on the grain size distribution, it is possible to determine the minimum particle size to be simulated. Furthermore, by performing simulations with a minimum particle size of about 0.0092 mm, the size of which the cumulative weight fraction of the grain is 0.01, the degree of liberation can be calculated more accurately. As an example, the 80% passing size when the degree of liberation for the concentrated sample was determined to be 0.8. First, the grinding time at a degree of liberation of 0.8 is calculated to be approximately 38 min, as shown in Figure 4.15(a). Considering it was analyzed for the concentrated sample, it was confirmed that the degree of liberation is higher than that of the middling sample. After the grinding time is determined, the particle size distribution at that time can be predicted. The particle size at which the weight fraction is 0.8 in the graph was found to be approximately 0.060 mm (Figure 4.15(b)).
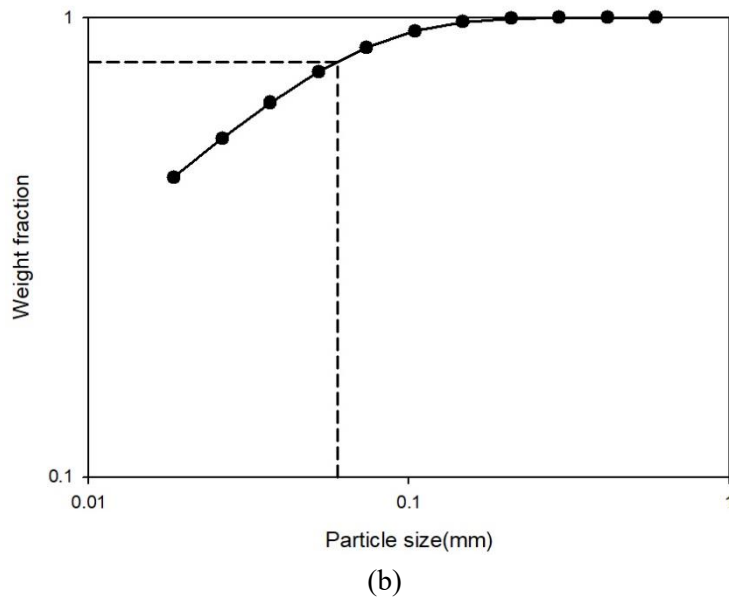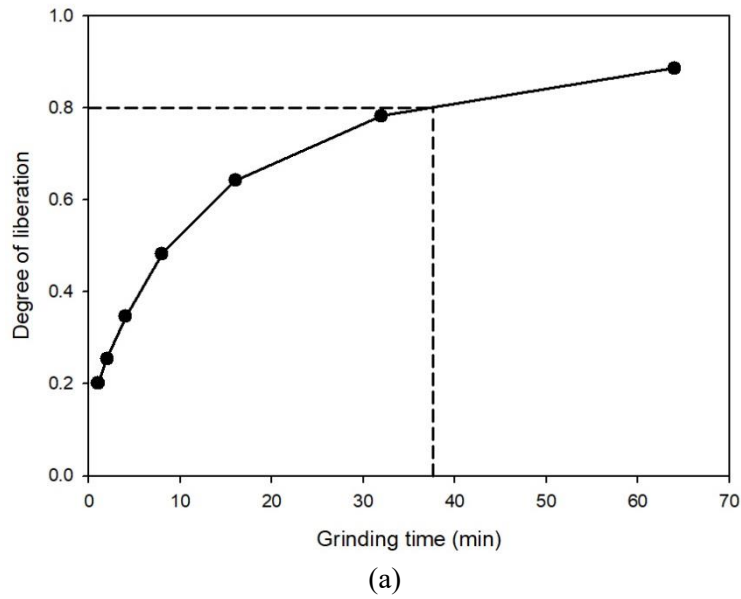
Figure 4.15. Application of the coupled model for setting the target particle size: (a)

Grinding time when the degree of liberation is 0.8 and (b) Particle size when the

weight fraction is 0.8.

Chapter 5. Conclusion

In this study, a more practical ball mill grinding model was developed using experimental and numerical approaches. For the experimental method, the breakage product was predicted by applying a model that combined particle size and grade, whereas for the method, ball mill modeling was performed by integrating DEM into the grinding kinetics framework.

First, the relationship between grade and breakage function parameters was investigated by performing single-fraction ball mill grinding tests for various grades. Furthermore, the MLA analysis was performed on various particle sizes and grades. As a result, the liberation size, one of the liberation parameters, was successfully derived based on the grade distribution and grain size distribution before grinding. Finally, other liberation parameters were determined using back-calculation, and the applicability of the coupled model was considered by deriving the target particle size to reach a specific degree of liberation.

Second, a ball mill simulation using DEM was performed by applying the particle breakage probability model. The results were analyzed based on the grinding kinetics model, which made it possible to independently determine the machine- and material-dependent factors, and calculate the breakage rate based on each factor.

By comparing the cases where the initial particle size distribution inside the mill was maintained and changed, it was confirmed that the first-order kinetics were established regardless of the particle size distribution inside the mill. Additionally, the particle weakening effect on repeated collisions was described using the damage

calculated from the energy applied to particles at every collision and the breakage probability parameters.

The breakage rate was calculated based on the collision energy data, indicating that the breakage rate can be derived once the equipment conditions and material properties are determined. The breakage rate for various material properties was calculated to derive a correlation between the breakage probability and breakage rate parameters. As a result, it was confirmed that the breakage rate parameter, A, and probability parameter, E_∞, are inversely proportional when the breakage rate is small enough or the average energy distribution of each particle is dense. Additionally, it was confirmed that α, which denotes the particle size sensitivity in the breakage rate, was proportional to χ, which indicates the particle size sensitivity in the breakage probability. In this case, E_∞ was independent of α. In particular, α and χ coincide only when the threshold energy is 0, which indicates that there is a close correlation between the breakage probability and the breakage rate parameters.

On analyzing the scale-up of the ball mill, it was found that the diameter of the ball media and the mill rotational speed exhibited different changes in the breakage rate depending on the material properties. However, in case of the changes in the ball loading, powder loading, and mill diameter, the changes of the breakage rate with respect to the material properties were insignificant. Furthermore, the analysis of the breakage rate change depending on the changes in the operating conditions with reference to the material property showed reasonable agreement with the empirical formula, except for the mill diameter and mill rotational speed. In the case of the mill diameter, the change in the breakage rate was amplified owing to the

increase in the collision energy as the lifter size increased. Similarly, in case of the mill rotational speed, the critical speed decreased owing to the increase in the lifter size. This effect was too large for the size of the original lifter, and hence, deviated significantly from the empirical formula.

Lastly, simulations were performed by changing the lifter size affecting the breakage rate and the operating conditions. It was observed that as the lifter size decreased, the breakage decreased in all cases. In addition, for the reference material characteristics, the changes in the breakage rate owing to changes in the operating conditions except the ball loading showed a tendency to be closer to the empirical equation. In particular, the graph of the breakage rate change according to the mill diameter and mill rotational speed was found to be close to the empirical formula.

This study presented a more practical method for ball mill grinding modeling by conducting experimental and numerical methods. In the case of numerical methods, it is expected that a deeper understanding of the breakage characteristics of the particles can be achieved by expanding this study to the breakage distribution function and particle size distribution after breakage.

References

1. Ai, J., Chen, J. F., Rotter, J. M., Ooi, J. Y., 2011. Assessment of rolling resistance models in discrete element simulations. Powder Technology, 206(3), 269–282.

2. Andrews, J. R. G., Mika, Ts., 1975. Comminution of a heterogeneous material: development of a model for liberation phenomena. Proceedings of the 11th International Mineral Processing Congress.

3. Austin, L. G., Klimpel, R. R., Luckie, P. T., 1984. Process engineering of size reduction: ball milling. Society of Mining Engineers of American Institute of Mining, New York.

4. Austin, L. G., Luckie, P. T., 1972. Methods for determination of breakage distribution parameters. Powder Technology, 5, 215–222.

5. Bian, X., Wang, G., Wang, H., Wang, S., Lv, W., 2017. Effect of lifters and mill speed on particle behaviour, torque, and power consumption of a tumbling ball mill: Experimental study and DEM simulation. Minerals Engineering, 105, 22–35.

6. Bonfils, B., Ballantyne, G. R., Powell, M. S., 2016. Developments in incremental rock breakage testing methodologies and modelling. International Journal of Mineral Processing, 152, 16–25.

7. Cho, K., 1987. Breakage mechanisms in size reduction. Ph.D. thesis, University of Utah.

8. Cleary, P. W., Morrison, R. D., Delaney, G. W., 2018. Incremental damage and particle size reduction in a pilot SAG mill: DEM breakage method extension and validation. Minerals Engineering, 128(August), 56–68.

9. Cleary, P. W., Morrison, R. D., 2016. Comminution mechanisms, particle shape evolution and collision energy partitioning in tumbling mills. Minerals Engineering, 86, 75–95.

10. Cleary, P. W., Morrison, R. D., 2011. Understanding fine ore breakage in a laboratory scale ball mill using DEM. Minerals Engineering, 24(3–4), 352–366.

11. Cundall, P. A., Strack, O. D. L., 1979. A discrete numerical model for granular assemblies. Geotechnique, 29(1), 47–65.

12. Datta, A., Mishra, B. K., Rajamani, R. K., 1999. Analysis of Power Draw in Ball Mills by the Discrete Element Method. Canadian Metallurgical Quarterly, 38(2), 133–140.

13. Datta, A., Rajamani, R. K., 2002. A direct approach of modeling batch grinding in ball mills using population balance principles and impact energy distribution. International Journal of Mineral Processing, 64(4), 181–200.

14. de Carvalho, R. M., Tavares, L. M., 2013. Predicting the effect of operating and design variables on breakage rates using the mechanistic ball mill model. Minerals Engineering, 43, 91–101.

15. Evans, C. L., Andrusiewicz, M. M., Wightman, E. M., Brennan, M. S., Morrison, R. D., Manlapig, E., 2013. Simulating concentrators from feed to final products using a multi-component methodology. SME Annual Meeting & Exhibit (SME 2013) and CMA 115th National Western Mining Conference, Denver, CO, United States, (490).

16. Ferrara, G., Preti, U., Meloy, T. P., 1989. Inclusion shape, mineral texture and liberation. International Journal of Mineral Processing, 27(3–4), 295–308.

17. Gardner, R. P., Austin, L. G., 1962. A chemical engineering treatment of batch grinding. Proceedings, 1st European Symp. Zerkeinern. Verlag Chemie, Weinheim, 217–247.

18. Gaudin, A. M., 1939. Principles of mineral dressing. McGraw–Hill, New York.

19. Gu, Y., 2003. Automated scanning electron microscope based mineral liberation analysis. Journal of Minerals and Materials Characterization and Engineering, 2(1), 33–41.

20. Han, T., Kalman, H., Levy, A., 2003. Theoretical and experimental study of multi-compression particle breakage. Advanced Powder Technology, 14(5), 605–620.

21. Hertz, H., 1882. Ueber die Berührung fester elastischer Körper. In Journal fur die Reine und Angewandte Mathematik, 1882(92), 156–171.

22. Hlungwani, O., Rikhotso, J., Dong, H., Moys, M. H., 2003. Further validation of DEM modeling of milling: Effects of liner profile and mill speed. Minerals Engineering, 16(10), 993–998.

23. Iwasaki, T., Yabuuchi, T., Nakagawa, H., Watano, S., 2010. Scale-up methodology for tumbling ball mill based on impact energy of grinding balls using discrete element analysis. Advanced Powder Technology, 21(6), 623–629.

24. Kelly, E. G., Spottiswood, D. J., 1990. The breakage function; what is it really? Minerals Engineering, 3(5), 405–414.

25. King, R. P., Schneider, C. L., 1998. Mineral liberation and the batch communition equation. Minerals Engineering, 11(12), 1143–1160.

26. King, R. P., 2001. Modeling and simulation of mineral processing systems. Elsevier.

27. Kwon, J., Jeong, J., Cho, H., 2016. Simulation and optimization of a two-stage ball mill grinding circuit of molybdenum ore. Advanced Powder Technology, 27(4), 1073–1085.

28. Mariano, R. A., 2016. Measurement and modelling of the liberation and distribution of minerals in comminuted ores. Ph.D. thesis, The University of Queensland

29. Marktscheffel, M., Schönert, K., 1986. Liberation of composite particles by single particle compression, shear and impact loading. Proceedings, 6th European Symposium on Comminution, Nuremberg.

30. Meier, M., John, E., Wieckhusen, D., Wirth, W., Peukert, W., 2009. Generally applicable breakage functions derived from single particle comminution data. Powder Technology, 194(1–2), 33–41.

31. Mishra, B. K., Rajamani, R. K., 1992. The discrete element method for the simulation of ball mills. Applied Mathematical Modelling, 16(11), 598–604.

32. Mishra, B. K., Rajamani, R. K., 1994. Simulation of charge motion in ball mills. Part 1: experimental verifications. International Journal of Mineral Processing, 40(3–4), 171–186.

33. Misra, A., Cheung, J., 1999. Particle motion and energy distribution in tumbling ball mills. Powder Technology, 105(1–3), 222–227.

34. Mori, H., Mio, H., Kano, J., Saito, F., 2004. Ball mill simulation in wet grinding using a tumbling mill and its correlation to grinding rate. Powder Technology, 143–144, 230–239.

35. Morrison, R. D., Shi, F., Whyte, R., 2007. Modelling of incremental rock breakage by impact - For use in DEM models. Minerals Engineering, 20(3), 303–309.

36. Napier-Munn, T., 2015. Is progress in energy-efficient comminution doomed? Minerals Engineering, 73, 1–6.

37. Narayanan, S. S., Whiten, W. J., 1983. Breakage Characteristics for Ores for Ball Mill Modeling Proc. Australia's Inst, Min. Metall, 3rd Edn. No, 286.

38. Narayanan, S. S., Whiten, W. J., 1985. Determination of comminution characteristics of ores from single particle breakage tests. Trans. Inst. Min. Metall.

39. Peterson, R. D., Herbst, J. A., 1985. Estimation of kinetic parameters of a grinding-liberation model. International Journal of Mineral Processing, 14(2), 111–126.

40. Powell, M. S., Govender, I., McBride, A. T., 2008. Applying DEM outputs to the unified comminution model. Minerals Engineering, 21(11), 744–750.

41. Rumpf, H., 1973. Physical aspects of comminution and new formulation of a law of comminution. Powder Technology, 7(3), 145–159.

42. Shi, F., 2016. A review of the applications of the JK size-dependent breakage model: Part 1: Ore and coal breakage characterisation. International Journal of Mineral Processing, 155, 118–129.

43. Shi, F., Kojovic, T., 2007. Validation of a model for impact breakage incorporating particle size effect. International Journal of Mineral Processing, 82(3), 156–163.

44. Shi, F., Xie, W., 2015. A specific energy-based size reduction model for batch grinding ball mill. Minerals Engineering, 70, 130–140.

45. Tavares, L. M., King, R. P., 1998. Single-particle fracture under impact loading. International Journal of Mineral Processing, 54(1), 1–28.

46. Tavares, L. M., King, R. P., 2002. Modeling of particle fracture by repeated impacts using continuum damage mechanics. Powder Technology, 123, 138–146.

47. Tavares, L. M., 2017. A review of advanced ball mill modelling. KONA Powder and Particle Journal, 34, 106–124

48. Tsuji, Y., Tanaka, T., Ishida, T., 1992. Lagrangian numerical simulation of plug flow of cohesionless particles in a horizontal pipe. Powder Technology, 71(3), 239–250.

49. Vogel, L., Peukert, W., 2003. Breakage behaviour of different materials - Construction of a mastercurve for the breakage probability. Powder Technology, 129(1–3), 101–110.

50. Vogel, L., Peukert, W., 2004. Determination of material properties relevant to grinding by practicable labscale milling tests. International Journal of Mineral Processing, 74(SUPPL.), 329–338.

51. Vogel, L., Peukert, W., 2002. Characterisation of grinding-relevant particle properties by inverting a population balance model. Particle and Particle Systems Characterization, 19(3), 149–157.

52. Vogel, L., Peukert, W., 2005. From single particle impact behaviour to modelling of impact mills. Chemical Engineering Science, 60(18), 5164–5176.

53. Wang, M. H., Yang, R. Y., Yu, A. B., 2012. DEM investigation of energy distribution and particle breakage in tumbling ball mills. Powder Technology, 223, 83–91.

54. Weibull, W., 1951. A Statistical Distribution Function of Wide Applicability. Journal of Applied Mechanics, 103, 293–297.

55. WEICHERT, R., 1992. Anwendung von Fehlstellenstatistik und Bruchmechanik zur Beschreibung von Zerkleinerungsvorgängen. ZKG International, 45(1), 1–8.

56. Wiegel, R. L., 1967. A random model for mineral liberation bysize reduction. Trans. SME/AIME, 238, 179–189.

57. Williams, J. G., 1984. Fracture mechanics of polymers / J. G. Williams. Ellis Horwood.

국문요지

분쇄는 일반적으로 자원처리 공정의 첫 단계로 에너지 집약적인 공정이다. 그러나 분쇄의 오랜 역사에도 불구하고, 분쇄 현상을 정확히 모사하는 것은 천연 광물 광석의 불균질성에 기반하는 분쇄 메커니즘의 복잡성 때문에 여전히 이루어지지 않고 있다. 본 연구에서는 실험적 및 수치적 접근법을 통해 효과적으로 분쇄공정을 모델링하는 방법을 도출하였다.

먼저, 수치해석적 방법 중 하나인 DEM (Discrete Element Method)을 이용하여 볼밀 분쇄공정을 모사하고 장비 의존적인 요소와 물질 의존적인 요소를 분리하여 시료의 분쇄 특성을 규명하였다. 분쇄 속도론 모델은 물질의 분쇄 특성을 파악하여 분쇄 산물의 입도 분포를 예측하는 데에 높은 성능을 보이지만 밀 내부에서 발생하는 분쇄 현상에 대한 이해는 부족하다. 반대로, DEM 을 이용하면 밀 내부의 각 입자에 대한 모든 충돌을 분석할 수 있으나 볼밀 분쇄공정을 모델링하기 위하여 PBE (Population Balance Equation)와 결합하는 경우에는 상대적으로 분쇄 산물의 입도 분포를 예측할 때의 정확성이 떨어진다. 본 연구에서는 DEM을 이용하여 각 입자의 충돌 에너지 분포를 결정하였고, 볼밀 시뮬레이션에서 볼과 광석 입자를 모두 구현함으로써 정확한 에너지 데이터를 획득하였다. 뿐만 아니라 입자의 파괴 확률 모델을

도입함으로써 물질 의존적인 요소를 독립적으로 적용하였다. 최종적으로, 분쇄 속도론 모델에 기반하여 시뮬레이션 결과를 해석함으로써 분쇄 특성을 보다 정확하게 예측해보고자 하였다. 단일 입도 분쇄 시험 시뮬레이션에서는 시간 경과에 따라 밀 내부의 입도 분포를 변화시킴으로써 1 차 분쇄 속도론이 성립함을 확인하였고, 각 입자의 충돌 에너지 분포를 바탕으로 반복 충돌에 의하여 입자 파괴가 점차적으로 쉽게 발생하는 현상을 모사할 수 있었다. 또한, 파괴 확률 변수와 분쇄율 변수 사이의 연관성을 조사하였으며, 밀의 scale-up 과 리프터의 크기 변화에 따른 분쇄율의 변화를 분석하였다.

둘째로, 실험을 통해 분쇄 속도론에 기반하여 분쇄 산물의 입도 및 품위 분포를 예측하는 모델을 개발하였다. 단체분리 측정 장비의 발전과 함께, 분쇄 전 후의 시료에 대한 다양한 정보를 쉽게 얻을 수 있게 되었으나 이를 효과적으로 모델링에 활용하는 방법에 대한 연구는 부족한 실정이다. 다양한 입도 및 품위의 자철석 시료에 대하여 볼밀 분쇄 시험과 광물단체분리측정기를(MLA) 이용한 분석을 수행함으로써 분쇄 산물의 입도 및 품위 분포를 얻었다. 이를 통해, 품위에 따른 분쇄 특성과 단체분리 특성을 규명하였다. 특히, 단체분리 변수 중 하나인 단체분리 크기를 MLA 로 측정 가능한 광물입자 크기 분포를 사용함으로써 효과적으로 결정할 수 있었다. 또한, 분쇄-단체분리 결합 모델을 이용하여, 단체분리도를 고려한 목적 입도와 분쇄 소요 시간을 예측할 수 있었다.

이처럼, 본 연구는 수치적 및 실험적 방법을 통하여 더 실용적으로 볼밀 분쇄공정을 시뮬레이션하는 방법을 제안하였다. 특히, 수치적 방법의 경우에는 해당 연구 내용을 분쇄 후의 입도 분포를 분석하는 데에 적용함으로써 입자의 분쇄 특성에 대한 더 심도 있는 이해가 가능할 것으로 기대된다.

감사의 글

6 년의 석박사통합과정 동안 저에게 많은 도움을 주셨던 분들에게 학위논문의 말미를 빌려 감사의 말씀을 전하고자 합니다.

먼저 지도교수님이신 조희찬 교수님께 감사드립니다. 교수님의 지도와 가르침 덕분에 학위과정을 무사히 마치게 되었습니다. 교수님의 가르침을 가슴에 새기고 사회에 나가서도 자랑스러운 제자가 될 수 있도록 노력하겠습니다.

권지회 박사님, 처음 시뮬레이션을 이용한 연구를 알게 해 주셨고 다양한 방면에서 연구를 수행하는 데 큰 도움을 주셔서 감사드립니다. 연구 수행뿐만 아니라 논문 작성에 이르기까지 다양한 측면에서 여러 조언을 주셔서 감사합니다.

바쁜 일정 중에서도 저의 논문을 심사해주신 민동주 교수님, 정은혜 교수님, 김정윤 박사님께도 감사드립니다. 교수님과 박사님의 지도와 격려로 학위논문을 더욱 다듬을 수 있었고 논문의 질을 향상시킬 수 있었습니다.

한국지질자원연구원의 류동우 박사님과 Geo-ICT 융합연구팀원들께도 감사의 인사를 전합니다. Geo-ICT 융합연구팀의 배려로 2 년 동안 연구를 바라보는 관점을 확장하고 면밀히 연구를 수행할 수 있었습니다.

김관호 박사님, 한국지질자원연구원에서의 실험을 수행하는 데 있어 많은 도움을 주셔서 감사드립니다. 박사님의 도움으로 풍성한 연구 결과를 얻을 수 있었습니다.

그리고 학위과정 동안 많은 시간을 함께 보낸 연구실의 선후배 여러분들에게도 감사드립니다. 처음 연구실에 들어왔을 때 대학원 생활에 대해 많은 도움과 조언을 주셨던 선배님들과 이후 같이 연구실의 마지막까지 즐거움과 어려움을 함께 나누고 지낼 후배님들께 감사드립니다. 덕분에 연구실에서의 생활을 즐겁게 추억할 수 있을 것 같습니다.

비록 감사의 글에 모든 분들을 언급하지 못하였지만, 많은 분들에게 학위논문 과정에서 많은 도움과 격려를 받았습니다. 이를 잊지 않고 저 역시 다른 사람들에게 베풀 수 있는 사람이 되고자 노력하겠습니다. 감사드립니다.

마지막으로 오랜 시간동안 누구보다도 저를 응원해주시고 지지해주신 가족들에게도 감사드립니다. 우리 가족들 진심으로 항상 사랑합니다.